The University of Tokyo
Graduate School of Science
Department of Physics

Study of Neutron-Tagging Algorithm for SK-Gd

(SK-Gdに於ける中性子検出アルゴリズムの研究)

Seungho Han

Supervisor: Prof. Kimihiro Okumura

Submitted in part fulfillment of the requirements for the degree of
Master of Science in Physics of the University of Tokyo, January 2021

Abstract

Since July 2020, the SK-Gd phase of the Super-Kamiokande (SK) experiment has started by dissolving 0.0110 wt.% of Gadolinium (Gd) in the pure-water detector volume. The large cross section (48,700 barns) and de-excitation energy ($\sim$8 MeV) of the Gd(n,γ) reaction are believed to greatly enhance the neutron detection efficiency. If the Gd concentration reaches the target value of 0.1 wt.%, the efficiency is expected to improve up to $\sim$90 %, while the same efficiency for the pure-water detector volume has been only $\sim$25 %. With the enhanced detection efficiency of neutrino-induced neutrons, we hope to boost sensitivity in the search for Supernova Relic Neutrinos (SRN), neutrino oscillation parameters, and proton decays.

To evaluate the neutron detection efficiency with the current Gd concentration of 0.0110 wt.%, we have inherited and tested the so-called "neutron-tagging" algorithm that has been used within SK to detect $p(n,\gamma)$ signals in pure-water data. The algorithm searches for a cluster of hits on photomultiplier tubes (PMTs) that are localized in time, and applies a pre-trained Multilayered Perceptron (MLP) to classify the found clusters into signal and noise. The author has parameterized the factors that affect the algorithm's detection efficiency, and built a software that is able to transparently tune each parameter and create/train a custom MLP. Using the software and the SK-Gd simulator under development, the parameters were optimized to improve detection efficiency on both simulated $p(n,\gamma)$ and Gd(n,γ) events. In a realistic search setting, the neutron capture detection efficiency of the optimized algorithm to simulated neutron events was $\sim$92 % for Gd(n,γ), $\sim$26 % for $p(n,\gamma)$, and $\sim$61 % overall.

The tuned algorithm was applied to AmBe neutron source data taken after 0.0110 wt.% of Gd was fully loaded. For comparison, the same algorithm was applied to a simplified neutron source simulation without source geometry and detector triggers. (The full simulation is under development.) The simplified simulation has proved to be effective in reproducing the feature distributions of the neutron source data, although the simulation physics model appears to have a larger Gd(n,γ)-to-$p(n,\gamma)$ ratio. As a consequence, the algorithm shows a higher detection efficiency on the simulation ($\sim$60 %) than on the neutron source data ($\sim$50 %). While we suspect the neutron transport/capture physics model used in the simulation to be the major origin of the apparent data-simulation discrepancy, we suggest that the lack of source geometry and trigger in simulation can bias the simulated neutron detection efficiency.

Acknowledgements

I am truly grateful to my thesis advisor Prof. Kimihiro Okumura, for all the research opportunities he has provided me with and his insightful guidance that has kept me focused and motivated whenever needed, especially during the rather unfortunate year of 2020 possessed by a hopeless series of self-quarantine.

Dr. Takatomi Yano has led the AmBe neutron calibration campaign. The Automated Source Deployment System has made the calibration process so much easier, and a large amount of data could be taken regularly without much of a hassle, all thanks to the system that he has developed. I also thank him for convening the AmBe calibration meeting, and giving me tons of advice and insights that have helped me progress.

Prof. Yoshinari Hayato has guided me both as a mentor and an expert. I have learned much about the detector, simulation, and analysis software from the Okayama group, namely, Prof. Yusuke Koshio, Dr. Kaito Hagiwara, and Masayuki Harada. Masayuki Harada has been the most inspiring colleauge with whom I discussed most of the topics covered in this thesis.

The SK simulation tool `skdetsim` has been developed by the SK collaborators for more than 20 years. Prof. Kimihiro Okumura, Prof. Yusuke Koshio, and Dr. Patrick de Perio has helped me learn how to use it. `skdetsim-skgd`, the Geant4 neutron capture model attachment to `skdetsim`, has been developed by Dr. Tsui Ka Ming, Dr. Yosuke Ashida, Dr. Ryosuke Akutsu, and Masayuki Harada. `SKG4`, the Geant4-based SK simulator that I used to estimate the amount of neutron-induced BGO scintillation within the triggered data is a work of Dr. Kaito Hagiwara, Masayuki Harada, Dr. Guillaume Pronost, Seiya Sakai, Shotaro Yamamoto, Prof. Yusuke Koshio, and myself. The neutron tagging software that I have developed for this study is based on the toy tagging program made by Dr. Tsui Ka Ming.

Most of the analysis presented in this thesis is either preceded (for the pure-water phase) or inspired by the discussions given in the works of Dr. Tristan James Irvine [1], Dr. Tsui Ka Ming [2], Toshiki Mochizuki [3], and Dr. Ryosuke Akutsu [4].

I would like to thank Prof. Hiroyuki Sekiya, Dr. Hiroshi Ito, Dr. Yasuhiro Nakajima, Dr. Kiseki Nakamura, Dr. Linyan Wan, Akira Takenaka, Shintaro Miki, and Shuehei Watanabe for discussion and comments relevant to this work.

I would like to express my gratitude to the Gd-loading team/shifts and all SK collaborators, for working hard day and night to successfully load Gd and keep the detector running. I deeply appreciate the Japanese Ministry of Education and Culture, Sports, Science and Technology for financial support, without which I could not have been a part of this brilliant collaboration.

Special thanks goes to the fellow members of the ICRR neutrino group and the Kamioka Observatory, without whom my student life would have been miserable: Dr. Guillermo Daniel Megías Vázquez, Dr. Ryosuke Akutsu, Junjie Xia, Dr. Hiroshi Ito, Dr. Kiseki Nakamura, Yutaro Sonoda, Akira Takenaka, Kohei Okamoto, Yu-chin Chen, Shuichi Imaizumi, Takeshi Okada, Yoshiki Nagao, Minato Shibata, Yuki Kanemura, Shintaro Miki, and Shuhei Watanabe.

Final thanks goes to my family, friends, and everyone who has supported me along the way.

Contents

List of Tables

List of Figures

Chapter 1

Introduction

The Super-Kamiokande (SK) experiment was designed to explore realms of physics that have never been known to mankind, by searching for hints of phenomena that should be either non-existent or extremely faint, with a gigantic water Cherenkov detector. By detecting supernova burst neutrinos [5] and finding evidence of atmospheric neutrino oscillation [6], the water Cherenkov detector technique employed by SK has been proven more than just cost-effective, still running for over 20 years while constantly updating the borderline of physics. Having cleared two Nobel-prize-winning problems already, SK now aims to search for the remaining hidden secrets of the universe: the Supernova Relic Neutrinos (SRNs), neutrino CP-violation, and proton decays. All of these unknowns hold keys to the origin of the matter and the universe.

The following is a brief summary of the above three physics programs:

- Supernova Relic Neutrinos (SRNs)

  Detectable supernova bursts within our galaxy are fairly rare ($O(1)$/century), but supernovae themselves are not ($O(1)$/s). Considering the burst neutrino flux and the extremely low interaction cross section of neutrinos, our universe should be suffused with the remnant neutrinos from all supernova explosions that has happened so far. By measuring the SRN flux, one can investigate the mechanisms of nucleosynthesis and stellar evolution, and test the well-established supernova neutrino emission model as well.

- Neutrino CP-violation (CPV)

  CPV represents the matter-antimmatter asymmetry, which should exist to explain the matter-dominant universe. It was discovered that quarks indeed violate CP-symmetry via weak interaction, but the amount of quark CPV is insufficient to explain the baryogenesis. The remaining source of CPV is the neutrino, whose three generations and the non-zero/non-degenerate masses confirmed by neutrino oscillation should enable CPV. The neutrino CPV in experiments manifests itself as a difference between neutrino and antineutrino oscillation probability. The neutrino oscillation is detailed in Appendix A.

- Proton decay

  The Standard Model conserves the baryon number, so that a free proton, the lightest baryon to exist, can never decay on its own to form a non-baryonic matter. However, the baryon number violation is one of the so-called "Sakharov conditions" [7] that are necessary to explain the baryogenesis. Most grand unified theories (GUTs) explicitly break baryon number conservation to predict a proton decay process, e.g., $p \rightarrow e^+ + \pi^0$ with lifetime of $O(10^{30})$ to $O(10^{36})$ years.

The SK detector is explained in Chapter 2.

Unfortunately, with the current detector sensitivity, it may take another 20 years to gather statistics to an amount required to prove the existence of the above-mentioned phenomena. To boost sensitivity to its target physics, SK has chosen to load Gadolinium (Gd), the most neutron-absorbing element known, to its pure-water volume. Why? To detect neutrons, of course. Detecting neutrons, one of the most studied particles in the universe, to identify the rarest types of events in physics history, may sound too simple; but even the first discoverers [8] of neutrinos have employed neutrons to identify neutrinos! Besides, in liquid scintillators for neutrino physics, loading Gd has become quite an established techinque. So, why neutrons all of a sudden? What do they have to do with the rare physics that we pursue?

1.1 Why neutrons?

Some of the neutron's importance in the search for rare physics comes from the characteristics of the water Cherenkov detector. With water Cherenkov detectors, it is difficult to detect heavy charged particles due to high Cherenkov threshold (1.4 GeV for protons) that increases with particle mass. Neutrons are the only exception, as they are never observed via Cherenkov radiation, but are detected via capture (i.e., absorption, or (n, γ)) reactions that produce observable gamma-rays. Hence in water Cherenkov detectors, neutrons are practically the only long-lived hadrons that can be detected regardless of energy.

The physical importance of neutrons stems from the fact that they are copiously produced via neutrino interactions in matter. Apart from protons that are rarely visible in SK, neutrons are the most abundantly produced nucleons in neutrino interaction. Yet, the detection efficiency is low in pure water, because of the low binding energy (2.2 MeV) of deuterons produced in the middle of the $p(n, \gamma)$ reaction. By counting the number of detected neutrons produced in one interaction, we could better classify and reconstruct the event topology, thus improving sensitivity to the rare physics.

Here are some benefits we expect from detecting neutrons in SK:

- SRN search

  The dominant interaction of electron neutrinos in the SRN energy range (10 - 60 MeV) is the so-called "inverse beta decay" (IBD, $\bar{\nu_e} + p \rightarrow e^+ + n$) on a free proton. Unfortunately, there are several sources of backgrounds, especially the solar and atmospheric neutrinos that can mimic the IBD in a conventional pure-water Cherenkov detector with minimal neutron detection capability. For example, an "invisible muon" event, where a low-energy (below Cherenkov threshold) neutrino-induced muon decays into an electron with itself undetected, has the same observable particles and thus becomes indistinguishable from signal (IBD) events. Another possibility of fake SRN events is a scenario where ν_e elastically scatters a bound electron. The SRNs are expected to be far outnumbered by such backgrounds. The estimated flux distributions of signal SRN and its backgrounds

are shown in Figure 1.1. If we could efficiently detect neutrons from data, then the aforementioned most dominant backgrounds that do not necessarily produce neutrons should be largely removable from analysis by requiring a neutron. We could also improve the supernova direction reconstruction, as we could purify the SRN scattering events where forward-scattered electrons keep the direction of the SRNs, from the SRN IBD events where neutrons obscure the original SRN direction.

- Neutrino CPV search and oscillation analysis

  Neutrino CPV search is a part of the neutrino oscillation analysis, which is a process that estimates the neutrino oscillation parameters by fitting a parameterized "oscillated" (i.e., predicted by the oscillation probability with a given set of oscillation parameters, the current knowledge on neutrino cross sections, and the estimated initial neutrino flux) neutrino energy spectrum to the one measured in data. For a brief introduction to the oscillation probability and parameters, refer to Appendix A.

  The neutrino sources used in the SK oscillation analysis are atmospheric, accelerator, and solar neutrinos, each with distinct ranges of energy and path length. The main target interaction in the oscillation analysis is the charged-current quasi-elastic (CCQE, $\nu_l + n \to l^- + p$ for neutrinos and $\bar{\nu}_l + p \to l^+ + n$ for antineutrinos, with flavor $l \in \{e, \mu, \tau\}$) interaction, which gives out the interacting neutrino's flavor by producing a same-flavored lepton. The SK detector is capable of separating electrons from muons as illustrated in Figure 2.2, so that we can estimate the counts of e-like and μ-like CCQE events within the detector. Neutral-current (NC) neutrino scattering on a bound electron can be a source of background, since the scattered electron does not carry any flavor information. Requiring a neutron from an event sample can help remove this background, which is especially dominant for low-energy solar antineutrinos.

  Another necessity of neutron detection in SK is supported by the fact that in SK, detecting final-state neutrons is practically the only way of distinguishing antineutrinos from neutrinos. (Recall that only antineutrinos emit neutrons via CCQE interaction.) The $\nu/\bar{\nu}$ separability is especially important for atmospheric neutrino analysis, in which we expect both neutrinos and antineutrinos in comparable amounts. With greater neutron

detection efficiency, we expect improved sensitivity to neutrino mass hierarchy (MH) in atmospheric analysis [1]. MH is important, since it is correlated to the overall oscillation analysis including the CPV search. Refer to Appendix A for MH. For accelerator neutrino analysis, the advantage of the separability is relatively small compared to that in the atmospheric analysis because the initial $\nu/\bar{\nu}$ flux can be controlled. Still, accidental wrong-sign backgrounds can be efficiently removed via neutron detection to improve the accelerator analysis' sensitivity to CPV.

Another expected advantage lies in the neutrino energy reconstruction. The initial neutrino energy spectrum in typical oscillation analysis is quite wide ($O(0.1)$ GeV for accelerator experiments, to say the least), while the oscillation probability depends on the incident neutrino energy. For this reason, precision in the energy reconstruction should be critical to the oscillation parameter estimation. Multiple neutrons produced by the intranuclear cascade of hadronic interaction should carry a part of the neutrino energy, which should be possible to retrieve if we could efficiently detect neutrons.

- Proton decay search

  If proton decays were to occur via $p \to e^+ + \pi^0$ in the SK detector, there would be ideally an event with three electron-like rings, one created by the positron and the other two imprinted by the two gamma-rays from the instantaneously decaying π^0. Atmospheric neutrinos can fake the event topology by producing a charged lepton and a π^0 (via either primary νN interactions, FSI, or SI explained in Section 1.3) within the detector, and requiring zero detected neutron in the sample can efficiently reject this background.

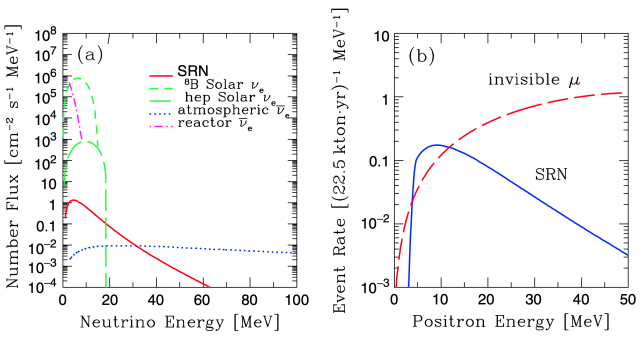

Figure 1.1: (a) number flux of SRNs compared with other background neutrinos, and (b) event rate of SRNs and invisible muon decay products. Reprinted from Ref. [9]

1.2 Neutron production in SK

The background neutrons to the SK detector are mainly produced via spallation, where high energy cosmic rays inelastically reacts with matter nuclei to scatter off a large number of nucleons. Hadronic particles, such as neutrons themselves, protons, alpha particles, and pions can also interact with nuclei to free bound neutrons. Another background radioactivity is spontaneous fission, in which a heavy nuclide spontaneously undergoes nuclear fission to emit neutrons. A small number of ^{238}U contained in Gd salt is subject to this process, although its contribution to the background neutrons should be negligible due to its very long half-life ($O(10^9)$ years).

Neutrons can also be produced via neutrino-nucleus interaction. The following is the summary of the three stages in which neutrons can be produced:

- Primary νN interaction:

  Antineutrinos can primarily undergo a CC or NC exchange with nuclei to knock out a neutron, where neutrinos can knock out neutrons via NC exchange only. Both types with a higher energy can also excite the nucleon to a baryonic resonance state (RES), which immediately de-excite to a nucleon and produce pions, kaons, and gamma-rays. At even higher energies, neutrinos can scatter off a single quark to produce more hadrons (DIS).

- FSI (Final-state interactions)

  The final-states of the primary νN interaction (mostly nucleons and hadrons) are very likely to undergo strong interaction within the nucleus, to produce even more hadrons.

- SI (Secondary interactions)

  Knockout nucleons and other hadrons (mostly pions) produced within the nucleus can further interact with the other surrounding nuclei even after they exit the primary nucleus.

Figure 1.2 shows how the FSI/SI can obscure the final neutron multiplicity in CCQE samples. Nonetheless, a non-zero multiplicity proves to be an effective indicator of $\bar{\nu}$-CCQE.

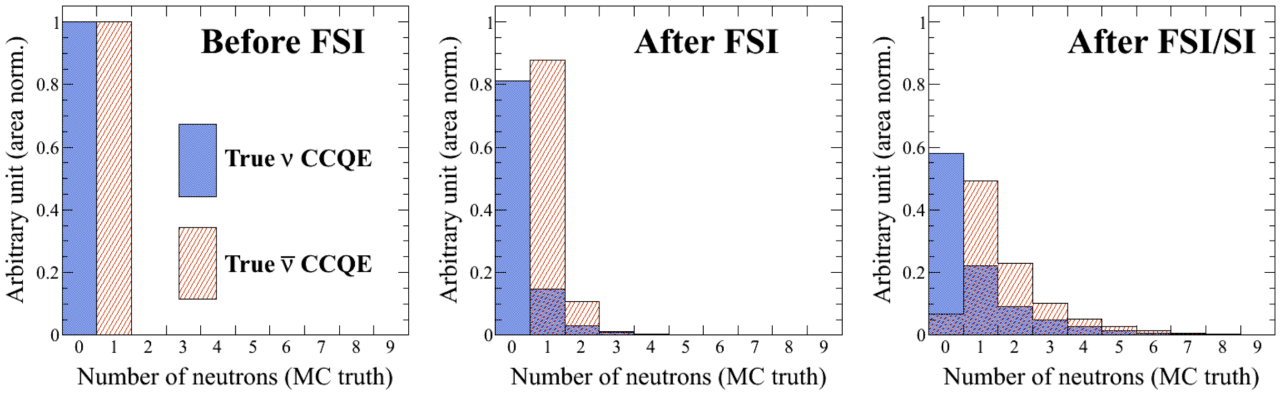

Figure 1.2: Simulated $\nu/\bar{\nu}$ CCQE neutron multiplicity distributions from primary νN interaction (left), from νN interaction including FSIs (center), and for νN interaction including both FSIs and SIs (right). Reprinted from Ref. [4].

1.3 Neutron reactions in Gd-loaded water

Neutrons are charge-neutral, so that they do not undergo Coulomb interaction, but only strong interaction with nuclei in extreme proximity ($\sim O(1)$ fm). Due to such property, neutrons are more penetrable than other charged particles of similar mass. Moreover, due to their gas/wave-like properties at lower energies, neutrons are often described using optical and thermodynamic models. It is conventional to classify neutrons by their kinetic energy as follows:

- Cold neutrons (K.E. < 0.025 eV)

  Cold neutrons are neutrons slower than most neutrons at room temperature (290 K). Ultracold ($< O(100)$ neV) neutrons are subject to total reflection upon matter nuclei with high optical potential, so that they can be treated as ideal gas. Cold neutrons are widely used in the study of internal crystal structure of solids, as well as in precision measurements of free neutron properties such as electron dipole moment. Despite their physical versatility, their preponderance within SK ($\sim$285 K) should be negligible.

- Thermal neutrons (K.E. $\sim$0.025 eV)

  Thermal neutrons are neutrons with kinetic energy close to the mode ($\sim$25 meV) of the Maxwell–Boltzmann distribution at around room temperature ($\sim$290 K). For neutrons within SK, this energy range is practically the lower limit they can reach. Thermal neutrons have wavelengths of $O(0.1)$ nm.

- Fast neutrons (1 < K.E. < 20 MeV)

  Fast neutrons with kinetic energy of $O(1)$ MeV are often products of nuclear fission and cosmic spallation. Many of the neutrons produced by high energy hadronic scattering (including νN interaction) are expected to fall into this range.

We expect most of the neutrons produced in SK to have kinetic energy ranging from fast to thermal. The neutron-nuclear reactions can be categorized into two types, according to their interaction times [10]:

- Direct reaction

  A direct reaction can occur when a projectile neutron has enough kinetic energy to have a wavelength of $O(1)$ fm (i.e., $\sim$20 MeV nucleon) and a relatively large impact parameter, so that it can interact with a single valence nucleon of the target nucleus. The unstable bound state of the incident neutron and the valence nucleon typically lives for about 10^{-22} s, which is in the order of time required to make several round trips (in classical terms) around the nucleus, before one of the projectile neutron and the nucleon finds a way to escape. The ejected particle is generally forwardly-directed with strong angular correlation, following the energy-momentum conservation.

- Compound Nucleus (CN) reaction

  When the projectile neutron collides with a nucleus with a small impact parameter, it interacts many times inside the nucleus, boosting individual nucleons into excited states, until it comes to rest inside the nucleus. The thermal equilibrium model is used to model such nuclear reactions. The excess energy introduced to the "compound nucleus" by the incident neutron is shared by many of the bound nucleons via multiple intranuclear scatterings, so the de-excitation probability of one specific nucleon to gain a large enough share of the energy to escape becomes statistically small. Such statistical constraint makes the overall lifetime of the CN to be $O(10^{-18})$ to $O(10^{-16})$ s, which is substantially longer than that of direct reactions. The angular distribution of the products are nearly isotropic, owing to the random intranuclear interactions, especially for light projectiles.

Neutrons produced within the SK detector loaded with Gd can undergo both direct and CN reactions with matter nuclei. In pure water, the most dominant direct reaction channel for neutrons with kinetic energy below 20 MeV is the elastic scattering with free protons (i.e., $p(n,n)p$). Refer to Figure 1.3 for the cross sections. The elastic scattering of an energetic neutron within the sea of free protons at rest quickly moderates the neutron down to the thermal regime within a few µs.[1] A moderated neutron is mostly captured by a proton to form a deuteron[2], emitting the excess 2.2 MeV binding energy as a form of a monoenergetic gamma-ray. This absorption process can be viewed as a CN reaction where the CN is the deuteron and the lifetime is infinite (stable), so that the radiation is almost isotropic.

In case a small amount of Gd is dissolved in water, Gd can also capture a fraction of moderated neutrons, as Gd has a few order of magnitude higher absorption cross section than ^{1}H or ^{16}O. The fraction of captures on Gd with varying Gd mass fraction in water is shown in Figure 1.5. The radiative neutron capture on Gd (i.e., $\mathrm{Gd}(n,\gamma)$) is an example of a CN reaction, where the CN in thermal equilibrium de-excites via emitting multiple gamma-rays. In case of the most naturally abundant and most strongly absorbing ^{157}Gd, the capture formula is $^{157}\mathrm{Gd} + n \rightarrow {}^{158}\mathrm{Gd}^{*} \rightarrow {}^{158}\mathrm{Gd} + \gamma$ (7.94 MeV). The total radiated energy of 7.94 MeV is the mass difference between the initial and final states, and is shared by multiple gamma-rays that are successively emitted in the process of multi-level de-excitation. The schematic of the process is shown in Figure 1.6. The energy distribution of the gamma-rays is random in nature, although there is a high chance of producing multiple low-energy gamma-rays due to the existence of quasi-continuum levels as shown in Figure 1.6.

Although most neutrons are expected to be thermally captured via either $p(n,\gamma)$ or $\mathrm{Gd}(n,\gamma)$, a small fraction (∼2 % or below according to the simulation explained in Section 3.1) may undergo inelastic interactions before they thermalize, sometimes multiplying or removing the incident neutron. The cross sections are shown in Figure 1.4. While quantitative evaluation of those channels is necessary, we focus on $p(n,\gamma)$ and $\mathrm{Gd}(n,\gamma)$ reactions of moderated neutrons.

[1] ^{1}H is actually the most effective nuclide in moderating energetic neutrons. The mean logarithmic reduction of neutron energy per collision is described as $< \xi >=< \ln \frac{E_0}{E} >= 1 + \frac{(A-1)^2}{2A} \ln \frac{A-1}{A+1} \approx \frac{2}{A}$ [11], where A is the mass number of the target nuclide.

[2] The thermal neutron capture cross section on ^{16}O is negligible compared to that on ^{1}H.

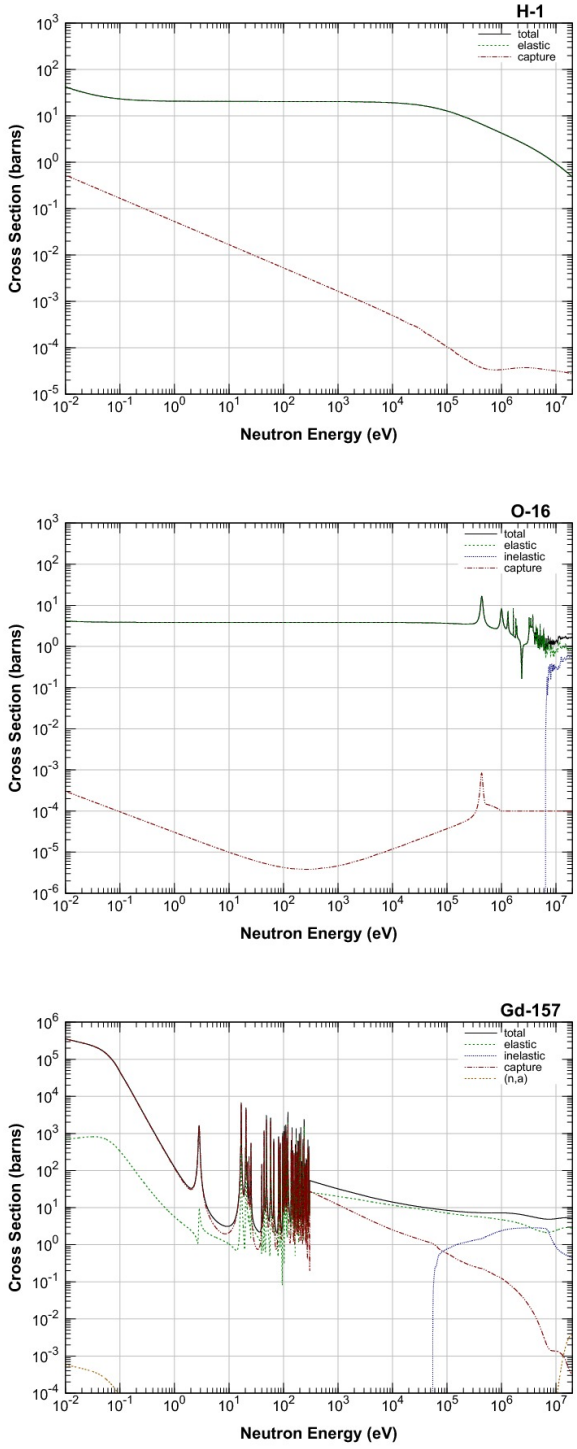

Figure 1.3: Neutron cross sections on ^{1}H, ^{16}O, and ^{155}Gd from the JENDL-4.0 library [12]. Neutrons are more likely to be captured with lower kinetic energy, qualitatively as they tend to spend more time in the vicinity of nuclei with lower speed. The large fluctuation in the intermediate energy range can be understood as manifestation of resonances in the distinguishable discrete energy levels. A formal approach can be found in Ref. [10].

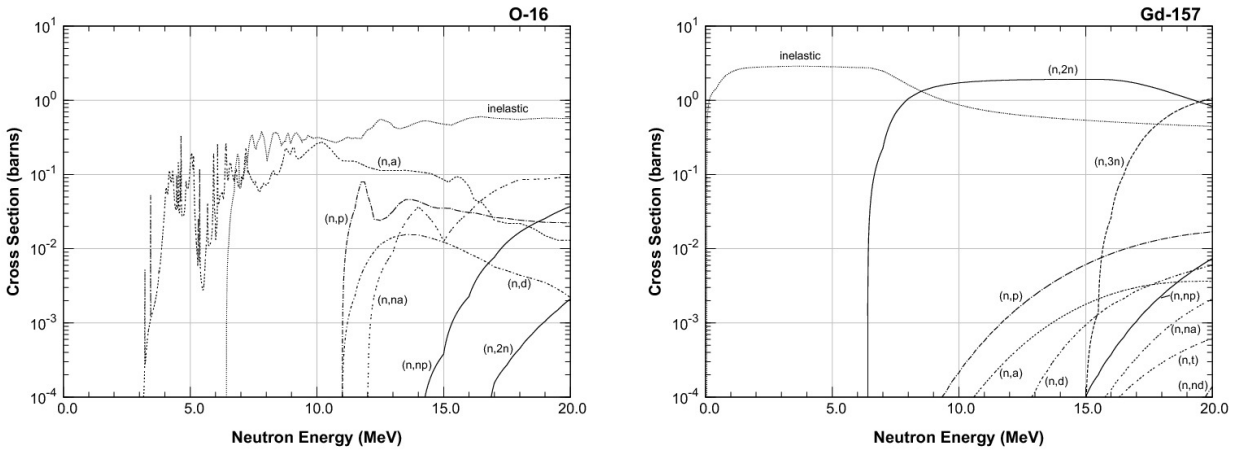

Figure 1.4: Neutron reaction cross sections on ^{16}O and ^{155}Gd, from the JENDL-4.0 library [12]. Note the small fraction of channels either removing or multiplying the number of neutrons.

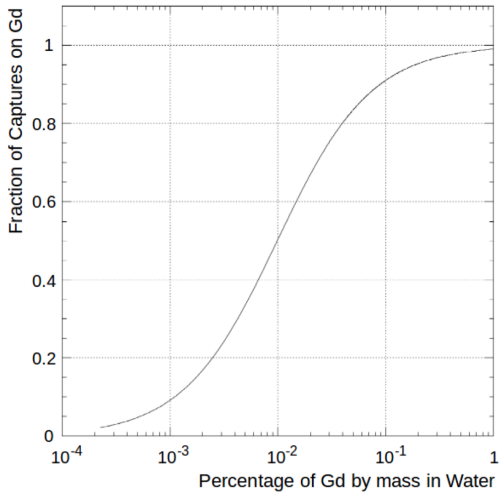

Figure 1.5: Capture ratio on Gd, by Gd mass fraction in water. Reprinted from Ref. [13].

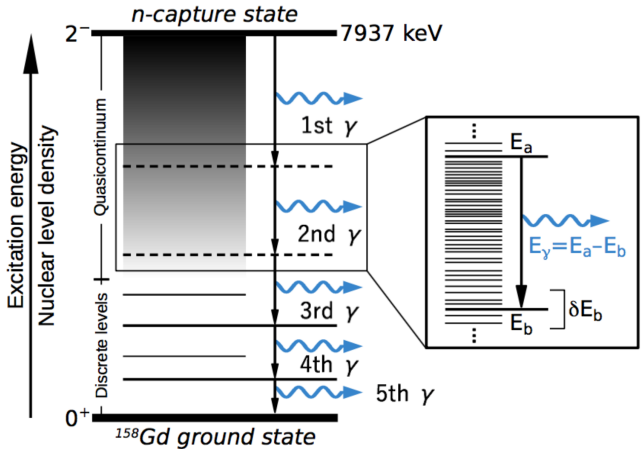

Figure 1.6: The de-excitation schematic of the excited state $^{157}\mathrm{Gd} + n \rightarrow {}^{158}\mathrm{Gd}^*$ to the ^{158}Gd ground state. Multiple gamma-rays from the $^{157}\mathrm{Gd}(n,\gamma)^{158}\mathrm{Gd}$ reaction can share 7.937 MeV. Reprinted from Ref. [14].

1.4 Outline of this study

With high neutron detection efficiency brought forth by dissolving Gd into the SK's detector volume, we expect to improve background rejection as explained in Section 1.1. The SK-Gd phase has officially started since July 2020 with Gd mass fraction of 0.0110 wt.%, and we need to evaluate the change in neutron detection efficiency.

SK already has the so-called "neutron-tagging" algorithm that has been used to detect neutrons in pure-water data. The workflow of this algorithm involves a multivariate analysis technique where we evaluate the signal likelihood of unseen data with an artificial neural network trained with labeled data extracted from the detector simulation. The process is detailed in Section 3, and the method has been proven valid for $p(n, \gamma)$ detection in pure water [1, 3, 4]. In this study, we take the same approach to the Gd-loaded data as well, but this time, we optimize the relevant parameters to the SK-Gd simulation that has become ready for use and validation. The tuned algorithm was applied to a neutron source data, to evaluate the neutron detection efficiency of the Gd-loaded detector and the reproducibility of the data with the simulation. The analysis process and the results are discussed in Section 4.

Chapter 2

The Super-Kamiokande detector

The Super-Kamiokande (SK) detector is an underground water Cherenkov detector, which as the name suggests, detects Cherenkov light emitted in water. When a charged particle passes through a dielectric (polarizable) medium, it can electromagnetically interact with the surrounding molecules to excite them and make them radiate. In case the particle travels faster than the phase velocity of electromagnetic wave in the medium, simultaneous radiation from different positions can share the wavefront to form a sort of shock-wave of angle $\theta = \cos^{-1}(\beta/n)$. The phenomenon itself and its anisotropy was first discovered by P. A. Cherenkov [15] for whom the phenomenon was named. The schematic is shown in Figure 2.1.

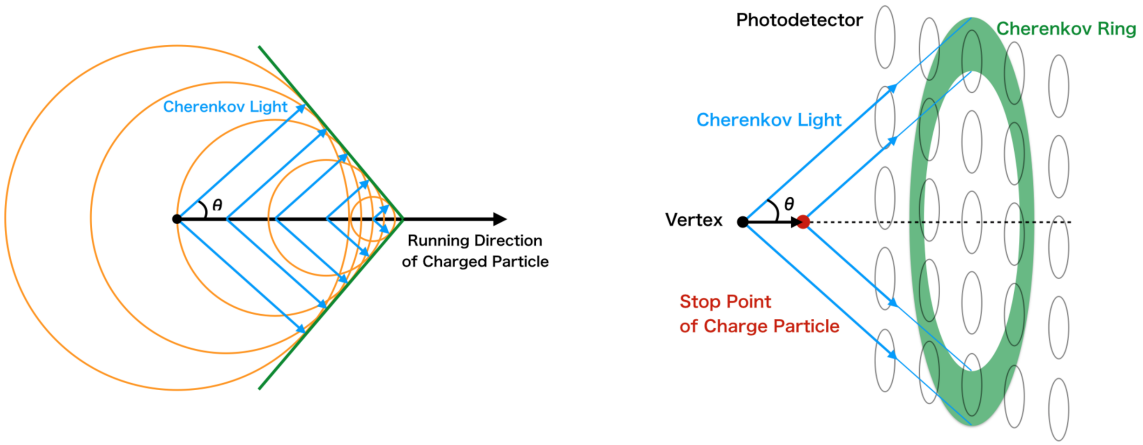

Figure 2.1: Schematics of Cherenkov radiation (left) and how it forms a ring-shaped image on a photodetector plane (right). Reprinted from Ref. [16].

The energy radiated per track length is modeled by the Frank-Tamm formula (in cgs) [17]

$$\frac{dE}{dx} = \frac{(ze)^2}{c^2} \int_{\epsilon(\omega)>1/\beta^2} \omega \left(1 - \frac{1}{\beta^2 \epsilon(\omega)}\right) d\omega \tag{2.1}$$

where ze and β are each the charge and the speed (v/c) of the moving particle, ϵ is the permittivity of the medium, ω is the frequency of the radiation (assuming magnetic permeability $\mu(\omega) = 1$ so that $n(\omega) = \sqrt{\epsilon(\omega)}$). For an ultrarelativistic particle of $\beta \approx 1$, the energy loss per path length dE/dx in Equation 2.1 and the Cherenkov angle $\theta = \cos^{-1}(\beta/n)$ shown in Figure 2.1 are almost fixed, given the particle charge and the dielectric properties of the medium. For instance, the energy loss due to an ultrarelativistic particle with unit charge passing through water where the Cherenkov angle θ is $\sim 42^\circ$ is $O(1)$ keV/cm.

Since the Cherenkov radiation stops as the particle is slowed down below the Cherenkov threshold speed of $\beta_{\min} = 1/n$, the radiation from most charged particles with moderate energies are ring-shaped, as illustrated in Figure 2.1. Hence, if we create a photodetector plane as in Figure 2.1 to measure the radius of the ring and estimate the amount of radiated photons, we can technically reconstruct the position and the energy of the incoming charged particle. Although the energy deposited to the detector system via Cherenkov radiation is extremely small (less than 1 %) compared to the energy lost by ionization[1], reconstructing an event from detected Cherenkov light is a practical option for a gigantic detector with zero net electromagnetic field. A disadvantage to this technique is that the Cherenkov light from heavy particles is often barely visible at best due to the energy threshold of Cherenkov radiation increasing with particle mass.[2] This is an inevitable sacrifice in this technique whose priority is set to increasing neutrino event statistics. Fortunately, electrons and muons are detectable, and even separable with the water Cherenkov technique. Electrons are more likely to induce electromagnetic interactions including pair production and bremmstrahlung[3], so that the Cherenkov rings generated by electrons are often "fuzzier" than their muon counterparts. The "fuzziness" can be quantified, and be used as a particle identification discriminator as illustrated in Figure 2.2.

[1] For example, the total stopping power of $\sim$2 MeV/cm for minimum ionizing particle in water.
[2] 0.8 MeV for e, 160 MeV for μ, 210 MeV for π, 750 MeV for K, and 1.4 GeV for p.
[3] The critical energy of electrons in water is $\sim$70 MeV, whereas the same for muons are $\sim$1 TeV.

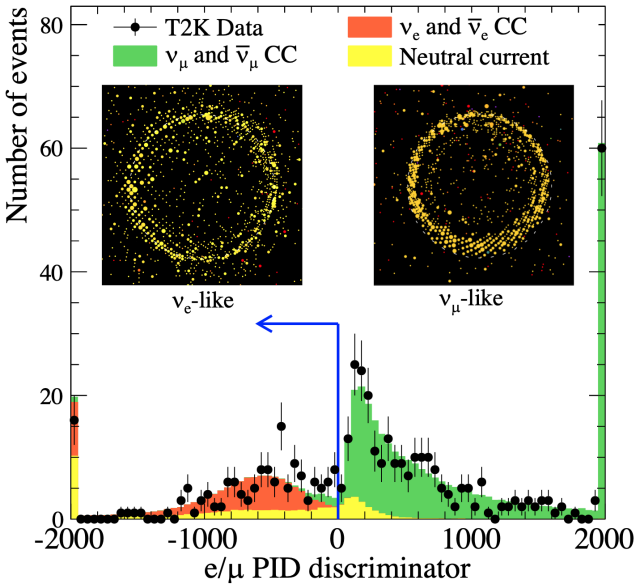

Figure 2.2: ν_e/ν_μ event identification amongst beam (T2K) neutrino data taken in SK, by the clarity of Cherenkov rings. Reprinted from Ref. [18].

2.1 Specification

The detector is as illustrated in Figure 2.3. The detector is located at 36°25'32.6" N, 137°18'37.1" E, about 1,000 m underground in the Mozumi Mine in Hida's Kamioka area with 2,700 m-water-equivalent (m.w.e.) mean overburden, which decreases the comsic ray flux by the factor of $O(10^{-5})$ compared to the sea level intensity.[4] The detectable background gamma-ray intensity ($E_\gamma > 0.5$ MeV) is $O(0.1)$ cm^2·s^{-1}·sr^{-1}, and the background neutron rate is $O(10^{-5})$ cm^2·s^{-1}.[5] The average atmospheric neutrino event rate is ∼8 per day.

The detector is cylinder-shaped, 39 m in diameter and 42 m in height. The inner photomultiplier tube (PMT) support structure divides the tank into two distinct, optically isolated volumes. The inner detector (ID) volume has dimensions of 33.8 m (diameter) by 36.2 m (height), containing 32 ktons of water and 11,146 inward-facing 50 cm PMTs (Hamamatsu R3600) on its inner wall. The inner wall except the PMTs is covered with black sheet to reduce reflection. The fiducial volume (FV) of the ID is defined as the cylindrical volume 2 m inward from the ID wall, and its total mass is 22.5 ktons. The mean distance from the inner tank wall to the outer wall is about 2.5 m.

[4]The cosmic muon flux at SK is $\sim O(10^{-7})$ cm^2·s^{-1}·sr^{-1}. (∼2 Hz event rate at the detector)
[5]The measurement was done before 1994.

The outer detector (OD) volume is instrumented with 1,885 outward-facing 20 cm PMTs (Hamamatsu R1408), serving as an active veto counter against incoming particles as well as a passive shield for neutrons and gamma-rays from the surrounding rocks. The OD region has a width of about ∼2 m with a total water mass of about 18 kilotons. The OD wall is covered with white Tyvek sheet to maximize reflection and photon detection efficiency.

The two detector volumes are isolated from each other with light-proof sheets covering both inner and outer surfaces of the PMT support structure. The ID PMTs are mounted on a 70 cm grid, with 7,650 on the barrel (side walls), 1,748 on the top, and the remaining 1,748 on the bottom. The effective photocoverage of the ID surface is ∼40 %. The schematic of the detector volumes is shown in Figure 2.4. The Cherenkov radiation induced by a charged particle moving inside the detector can trigger the detector (if it's strong enough) to imprint a ring-shaped image on the detector surface. In case the particle is created within the ID, there would be no simultaneously detected signal in the OD. Thus, neutrino-induced particles are without any OD signature, and a sample muon-neutrino CC event display is illustrated in Figure 2.5.

The detector should be calibrated every once in a while to understand the detector capability and keep it from changing over time. The optical parameters of water within the detector volume are calibrated using laser. The relative PMT gain and timing distributions is calibrated using a diffuser ball, which is a point light source with uniform intensity over all solid angles. The absolute energy scale of the PMTs are calibrated using various physical sources, including low-energy electrons from a linear accelerator and neutrons and the accompanied capture gamma-rays from a point source. Cosmic ray muons have a well-known energy distribution so that they are used to cross-check the calibration. The calibrated parameters are introduced to the detector simulation to maximize the reproducibility.

To minimize the signal distortion caused by the geomagnetic field (∼450 mG), 26 Helmholtz coils are lined up along the tank wall, reducing the net magnetic field to 50 mG.

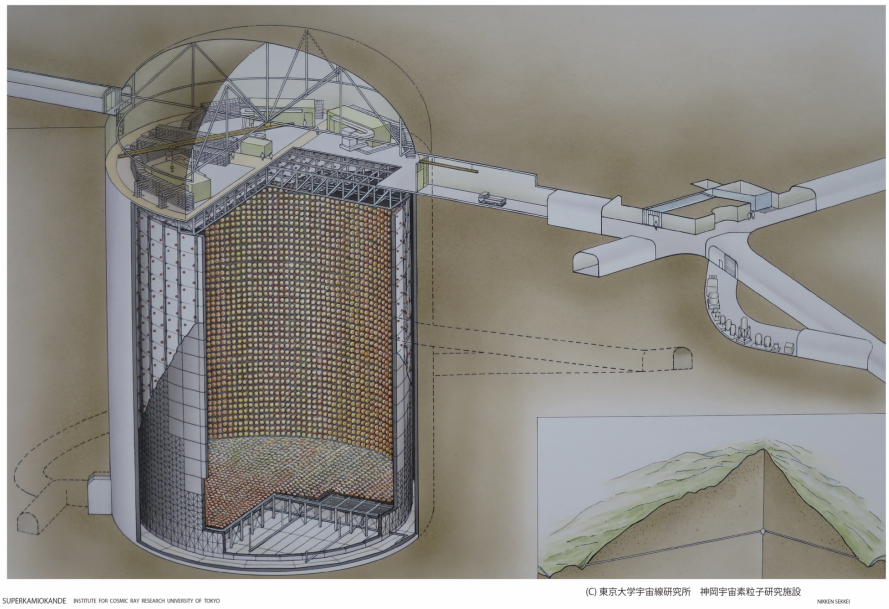

Figure 2.3: The SK detector.

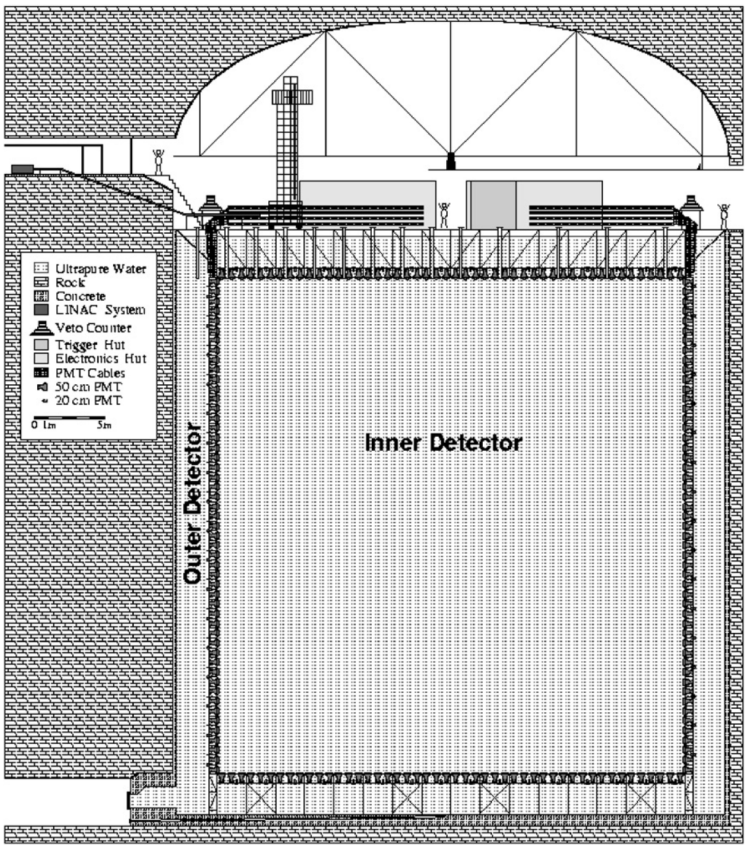

Figure 2.4: The schematic of the SK detector.

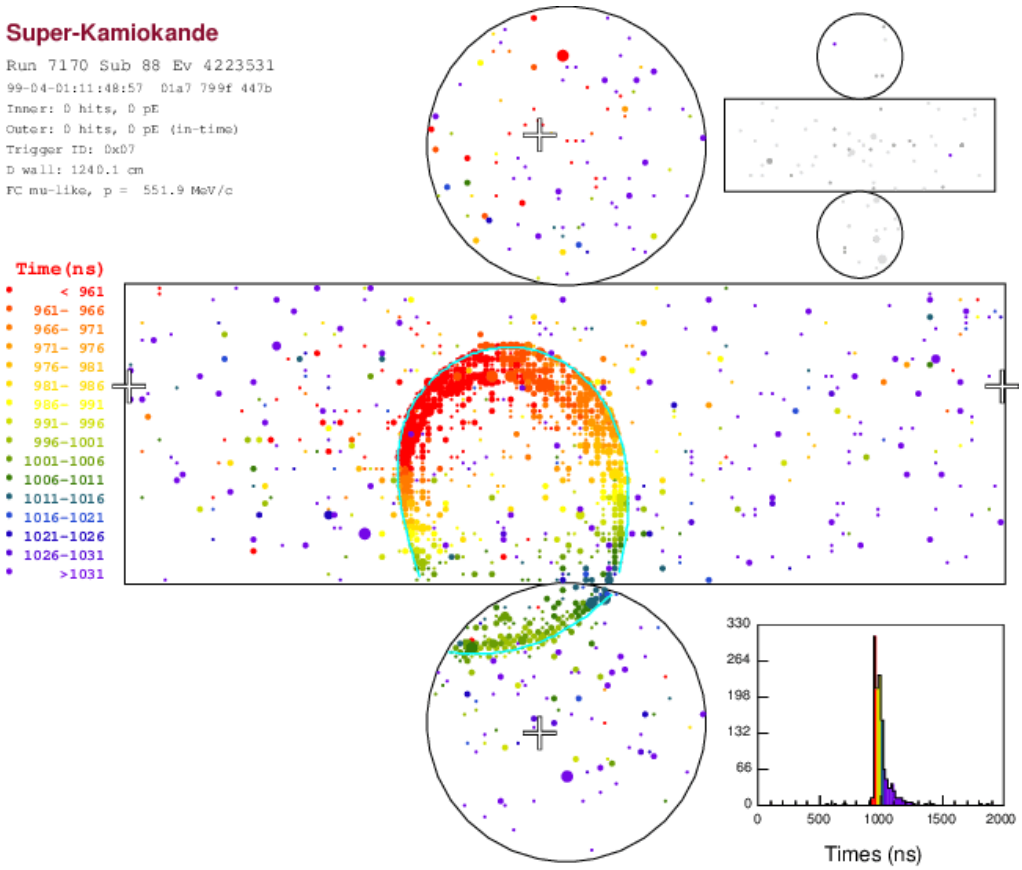

Figure 2.5: Sample event display of 0.6 GeV muon-neutrino.

2.1.1 ID PMTs and electronics

The ID PMTs are 50 cm Hamamatsu R3600 PMTs. The design is as shown in Figure 2.6. The photocathode of the ID PMT is coated with a bialkali (Sb–K–Cs) that matches the wavelength of the Cherenkov light. Its sensitivity range is 280 to 660 nm. The maximum quantum efficiency (QE) is about 21% at its peak (λ ~380 nm). The average collection efficiency at the first dynode is 70 %, which is uniform within ±7 % across the whole PMT surface. The dynode structure follows the Venetian Blind style, and the gain is 1×10^7 for 2,000-V high voltage. The relative transit time spread for the single photoelectron signal is about 2.2 ns (1σ). A PMT hit is defined as an individual signal pulse with over 0.25-photoelectron-equivalent charge deposit. The average dark-hit rate at the 0.25-photoelectron threshold is known to be 7 kHz.

The current signal from each ID PMT is sent to a QTC[6]-based Electronics with Ethernet (QBEE) system. The maximum detectable integrated charge without saturation for each PMT

[6]Charge-to-time converter.

is 2500 pC (equivalent to ∼1,300 photoelectrons). A time-to-digital converter (TDC) included in the system digitizes the time and deposited charge of each PMT hit, and send the information to online frontend PCs. Technically, all recorded hits are saved offline. A software trigger is applied to the recorded/sorted hits to issue an event.

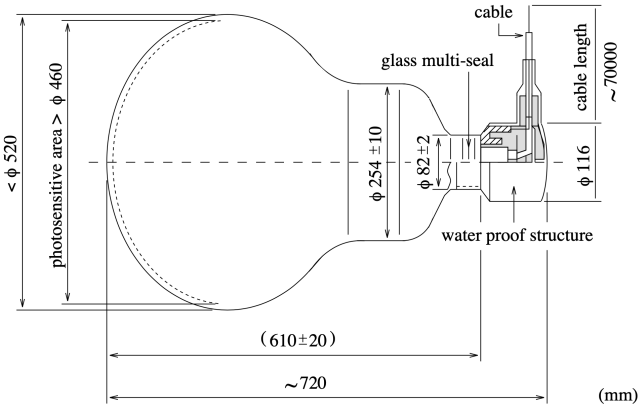

Figure 2.6: ID PMT.

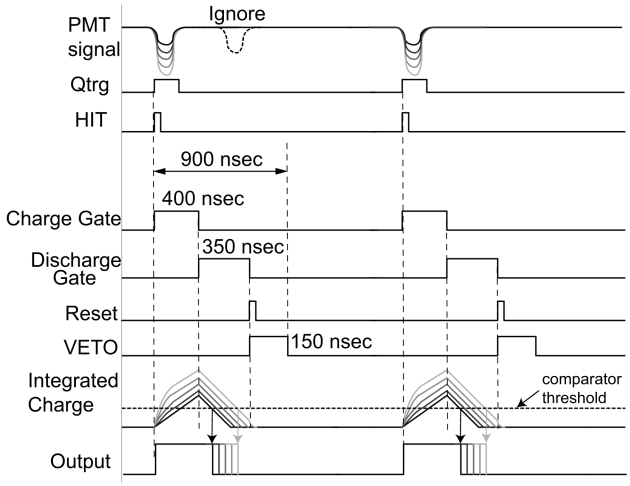

Figure 2.7: The schematic of gates issued after a PMT hit. The charging and discharging gates opens for 400 ns and 350 ns, respectively. All signal currents are ignored while one of the discharging gate and VETO is open. The total amount of time required to process a single input current is 900 ns. The timing of each hit is determined by the comparator threshold.

2.1.2 Water purification

The water that flows into the SK detector is taken from the mine, and it is critical to keep the water as pure and transparent as possible. Radioisotopes, notably Radon and Radium, are naturally dissolved in air and water. Such unwanted radioactivity increases noise hits and

mimics low-energy PMT hits such as neutron (n, γ) signals. For these reasons, the water within the detector is constantly circulated through a purification system at a flow rate of ∼50 tons/h.

The purification system has many stages, but they all boil down to three main objectives: filtering out particulates of finite size, controlling growth of bacteria, and reducing Radon contents through degasification. The purity of water is represented by the measured resisitivity. While the value before applying the purification system is typically about 11 MΩ·cm, the value after applying the system is 18.2 MΩ·cm, reaching the chemical limit of the ultra-pure water. The photon attenuation length at this state is ∼90 m.

2.1.3 Software trigger

Since all hits are saved offline, events are issued by "software" triggers. If the number of events within a certain 200-ns window is over a pre-defined threshold, records of PMT hits within the event window is set as one event. Table 2.1 summarizes the thresholds and the window widths for each event trigger type.

Trigger Type	Threshold [hits/200 ns]	Event window [µs]
Special High Energy (SHE)	58	[-5, +35]
High Energy (HE)	50	[-5, +35]
Low Energy (LE)	47	[-5, +35]
Super Low Energy (SLE)	31	[-0.5, +1.0]
Outer Detector (OD)	22 (in OD)	[-5, +35]

Table 2.1: Summary of the software trigger types.

For SHE triggers only, a special attachment flag named AFT (after-trigger) is raised in order to contain (n, γ) reactions that happen with a time constant of $O(100)$ µs, and additional 500-µs record of PMT hits is attached to the SHE-triggered event. The AFT attachment is not done for all SHE events, however, due to additional triggers near the primary SHE events.

Another special type of trigger is a random trigger, also known as the "dummy" trigger within SK. A "dummy" event is triggered by nothing but a clock with fixed frequency[7], so that it is typically used to model dark noise hits in the detector simulation.

[7]Usually this "clock" is set to the T2K beam frequency, but it can also be used as a "dummy" trigger in case the beam is off! Dummy-triggered events have an event window of [-500, +500] µs.

2.2 SK-Gd

13 tons of $Gd_2(SO_4)_3 \cdot 8\,H_2O$ was put into the tank via a dedicated dissolving system, starting from July 14th, 2020 until August 17th, 2020. The loaded amount corresponds to a 0.026 % concentration of $Gd_2(SO_4)_3 \cdot 8\,H_2O$ by weight dissolved in 50 ktons of total pure water in the detector system, and the concentration is equivalent to the Gd mass fraction of 0.0110 wt.%. The loaded Gd-sulfate and the amount loaded by date are shown in Figure 2.8.

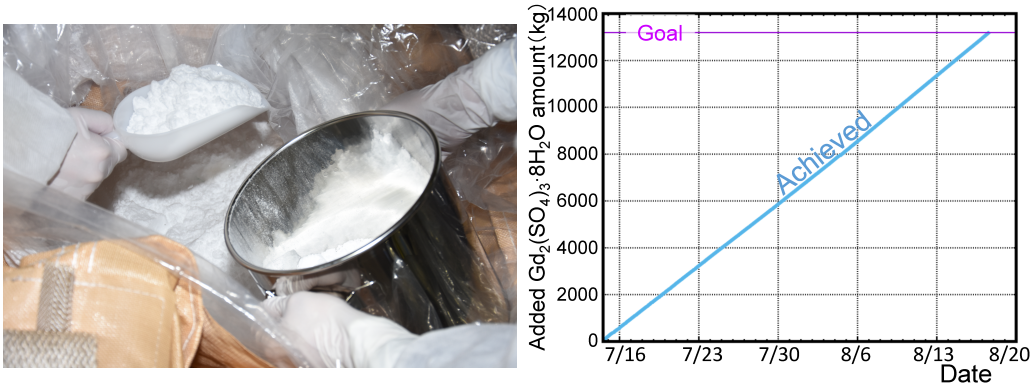

Figure 2.8: The $Gd_2(SO_4)_3 \cdot 8\,H_2O$ powder (left) and the amount of the Gd-sulfate loaded into the detector by date (right). Reprinted from Ref. [19].

A new Gd-loaded water purification and circulation system was developed to load Gd while maintaining the pure water transparency as is. To achieve this, a special ion exchange resin was introduced to remove all ionic impurities in water except Gd^{3+} and $SO_4{}^{2-}$.

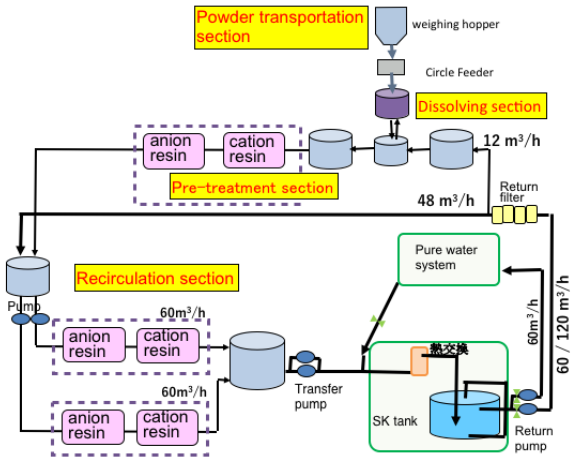

Figure 2.9: A block diagram of the Gd-dissolving system. Reprinted from Ref. [19].

Pure water was sent from the SK tank to the Gd-loading system at a flow rate of 60 tons/h.

The flow was separated into two streams, one at a rate of 48 tons/h, and the other at a rate of 12 tons/h into which the Gd-sulfate powder was dissolved. The $Gd_2(SO_4)_3 \cdot 8\,H_2O$ powder was put into the the powder feeder, and then sent to a pump for dissolving. The compound was circulated at a high speed within the dissolution tank, resulting in a 0.13 % $Gd_2(SO_4)_3 \cdot 8\,H_2O$ solution. The solution was purified in the "pre-treatment" section of the system, and merged with the 48 tons/h pure water stream to make a 0.026 % $Gd_2(SO_4)_3 \cdot 8\,H_2O$ solution. The final solution was sent to the SK tank using the "recirculation" section of the system, which continues to recirculate the SK water, even after the Gd loading was completed. The temperature of the supplied Gd water was set to about 0.3°C lower than that of the tank water just before the Gd-loading, to make it gradually fill the tank from the bottom. The overall system is as illustrated in Figure 2.9.

Since the Gd-loaded water was filled from the bottom, the concentration by height was measured using the Atomic Absorption Spectroscopy (AAS) technique[8] and the conductivity measurement. A sample of Gd-loaded water was taken from the tank with varying heights, and the Gd concentration was investigated daily during the Gd-loading phase. The results are shown in Figure 2.10. The Gd concentration at $z = 12$ m reaches ~250 ppm by August 14$^{\text{th}}$, 2020.

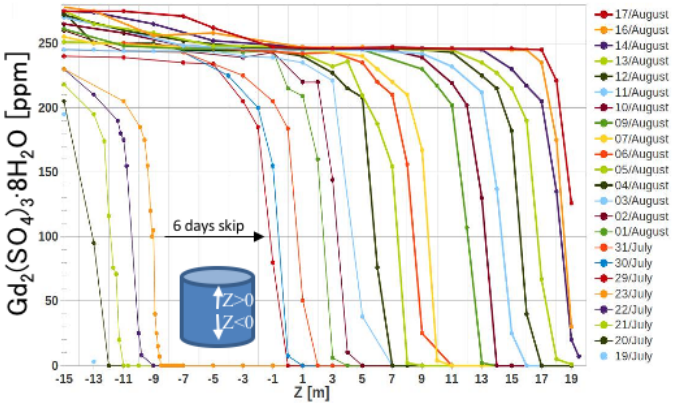

Figure 2.10: Measured Gd concentration by height and date. Reprinted from Ref. [19].

The neutron data used in this study was mainly taken during the 3-month commissioning phase (September - December, 2020) after the Gd-loading was completed.

[8]This technique makes use of the wavelengths of light specifically absorbed by a vaporized element, in our case, Gd.

Chapter 3

The neutron detection algorithm

Most neutrons produced within the SK detector eventually lose energy to be absorbed by an atomic nucleus within the tank volume. The compound nucleus that has absorbed a neutron immediately de-excites and emits one or several gamma-rays with a fixed sum of energy. If these gamma-rays scatter off a bound electron hard enough ($v_e > 0.75c$, $\mathrm{KE}_e > 0.8$ MeV) to generate Cherenkov photons, the PMTs on the inner surface of the tank will be able to detect them. We call such neutron-induced PMT hits a neutron capture signal, or in short, a neutron signal. A neutron capture signal might have only a couple of hits, or sometimes, more than a few dozen hits depending on the capturing nucleus and its position within the tank. The detector size of $O(10)$ m limits the hit time spread to be $O(100)$ ns. Figure 3.1 shows the number of PMT hits and the time spread distributions obtained from simulation for $p(n,\gamma)$ and $\mathrm{Gd}(n,\gamma)$ reactions, together which are expected to take up more than 99.98% of the total captures within ∼0.11 wt.% Gd-loaded water according to Table 3.1.

	n [/cm^3]	σ_{abs} [barns]	$n\sigma_{\mathrm{abs}}$ [10^{-5}/cm]
Gd	4.22×10^{14}	4.87×10^{4}	2.06
H	6.72×10^{19}	3.32×10^{-1}	2.23
O	3.36×10^{19}	1.90×10^{-4}	6.38×10^{-4}

Table 3.1: The number density n, the thermal neutron absorption cross section σ_{abs}, and their product $n\sigma_{\mathrm{abs}}$ for each of the top three neutron-absorbing elements: Gd, H, and O. The number densities are for 0.0110 wt.% Gd-loaded water and the cross sections are taken from the ENDF/B-VII.1 data [20]. The $n\sigma_{\mathrm{abs}}$ is equivalent to the capture rate per neutron path length.

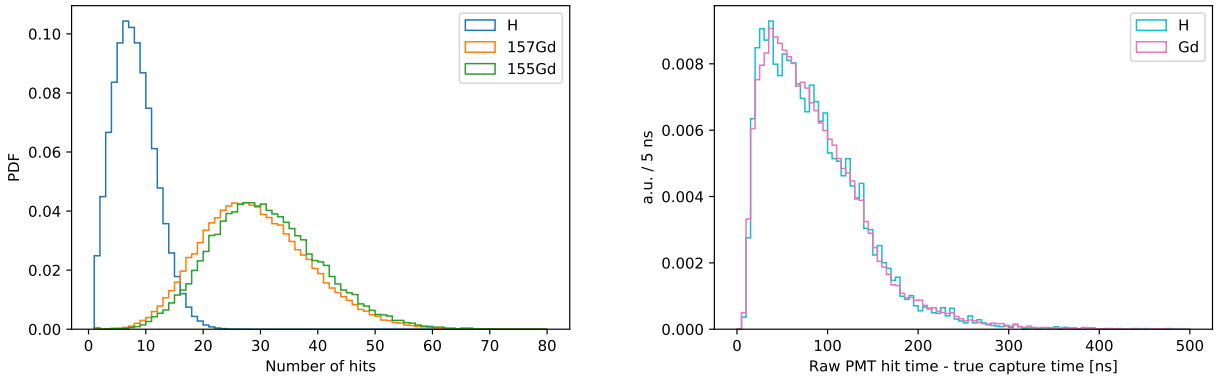

Figure 3.1: The number of hits (left) and the raw PMT hit time distributions (right) obtained from simulations for $p(n,\gamma)$ and $\mathrm{Gd}(n,\gamma)$ reactions. (random neutron vertex, area-normalized) The simulation configuration is as explained in Section 3.1.

Figuring out whether a set of PMT hits is coming from a neutron, given their number and time spread, is not an easy task, as the total of ∼12,000 PMTs would record on average 8 hits per 100 ns even without any external source. Such hits that originate from the detector itself or the surrounding environment are called the "dark" hits, and their primary source is the thermionic emissions (i.e., dark current) within each PMT. Dark hits would sometimes total up to 30 hits in a 100 ns interval, making it challenging for us to pick out neutron signals by their hit counts. If we were to do so, we would have to compromise between signal purity and detection efficiency. To maximize both, we need to find other distinctive features of signal hits.

Multivariate statistics has studied viable solutions to classifying unseen data by statistically analyzing the known feature distributions of different categories. The same problem is now widely addressed in machine learning and experimental particle physics as well, where classifying signals of physical interest is increasingly becoming difficult. For the past few years, SK has also tested a couple of multivariate analysis techniques such as a Multilayer Perceptron (MLP) [1] and Boosted Decision Trees (BDT) [2, 21] in identifying neutron captures within the pure water data and the simulated SK-Gd events. The methods have proven valid for neutron signal classification, and thus the same methodology was inherited and improved.

In this study, we target both $p(n,\gamma)$ and $\mathrm{Gd}(n,\gamma)$ signals, as the Gd-loading has just finished its commissioning phase with Gd concentration being ∼10% of the target value of 0.1 wt.%.

The author would like to clarify that designing the algorithm from scratch was not part of the author's original work. The author's contribution to this algorithm lies in developing an easily tunable program and optimizing it with simulation of the ∼0.0110 wt.% Gd-loaded detector. The improvements made by this study will be specified. The neutron detection program[1] has been fully re-written by the author.

The neutron detection algorithm used in SK neutron analysis consists of two stages. In the first stage, we look for a cluster of hits whose number and hit time distribution resemble those of signal hits. In the second stage, we statistically analyze each selected hit-cluster's features to examine its signal likelihood, using a multivariate analysis technique. The following subsections will discuss the specific design and the tuning process for each stage of the algorithm.

3.1 Signal properties of physics simulation models

Before testing and optimizing the neutron detection algorithm, the properties of signal hits were investigated with Monte Carlo (MC) simulation. The simulator `skdetsim-skgd` [22], whose framework other than the neutron capture models fully inherits `skdetsim`, was used to simulate neutron capture events. For low-energy ($KE_n < 20$ MeV) neutron transport, GCALOR (Geant-CALOR interface) is called [23]. For neutron captures, the same GCALOR is called for $p(n,\gamma)$ reaction, and the ANNRI-Gd model [24] based on the results of the ANNRI experiment [14, 25] at J-PARC is used for $\mathrm{Gd}(n,\gamma)$ reaction. There are a couple of caveats worth mentioning; the water parameters such as transparency and absorption lengths are tuned for pure water, and captures on nuclides other than Gd or H are not simulated. Noise hits are not simulated as well, but extracted from randomly sampled dummy trigger events taken at the end of the SK6 commissioning phase (Run 85200 - 85245), for more realistic reproduction of data events. A brief explanation on the dummy trigger can be found in Subsection 2.1.3.

[1] The code is maintained on a GitHub repository at `https://github.com/seunghophysics/NTag`. SK libraries and ROOT are required. Basic instructions can be found at `https://ntag.readthedocs.io`. For the API documentation, please refer to `https://www-sk.icrr.u-tokyo.ac.jp/~han/NTag/index.html`. (access to SK's internal network required)

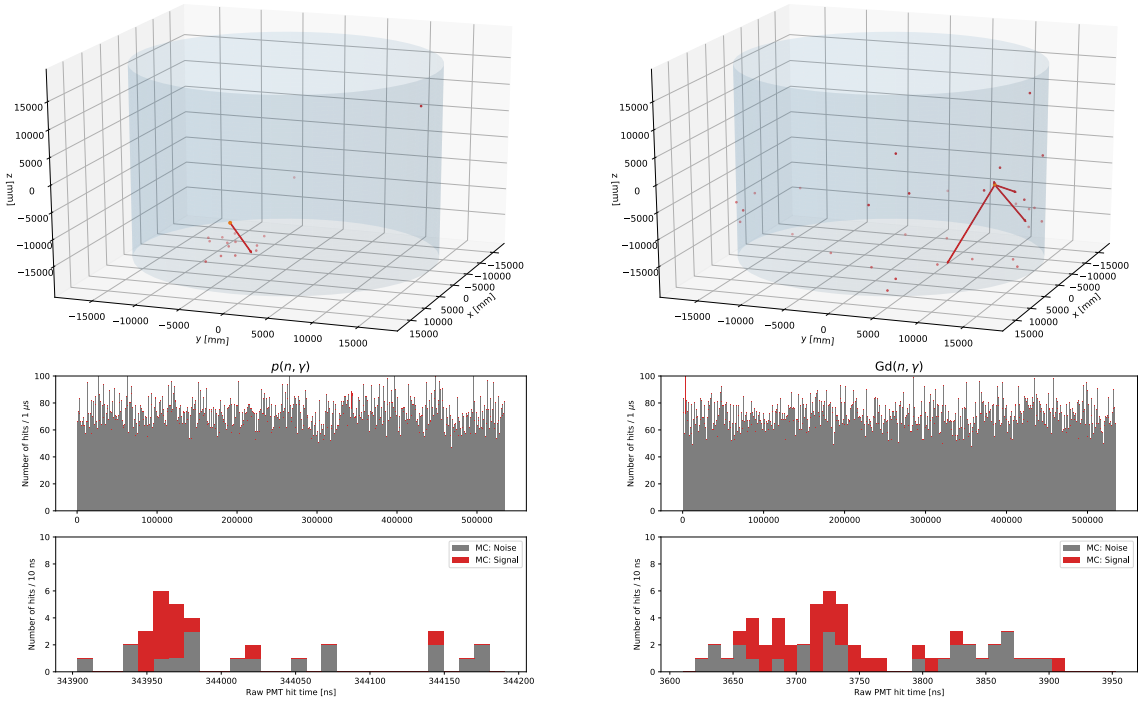

Figure 3.2: Sample MC event displays for a $p(n,\gamma)$ (left) and a $\mathrm{Gd}(n,\gamma)$ event (right). The top figures are the 3D drawings of the inner tank dimensions with all neutron signal hits (red dots) and gamma-rays (red arrows) in each event. The bottom histograms are the raw PMT hit time distributions of each event with bin width being 1 µs and 10 ns. The simulation configuration is as explained in Section 3.1.

Figure 3.2 shows sample displays of the simulated $p(n,\gamma)$ and $\mathrm{Gd}(n,\gamma)$ events. As can be inferred from the figure, the $p(n,\gamma)$ and $\mathrm{Gd}(n,\gamma)$ signal hits should have distinctive properties. Figure 3.3 shows the gamma-ray multiplicity and total energy distributions for captures on both nuclides. The $p(n,\gamma)$ reaction emits a single monoenergetic 2.22 MeV gamma-ray, whereas the $\mathrm{Gd}(n,\gamma)$ reaction emits 4 to 8 gamma-rays with their energies totaling 7.98 MeV for captures on ^{157}Gd and 8.54 MeV for captures on ^{155}Gd. Figure 3.4 shows the energy distribution of individual simulated gamma-rays, which are mostly sub-MeV for the $\mathrm{Gd}(n,\gamma)$ reaction. These individual gamma-rays are generated with uniform angular distribution for 4π solid angle.

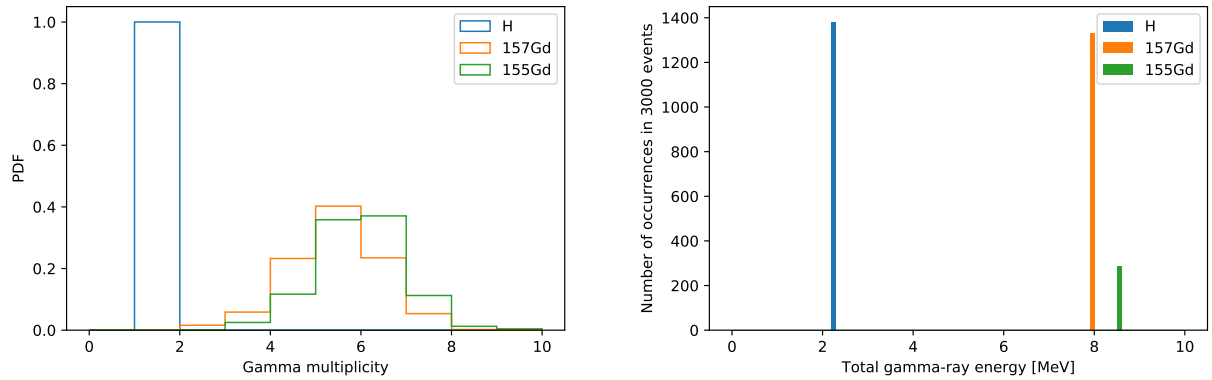

Figure 3.3: The gamma-ray multiplicity (left) and the energy sum of all emitted gamma-rays (right) obtained from simulation with the GCALOR and ANNRI-Gd model. (area-normalized)

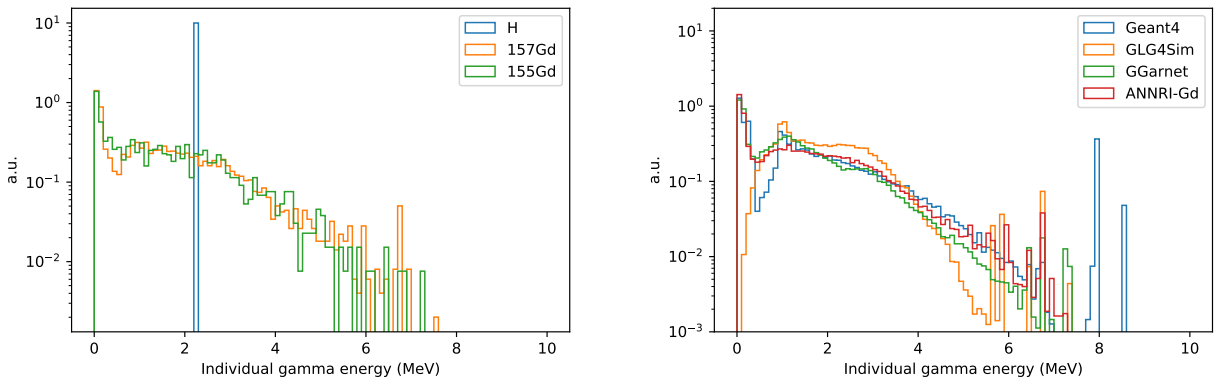

Figure 3.4: The energy distribution of the individual gamma-rays obtained from simulation with the GCALOR and ANNRI-Gd model (left) and the same for $\mathrm{Gd}(n,\gamma)$ reaction with four different physics models available in the simulator, the default Geant4 [26], GLG4Sim [27], GGarnet [24], and ANNRI-Gd [24]. (area-normalized)

Neutrons travel through a random path before they are thermalized and finally captured by a surrounding nucleus. The distances from a neutron's initial vertex to its capture position with its momentum between 60 to 120 MeV/c were obtained from simulation, and Figure 3.5 shows their distribution. The left figure suggests that low-energy neutrons with kinetic energy below 10 MeV are likely to be captured ∼20 cm away from the initial vertex. Clear momentum dependence of the distance can be observed from the right figure. The figures also imply that the capture vertex resolution of any neutrino vertex fitter, which only works on the recoil leptons, should be at least ∼20 cm.

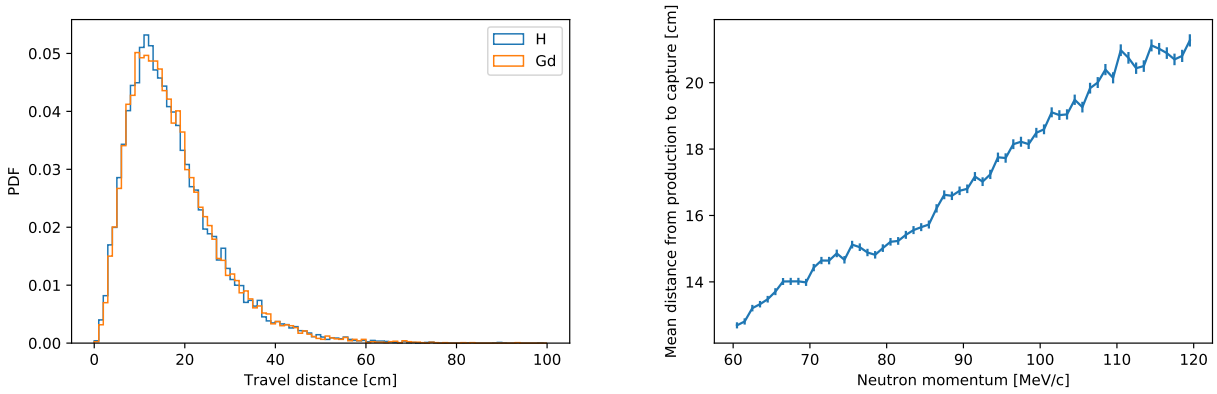

Figure 3.5: The distribution of distance from neutron's initial vertex to the capture vertex (left, area-normalized) and the mean of the same distance by neutron momentum (right) obtained from simulation with the GCALOR and ANNRI-Gd model.

However, what physically hit the PMTs are the Cherenkov photons generated by Compton-scattered electrons, rather than the capture gamma-rays themselves. These gamma-rays should travel another few tens of centimeters before they scatter off an electron. Since the scattered electrons are usually barely over the Cherenkov threshold, they can only radiate instantaneously. Hence, it is safe to assume that all Cherenkov radiation has originated from the electron vertex. Figure 3.6 displays the distribution of the distances from the neutron's initial vertex to vertices of scattered electrons. According to this figure, signal hits should be coming from coordinates 20 to 60 cm (1σ: 48 cm) away from the neutron's production point. This implies that the resolution of the neutrino vertex fitter, if we were to use it to estimate the neutron vertex, would not significantly affect the overall performance of neutron detection as long as the resolution stays within 50 cm.

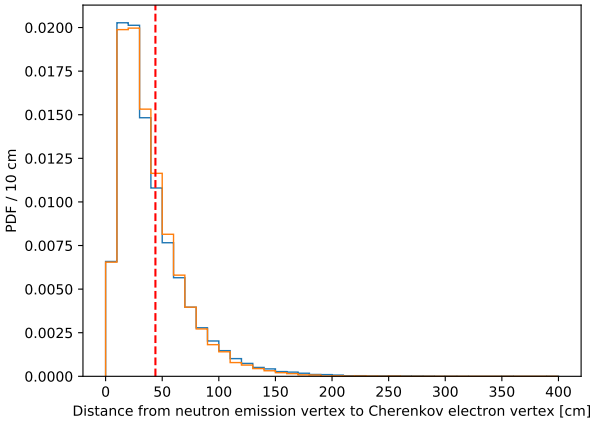

Figure 3.6: The distribution of the distances from neutron's initial vertex to scattered electron vertices obtained from simulation with the GCALOR and ANNRI-Gd model. (area-normalized) The red dotted line is positioned at the 1σ value, which is $\sim$48 cm.

3.2 Stage 1: Hit-cluster search

The first step of the neutron detection algorithm is to pick out neutron signal "candidates" based on their hit counts. However, both signal and dark hits have comparable hit counts in $O(100)$ ns, so we might end up picking up an enormous amount of dark hits as candidates, if we were to use the detector's global time. Therefore for each event, we estimate the photon production time instead, by subtracting from the PMT hit time the time-of-flight(ToF) a photon takes to travel from its creation vertex to the tank wall. The estimated photon production time is also called the ToF-corrected hit time or the residual hit time. With vertex resolution good enough, the signal hits have residual hit time spread of $O(10)$ ns, much smaller than the global hit time spread of $O(100)$ ns. Hence working with the ToF-corrected hit time reduces the number of noise hits, most of which have no positional dependence. If a particular set of hits recorded within $O(10)$ ns of residual hit time has more hits than a pre-defined threshold, then the hits are taken as a neutron signal candidate. This process is illustrated in Figure 3.7.

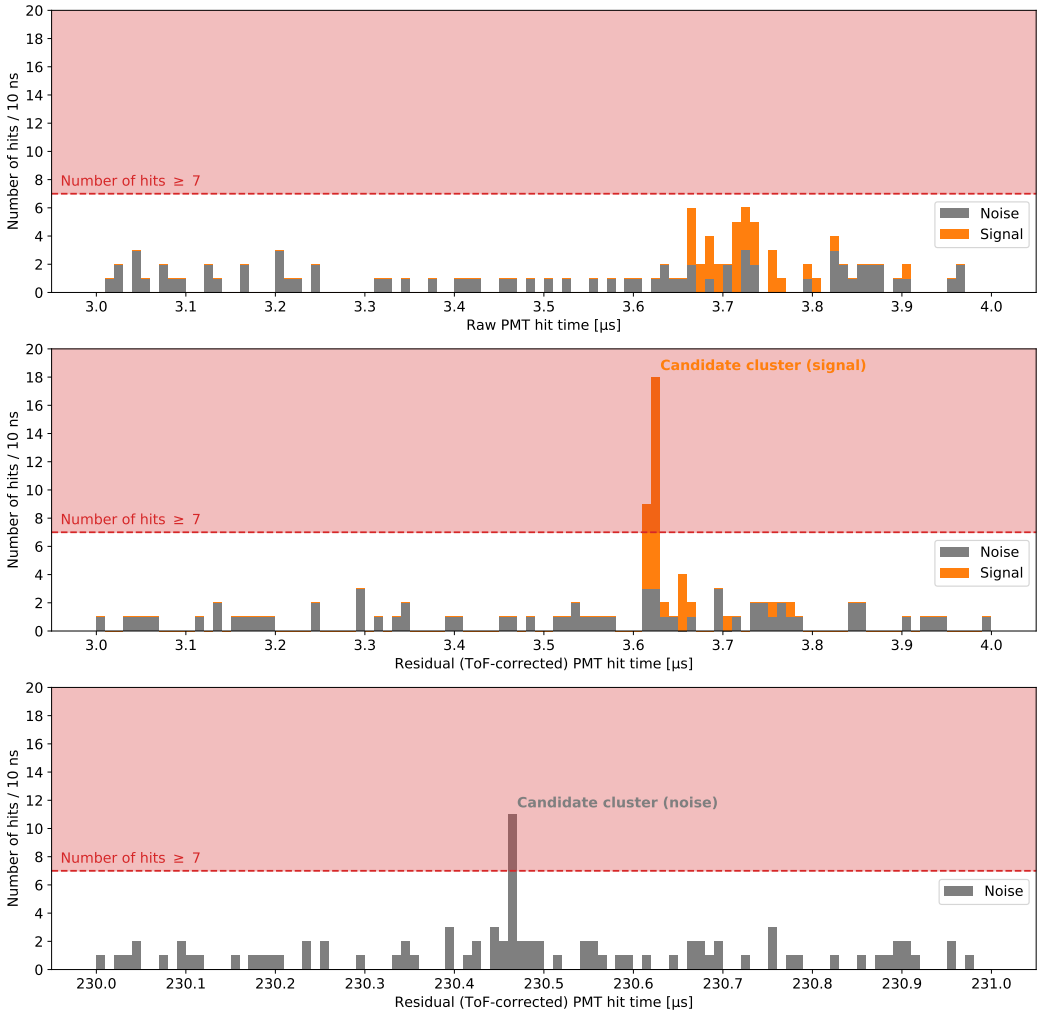

Figure 3.7: Sample distributions of raw PMT hit times of signal (top) and the residual, i.e., ToF-corrected, hit times of signal (center) and noise (bottom). The ToF-corrected hit times show a much sharper peak for signal hits that are generated close to a specific vertex within the tank volume, whereas they don't for noise hits which mostly occur randomly near the tank wall, and thus lack position dependence. For this reason, a sliding time window searches for any cluster of hits more than a pre-defined threshold (e.g., the red dotted line) in the sorted array of ToF-corrected hit times. Any found set of hits are saved as a neutron capture "candidate", and most of the candidates are accidental noise selected as the example shown in the bottom figure. With the search conditions stated in Table 3.3, the signal-to-noise ratio is ∼1:30 as shown in Figure 3.12.

To prevent double-counting a single signal, a parameter TMINPEAKSEP is set as the minimum time difference between any two consecutive candidates. If two neighboring candidates are separated within TMINPEAKSEP, the candidate with more hits replace the other. TMINPEAKSEP should be significantly larger than the resolution (∼20 ns) shown in Figure 3.9.

The performance of the hit-cluster search was optimized and evaluated with the same simulation configuration as in Section 3.1. Since applying a neutrino vertex fitter requires a charged lepton for a primary trigger, for simplicity we smeared the true neutron vertex to simulate the vertex fit, rather than actually applying a dedicated fitter. Each of the true neutron vertex coordinates was smeared by a Breit-Wigner distribution of $\gamma = 7$. Smearing with the given γ value results in vertex resolution of ∼18 cm, which is comparable to that of fiTQun [28], whose 1σ vertex resolution for sub-GeV 1-ring muon neutrino events is ∼18 cm. This is well within the ∼50 cm vertex resolution of Cherenkov-radiating electrons shown in Figure 3.6. The smeared neutron vertices are as illustrated in Figure 3.8.

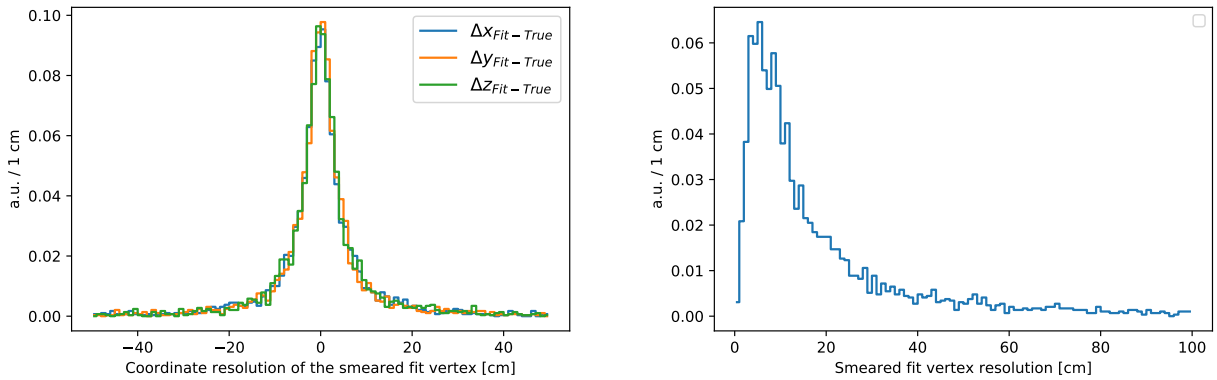

Figure 3.8: The coordinate resolution (left) and the distance resolution (right) of the smeared neutron vertices. (area-normalized) The maximum distance from the smeared vertex to the true vertex was limited to 150 cm.

There are several tunable parameters within this stage. One of the most critical ones that directly affects the cluster search is the time width of the search window that slides through the sorted array of ToF-corrected hit times. Let us call this parameter the "search window width." With a wider width, more signal hits as well as noise hits are likely to be included within the search window. From Figure 3.9, we expect the optimal value to be within $O(10)$ ns, however, it had not been optimized quantitatively ever since the algorithm was designed. So far, the width of 10 ns had been used since the value is optimal for containing electron events, and thus commonly used within the SK collaboration. In this study, the search window width was tuned to 14 ns, which is close to the peak widths shown in Figure 3.9 and shows higher signal-to-noise significance for $p(n, \gamma)$ signals according to Figure 3.10.

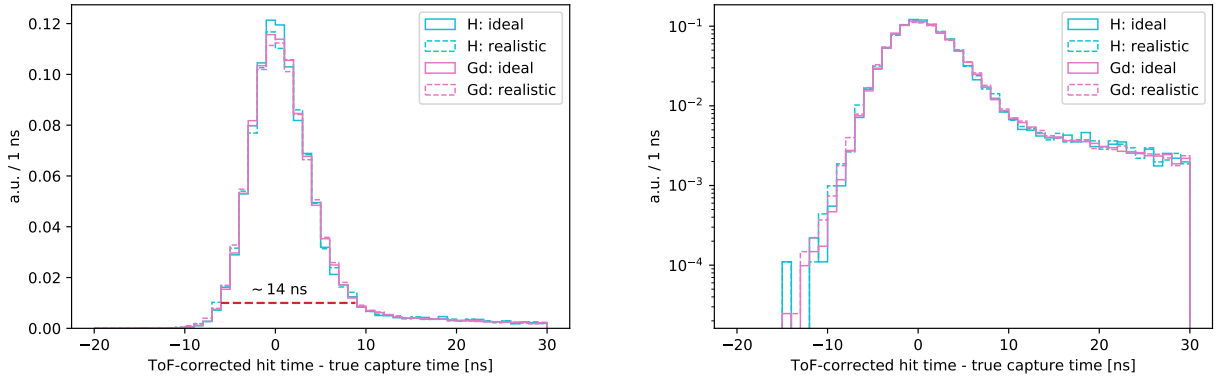

Figure 3.9: The linear-scale (left) and log-scale (right) residual (ToF-corrected) hit time distribution for signal hits. (area-normallized) The solid lines are the results of ideal vertex resolution (fit neutron vertex = true neutron vertex) and the dotted lines are those of realistic resolution (1σ resolution being ∼18 cm). Both ideal and realistic resolutions show almost identical peak widths of ∼14 ns. The robustness to the vertex resolution within 50 cm is as expected by Figure 3.6. The tail following the peak should represent photons traveling longer than the shortest possible path due to reflection on the tank wall and the glass bulbs covering PMTs.

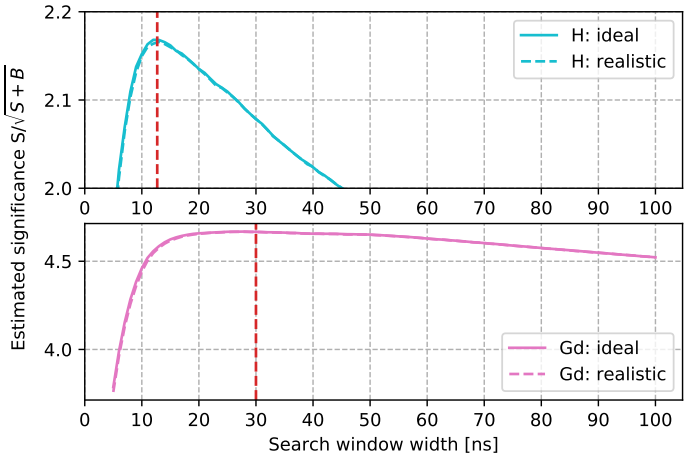

Figure 3.10: The estimated significance $S/\sqrt{S+B}$ versus the search window width, for $p(n,\gamma)$ signals (top) and $\mathrm{Gd}(n,\gamma)$ signals (bottom). The solid line is for ideal and the dotted line is for realistic resolution similar to fiTQun (∼18 cm). The noise hits were assumed to be perfectly uniform with the rate of 0.08 hits/ns, which is a good approximation of the noise hit rate within SK6. The maximum significance was achieved with the search window width of ∼13 ns for $p(n,\gamma)$ reaction and ∼30 ns for $\mathrm{Gd}(n,\gamma)$ reaction. The overall significance was maximized with the width of ∼19 ns.

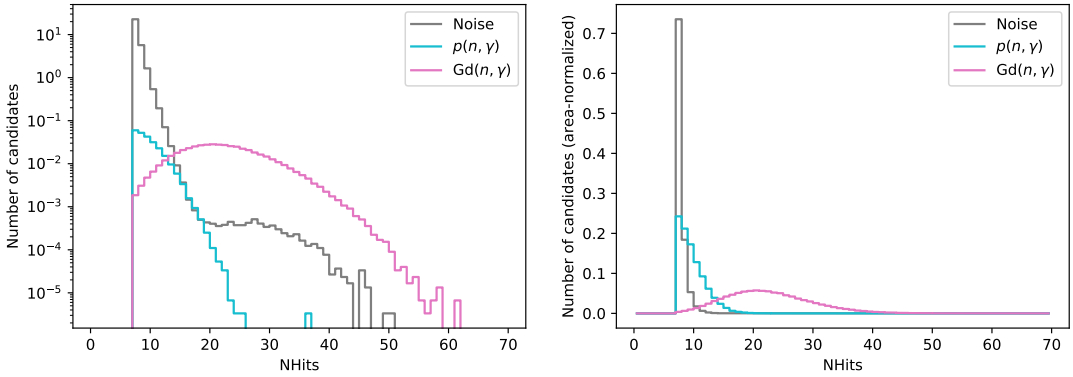

Figure 3.11: The raw (left) and area-normalized (right) N_{Hits} distributions for noise, $p(n,\gamma)$, and Gd(n,γ) candidates.

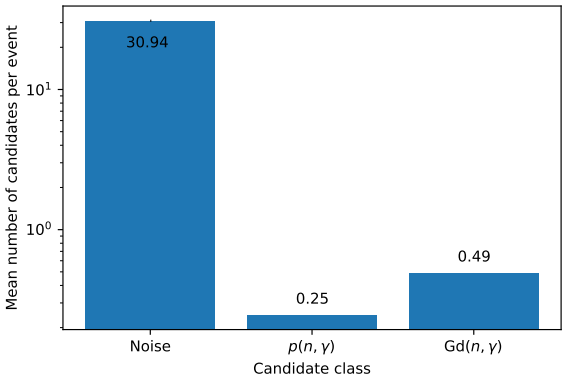

Figure 3.12: Mean number of candidate class per event.

The second parameter of importance is the number-of-hits (N_{Hits}) threshold which should be correlated with the search window width. The N_{Hits} distributions for the three candidate types are shown in Figure 3.11. Determining the threshold is again a compromise between signal purity and detection efficiency. The threshold that has been used so far within SK is 7. With the search window width fixed at 14 ns, three threshold values, 5, 6, and 7 were tested in hopes of getting higher efficiency, and the summary of the test results is shown in Table 3.2. Lower thresholds show dramatically higher selection efficiency for Stage 1, especially for $p(n,\gamma)$ captures. However, the number of noise candidates, which directly translates to the computational load, increases significantly as well. Besides, signal candidates with a too small number of hits are often indistinguishable from noise candidates, and therefore they are likely to be rejected by the MLP that is used to separate signals and noise in the following Stage 2. If most of the signal candidates with a small number of hits were to be rejected in the end, there would be no reason to lower the threshold after all, which would only sacrifice signal purity and increase the computational load exponentially.

To verify the validity of lowering the N_{Hits} threshold, a sample MLP with the same architecture as the one used in Stage 2 (explained in Section 3.3) was made with Keras [29], and was trained with candidates selected with different threshold values. The top three rows in Table 3.2 show the selection results of the threshold values 5, 6, and 7 from a 3,000-event single neutron MC. The selection efficiencies of both Stage 1 and 2 combined listed in Table 3.2 are the ones that give the noise ratio of 2% within the selected candidates. The overall selection efficiency is higher for lower threshold, so we can conclude that lowering the threshold definitely enhances detection efficiency, especially for $p(n,\gamma)$ signals. However, whether it is worth computing $\sim$15 times longer amount of time to get a few percent increased amount of signals boils down to one's personal preference. Also, the enhanced efficiency with lower thresholds may merely be a result of larger input statistics, i.e., the much larger amount of noise candidates taken in one event.

To check the effect that the amount of statistics has on the final selection efficiency, an additional test set of candidates were taken from a 300,000-event single neutron MC with threshold value of 7. The results are listed in the final row of Table 3.2, and they are almost comparable to the

results with threshold 6. Hence, it is evident that the lower selection efficiency that comes with a higher threshold value can be compensated by increasing the quantity of input statistics. In fact, event-wise parallel computing enables us to process 300,000-event MC as fast as 3,000-event MC, as long as we can split the job into 100 pieces and run them in parallel. For this reason, the threshold was kept as 7 in this study. However if the detection efficiency for the $p(n,\gamma)$ channel is crucial as with pure water, one would have to consider lowering the threshold by the expense of the computation time.

		Stage 1 eff. (%)			$N_{\text{Candidates}}$		Stage 1&2 eff. (%)			
No.	N_{Hits} cut	Gd	H	All	Noise	Signal	Thr.	Gd	H	All
1	$N_{\text{Hits}} \geq 5$	99.4	82.9	91.8	1,477,453	2,753	0.767	97.4	26.4	66.0
2	$N_{\text{Hits}} \geq 6$	99.3	71.4	86.4	382,762	2,592	0.740	96.9	20.6	62.2
3	$N_{\text{Hits}} \geq 7$	99.3	58.8	80.6	96,160	2,418	0.425	95.8	17.0	58.7
4	$N_{\text{Hits}} \geq 7$	99.0	57.5	79.3	9,660,836	237,913	0.740	96.7	24.4	62.6

Table 3.2: The summary of the performance test of different N_{Hits} thresholds. All test sets 1-4 share the same MC configuration as explained in Section 3.1 and 3.2. Test sets 1-3 consist of 3,000 neutron MC events each. The Stage 2 selection efficiencies are obtained with Keras [29] using the same MLP architecture as explained in Section 3.3 for reference. The signal likelihood thresholds (Thr.) and the combined selection efficiencies are the ones that give 2% noise ratio within the final selected candidates. Test set 4 with 300,000 neutron MC events is included for comparison with test set 3. All parameters other than the N_{Hits} threshold are as in Table 3.3.

Another important parameter that needs to be tuned is the PMT dead-time. It is to reduce the PMTs' random burst noise which is known to occur by a higher chance to a PMT with a photon hit rather than a PMT without any. This rather peculiar phenomenon was reported quite recently within the SK collaboration [3]. This noise can be reduced by imposing hypothetical dead-time and removing all hits within the dead-time from the selected candidates. The previous studies [3, 4] suggest 3-6 µs as appropriate values. However in this study, the PMT dead-time was neglected and set to 0, as the search window width had been optimized beforehand without considering this parameter. The full optimization is left for future work.

Table 3.3 lists the parameter values used for the evaluation of the algorithm. For evaluation, the algorithm was applied to 300,000 cold (p = 1 keV/c) neutron MC events with random neutron vertex within the detector's fiducial volume. With the parameter values listed in Table 3.3, the signal selection efficiency of Stage 1, the hit-cluster search, was ∼99% for Gd(n,γ) signals, ∼58% for $p(n,\gamma)$ signals, and ∼80% overall, as shown in Table 3.2.

No.	Parameter	Description	Unit	Value
1	TWIDTH	Search window width for hit-clusters	ns	14
2	NHITSTH	Lower threshold for N_{Hits} within 14 ns	-	7
3	NHITSMX	Upper threshold for N_{Hits} within 14 ns	-	70
4	N200MX	Upper threshold for N_{Hits} within 200 ns	ns	200
5	T0TH	Lower threshold for residual hit time	µs	1
6	T0MX	Upper threshold for residual hit time	µs	535
7	TMINPEAKSEP	Minimum time difference between candidates	ns	60
8	PVXRES	γ in Breit-Wigner vertex smearing	cm	7
9	TRBNWIDTH	PMT dead-time	µs	0

Table 3.3: The list of parameter values used for Stage 1 (N_{Hits}-based candidate search) of the neutron detection algorithm. For reference, the primary particle generation time is 1 µs in the global simulation time frame, and the time range of each data event is [-5, -535] µs. The residual hit time range of [1, 535] µs corresponds to the full time range following neutron emission.

3.3 Stage 2: Binary classification with MLP

The second step is to extract features from the selected candidates and statistically find each candidate's signal likelihood based on its features. If the candidate's signal likelihood is greater than the pre-defined threshold, we say that the candidate is "tagged." As for the multivariate analysis framework, this study used the Multilayer Perceptron (MLP) method, commonly known as the "artificial neural network," which is also currently utilized within the SK experiment to detect neutrons from atmospheric and beam neutrino events. If the user inputs distinguishing features between signal and noise to an MLP, then following the pre-defined algorithm (in this study, backpropagation), the network will optimize itself to output the prediction that gives the highest efficiency or the least loss. This process is called supervised learning. The working principles of the MLP method can be found in Ref. [30].

The Neut-Fit algorithm [1] was used to estimate the origin vertex of signal photons. For each candidate, the algorithm searches for a vertex that minimizes the variance of the ToF-corrected hit times by looping over a fixed number of grid points that evolve increasingly finer after each loop. Specifically for a $p(n,\gamma)$ signal, this algorithm should give nearly ideal electron vertex resolution in theory, if the candidate does not include any noise hit.[2] For this reason, past studies [1, 3, 4] on pure water neutron tagging have utilized Neut-Fit vertices as well as neutron fit vertices in ToF correction. However for $\mathrm{Gd}(n,\gamma)$ signals, the algorithm is not expected to work as well, since the Gd capture signals mostly originate from multiple electron vertices. (refer to Figure 3.2 or 3.3) Therefore, the number of grid points per each coordinate axis was reduced by 80 % (the initial grid width was changed from 100 cm to 500 cm), and the target grid width was changed from 0.5 cm to 20 cm. This change has reduced the computation time by the factor of $O(10^{-2})$ without altering the overall detection performance. The 1σ vertex resolution of Neut-fit for 2.2 MeV gamma-ray was $\sim$270 cm for both before and after the change.

[2] In reality, most candidates have a couple of noise hits as in the center plot of Figure 3.7. The Neut-Fit algorithm is highly sensitive to noise hits, and the vertex resolution is in general much worse ($O(100)$ cm) than that of neutrino vertex fitters ($O(10)$ cm). Nonetheless, Neut-fit is currently the only option available for capture vertex estimation of $p(n,\gamma)$ candidates, as the target N_{Hits} of low energy neutrino vertex fitter is much larger ($\sim$60 Hits for $\sim$10 MeV ν_e events) than typical N_{Hits} of $p(n,\gamma)$ candidates. For $\mathrm{Gd}(n,\gamma)$ candidates, the viability of applying the likelihood-based low energy neutrino vertex fitter BONSAI [31] has been demonstrated in a past fake-data study with 0.1 wt.% Gd concentration [2].

3.3.1 Features (input variables to MLP)

16 features are selected based on the past studies [1, 3, 4], and are extracted from each candidate to be used as inputs to the MLP. Distributions are shown in Figure 3.13, and their correlation matrices are as illustrated in Figure 3.14. The candidates are classified into noise, $p(n,\gamma)$, and Gd(n,γ) candidates by comparing the reconstructed capture time (ReconCT) and the true neutron capture time within a simulated event. The reconstructed capture time of a candidate is defined as the average of the maximum and minimum ToF-corrected hit times of the candidate. Any candidate whose ReconCT is within 50 ns from the true neutron capture time, or the capture gamma-ray production time in the simulation time frame, is taken as signal candidates.[3] The following is the description and categorization of the features according to their definitions:

- N_{Hits}-related:
  - **NHits**: The number of hits within the residual search window width (14 ns).
    NHits should be one of the most strongly separating features. Most of the Gd(n,γ) signals and some of the $p(n,\gamma)$ signals could be separated by a simple cut on *NHits*, for example, $NHits > 15$. *NHits* for noise candidates decreases exponentially.
  - **N200**: The number of hits within (-100, +100) ns window centered at ReconCT.
    N200 has separation power on candidates that are selected due to accidental increase of noise hits (radioactivity, spallation, etc.) within proximity. *N200* for noise candidates show much weaker correlation with *NHits* than for signal candidates.
- Timing-related:
  - **TRMS**: Standard deviation of residual hit times (within 14 ns).
    Noise hits are mostly random in time, and thus they generally have a larger *TRMS* than signal hits. Gd(n,γ) candidates show a sharper distribution, since they have much larger signal-to-noise ratio than $p(n,\gamma)$ candidates.

[3] This strategy that has been used so far within SK is convenient, however, is a source of error as noise candidates coincident with a neutron capture can be classified as signals. It should better be replaced with a hit-based alternative in the future.

- Vertex-related:

  - **prompt_nfit**: Distance from the (smeared) neutron fit vertex to the Neut-Fit vertex. Neut-fit vertices of signal candidates should be mostly within 500 cm distance from the neutron vertex, considering the resolution of Neut-fit (1σ: 270 cm for 2.2 MeV gamma-ray). Candidates with smaller *prompt_nfit* are more likely to be signals, and those with very large *prompt_nfit* ($>$ 1,000 cm) are most likely to be noise.

  - **DWall**: (Shortest path) distance from the neutron fit vertex to the tank wall.
    A neutron fit vertex is technically a vertex that is used for ToF subtraction. *DWall* itself has no separation power whatsoever, as a neutrino vertex fitter, unlike Neut-Fit, gives out only one fixed vertex per event. However, *DWall* combined with other vertex-related features should provide a better picture of the neutron vertex to the MLP. For example, if a candidate has a small *DWall* and a relatively large *DWallMeanDir* (explained below), the candidate is more likely to be a noise since the photons that have hit the detector should have traveled further against attenuation than *DWall*. Including *DWall* as a feature has indeed increased the overall detection efficiency by $\sim$1% (abs).

  - **DWall_n**: Distance from the Neut-fit vertex to the tank wall.
    DWall_n has high separation power for noise candidates, many of which have Neut-Fit vertices on the tank wall (*DWall_n* = 0). *DWall_n* for signal candidates shows stronger correlation with *DWall* than for noise candidates. Unfortunately, *DWall_n* cannot replace *DWall*, since the resolution of Neut-fit is much worse ($O(100)$ cm) than that of dedicated lepton vertex fitters ($O(10)$ cm).

  - **DWallMeanDir**: *DWall* in the averaged hit direction.
    DWallMeanDir should be smaller for signal candidates whose PMT-hitting photons have to travel against attenuation. Many noise candidates, however, are a set of spontaneous dark hits coming from the PMTs themselves, and thus they tend to have a larger *DWallMeanDir*. *DWallMeanDir* is negatively correlated with PMT acceptance (refer to [1, 4] for details), or the probability of PMTs to be hit.

– **ThetaMeanDir**: Mean of the angles made by a vector from the neutron fit vertex to each hit PMT and a unit vector in the averaged hit direction.

ThetaMeanDir of $p(n,\gamma)$ candidates should have its peak close to 42°, which is the Cherenkov angle of water. *ThetaMeanDir* for $\mathrm{Gd}(n,\gamma)$ candidates does not share the same physical meaning due to the gamma-ray multiplicity of $\mathrm{Gd}(n,\gamma)$ reaction. Noise hits are often clustered locally, and thus noise candidates have a tail in the lower end of the distribution. However, the 42° peak of noise candidates had not been identified in the past study [1], and further investigation is needed.

- Angularity-related:

– **AngleMean**, **AngleStdev**, **AngleSkew**: Mean, sample standard deviation, and skewness of the opening angles of all possible 3-hit combinations.

Any 3-hit combination has an opening angle, and there exist $\binom{N_{\mathrm{Hits}}}{3}$ possible 3-hit combinations for a candidate with N_{Hits} hits. The features *AngleMean*, *AngleStdev*, and *AngleSkew* are all statistics of the opening angle distributions of a candidate. The introduction of these features is inspired by one of the past studies [4] that has introduced *Cherenkov-likelihood* of PMT hits. Its separability is based on the discrepancy between the opening angle distributions of signal and noise candidates. Noise hits are more likely to be either clustered locally or distributed randomly, which makes tails at ends. *AngleMean* shows very strong correlation with *ThetaMeanDir*.

– **Beta(l)**: Angular isotropy parameters of hits.

The *Beta(l)* parameter is defined as

$$\beta_l = \frac{2}{N_{\mathrm{Hits}}(N_{\mathrm{Hits}}-1)} \sum_{\substack{i,j \\ i\neq j}} P_l(\cos\theta_{ij}) \tag{3.1}$$

where P_l is the Legendre polynomial of degree l ($1 \leq l \leq 5$), and θ_{ij} is the angle between two vectors from the neutron fit vertex to the i-th and j-th hit PMTs. In general, lower values of the *Beta(l)* parameters indicate greater angular isotropy of hits. These parameters up to scaling are the estimated sum of the spherical harmon-

ics expansion coefficients, which must be rotationally invariant. They characterize the angular distribution of the PMT hits, and have shown separation power between signal and non-signal hits in the SNO experiment [32]. For that reason, they have been adopted to neutron detection in the SK experiment by the past studies [2, 4]. These parameters show distinct distributions between signal and noise candidates, however, it seems like the number of signal-like noise candidates has increased compared to the previous work [4].

The correlations that *Beta(l)* parameters have with other features are interesting. *Beta1* has very strong correlation with *ThetaMeanDir*, since *Beta1* is equivalent to a cosine of *ThetaMeanDir*. All *Beta(l)* parameters are mutually correlated for noise candidates, but not as much for signal candidates. *Beta(l)* parameters are also strongly correlated with the opening angle statistics, especially with *AngleMean* and *AngleStdev*, and moderately correlated with *prompt_nfit*. The correlation is smaller for signal candidates. As in the SNO experiment [32], a linear combination of a selection of *Beta(l)*, such as $\beta_{14} := \beta_1 + 4\beta_4$, might be enough for an input.

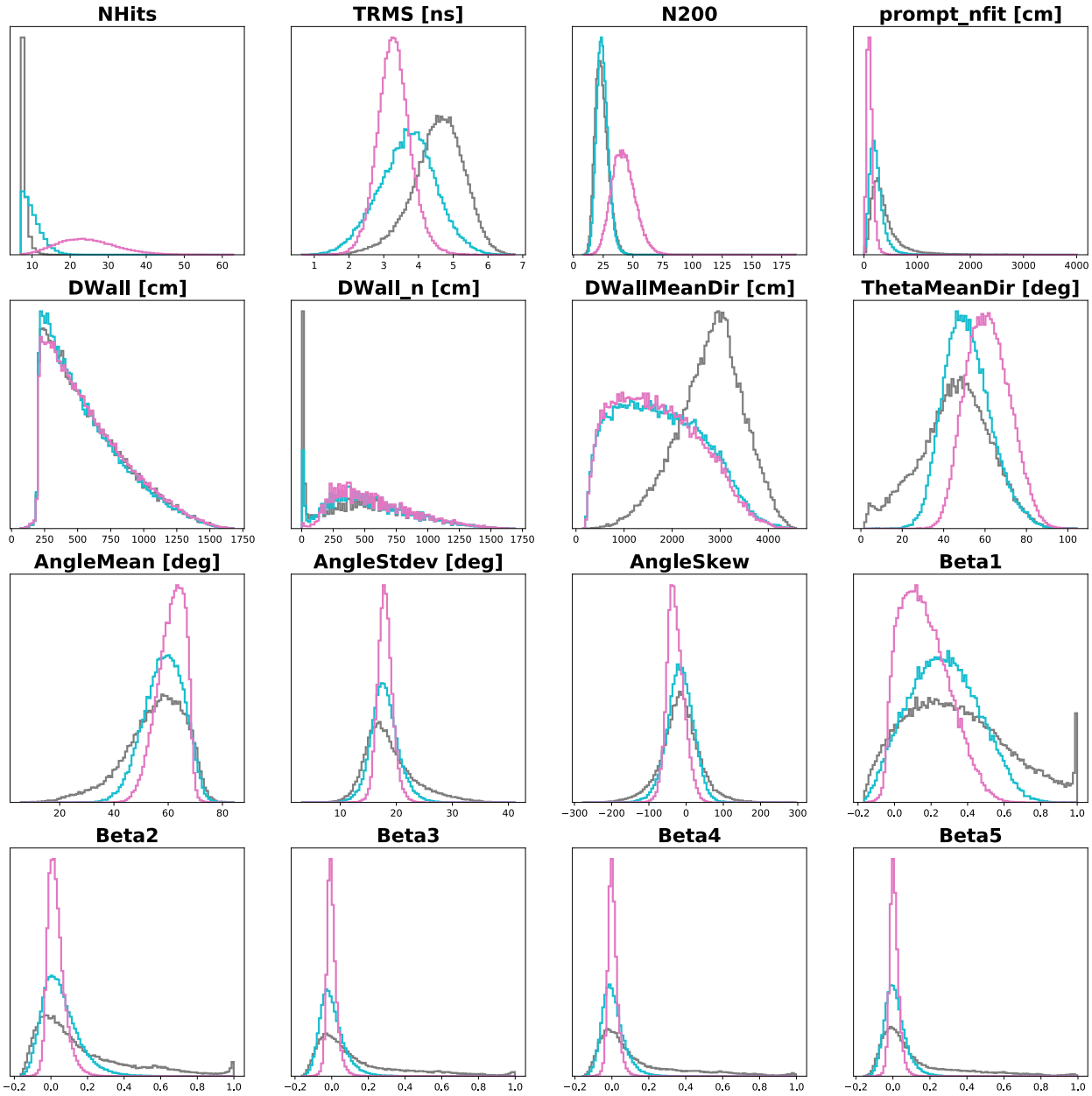

Figure 3.13: The MLP input feature distributions of noise candidates (gray), true Gd(n,γ) candidates (pink), and true $p(n,\gamma)$ candidates (cyan) (area-normalized). 5,000 candidates each are randomly sampled candidates a cold (p =1 keV/c) neutron MC with the MC configuration explained in Section 3.1.

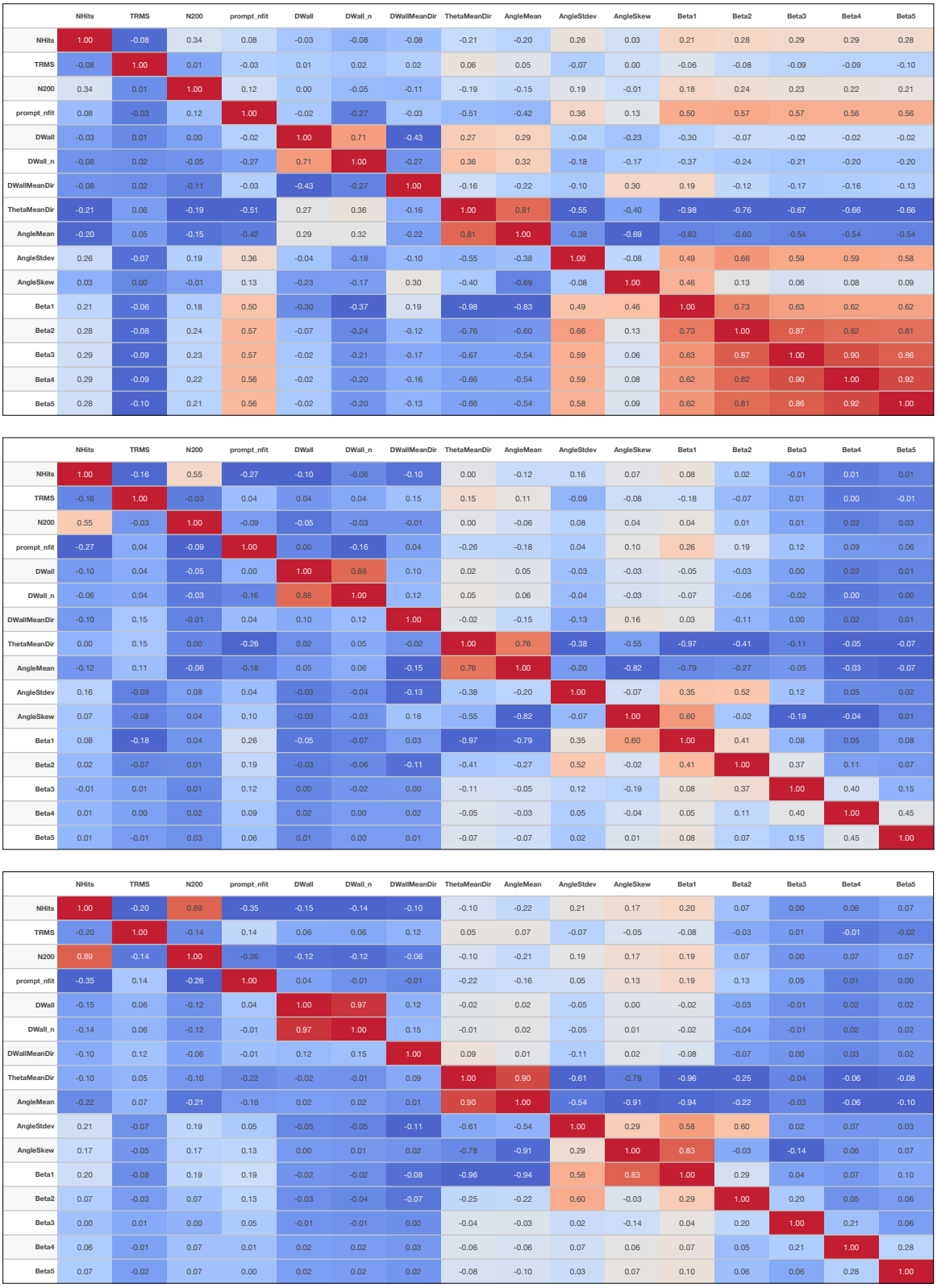

Figure 3.14: Correlation matrices for noise (top), $p(n,\gamma)$ (center), and $\mathrm{Gd}(n,\gamma)$ candidates (bottom).

3.3.2 Training the MLP

Modeling and executing the binary classification with MLP was done with TMVA [33] (Toolkit for Multivariate Data Analysis with ROOT) v4.2.0 [34]. This is a package developed by a group of physicists during the early 2000s. It is very convenient if the data is in ROOT format. The version 4.2.0 has been the latest standalone version that is available since the program was integrated into ROOT in 2013. Although the convergence is quite slower than the latest optimizers such as Adam [35], it shows similar performance as Keras [29] or the latest TMVA that is maintained by ROOT. The `MVA::MLP` class of TMVA was used to model the MLP. The options used are specified in Table 3.4. The hyperparameters have been tuned heuristically rather than systematically.

The binary cross entropy (BCE) is used as the loss function. The BCE is defined as

$$\mathrm{BCE} = -\frac{1}{N}\sum_{i=1}^{N}\left(y_i^{\mathrm{true}}\log p(y_i) + \left(1-y_i^{\mathrm{true}}\right)\log\left(1-p(y_i)\right)\right) \tag{3.2}$$

where N is the number of candidates, y_i^{true} is the true class (label), and $p(y_i)$ is the output node value, i.e., the signal likelihood of the i-th candidate. The output signal likelihood $p(y_i)$ must be restricted within the range [0, 1], as we use the sigmoid $f(x) = 1/(1+e^{-x}) \in [0,1]$ as the activation function of all nodes. The change of loss versus epochs is shown in Figure 3.15. The convergence within 1% loss variance was achieved after ∼200 epochs with the learning and decay rates specified in Table 3.4.

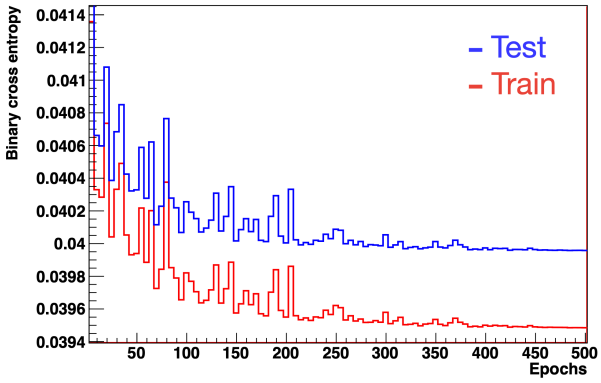

Figure 3.15: BCE versus epochs for test and train data sets.

Option	Used values
Weighting	None
Variable transformation	Normalization
Activation function	Sigmoid
Epochs	500
Architecture	16:17:15:1
Loss function	Binary cross entropy
Optimizer	Backpropagation
Learning rate	0.02
Decay rate	0.01
Train/test split	50:50 (randomly sampled)
UseRegulator	True

Table 3.4: TMVA's MLP options used for training.

The importance of the features is illustrated in Figure 3.16. The importance of the i-th input variable I_i in TMVA [34] is defined as the sum of the squared weights between the variable and the nodes in the first hidden layer:

$$I_i = \bar{x}_i^2 \sum_{j}^{n_{\text{nodes}}^{(1)}} \left(\omega_{ij}^{(1)}\right)^2 \tag{3.3}$$

where $\bar{x}_i$ is the sample mean of the i-th input variable, $n_{\text{nodes}}^{(1)}$ is the number of nodes in the first hidden layer, and $\omega_{ij}^{(1)}$ is the weight of the connection between the i-th input variable and the j-th node in the first hidden layer. The opening angle statistics *AngleMean*, *AngleStdev*, and *AngleSkew* which were introduced to replace the Cherenkov-likelihood used in the past study [4] showed the weakest importance.

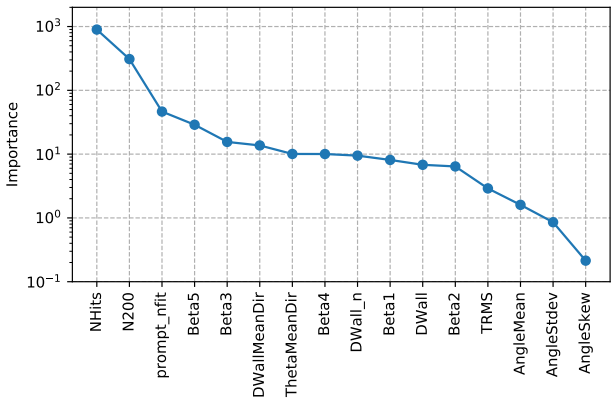

Figure 3.16: Feature importance.

3.4 Evaluation

Evaluation of the combined (Stage 1&2) neutron detection algorithm was estimated using single cold (p_n = 1 keV/c) neutron MC (without any other particle generation). The test data set was made by randomly sampling 50% of signal and noise candidates each from 300,000 MC events. The other half is used for training MLP, which is explained in Subsection 3.3.2. The numbers of total noise candidates and total signal candidates in the test data set were 4,748,992 and 116,677, respectively. The neutron fit vertex, i.e., the estimated neutron emission vertex was smeared from a true neutron vertex using the smearing condition explained in Section 3.2. Noise hits were taken from randomly sampled events taken at the end of the SK6 commissioning phase (Run 85200 - 85245). The performance of the algorithm is summarized in Figure 3.17.

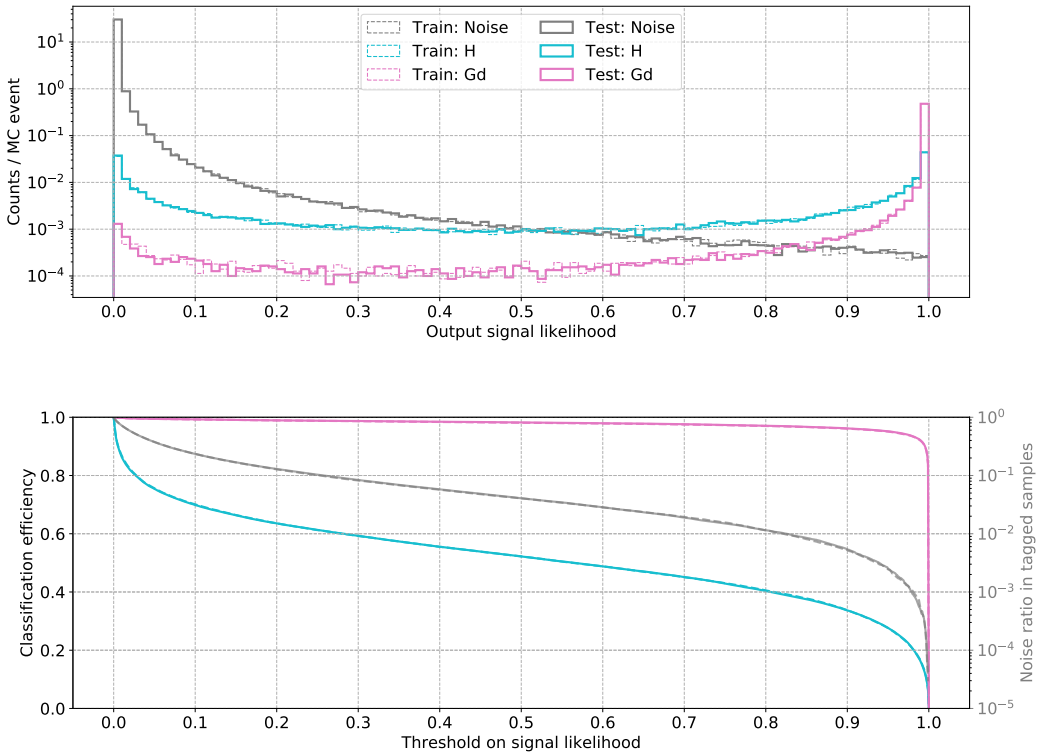

Figure 3.17: The signal likelihood distributions (top) and the MLP performance (bottom).

The results are as expected; most noise candidates have signal likelihood close to 0, while signal candidates have larger signal likelihood in general. The $p(n,\gamma)$ candidates show smaller signal likelihood than the Gd(n,γ) candidates. The bottom figure represents the performance of the trained MLP according to the threshold values set on signal likelihoods. For example, if

we tag candidates with signal likelihood larger than 0.5, we reject about a half of the $p(n,\gamma)$ candidates selected in Stage 1, while almost all $\mathrm{Gd}(n,\gamma)$ candidates from Stage 1 are tagged. The noise ratio within the tagged candidates, i.e., candidates with signal likelihood larger than the threshold, should be close to 4 %.

To evaluate the performance of Stage 1 and 2 of the detection algorithm, we define the neutron capture detection efficiency $\epsilon_{(n,\gamma)}$ as:

$$\epsilon_{(n,\gamma)} = \frac{(\#\text{ of true tagged neutron captures})}{(\#\text{ of true neutron captures})} \tag{3.4}$$

The capture detection efficiency $\epsilon_{(n,\gamma)}$ in principle is different from the neutron detection efficiency ϵ_n, whose denominator should be all neutrons including those that are not captured to produce gamma-rays. Since the fraction of such uncaptured neutrons is very low (less than 2 % according to the models used in this study), $\epsilon_{(n,\gamma)}$ is essentially ϵ_n. All efficiencies on MC data set shown in this chapter are $\epsilon_{(n,\gamma)}$ values.

The summary of the trained MLP, for the signal likelihood threshold of 0.7, is given in Table 3.5. The two rows represent different ReconCT time range used for the signal search. Of course it is better to have a wider search time range, but in actual neutron data the first few µs are often contaminated with triggering light coming from recoil leptons or scintillation. Hence, the neutron search time range of [1, 535] µs is practically applicable to MC events only.

The overall neutron detection efficiency of the combined detection algorithm was estimated to be ∼60% (with noise ratio r_{Noise} ∼2 %) for 0.0110 wt.% Gd concentration.

	Stage 1 eff. (%)			Stage 2 eff. (%)			Combined (%)			
Time range	Gd	H	All	Gd	H	All	Gd	H	All	r_{Noise}
[1, 535] µs	99.0	57.6	79.4	98.0	45.0	78.8	95.6	25.9	62.6	2.01
[4, 535] µs	95.3	56.8	77.0	96.6	44.9	78.6	92.1	25.5	60.5	2.06

Table 3.5: Summary of the capture selection efficiencies $\epsilon_{(n,\gamma)}$ of the neutron detection algorithm used in this study. r_{Noise} indicates the noise ratio within the tagged candidates.

Chapter 4

Testing with a neutron source

The neutron detection efficiency of a detector should be a convolution between the detection algorithm's performance and the detector's physical capability.[1] In the performance evaluation explained in the previous chapter, we have replaced the former with the semi-realistic simulation equipped with recently developed physics models and simulation parameters tuned to the pure water phase. We have to demonstrate that it actually reproduces the detector's response.

A traditional approach to this has been putting a point neutron source inside the tank and compare the detector's response between the actual data and its simulation. We have followed this approach and recorded data since the beginning of the Gd phase. Then, the neutron detection algorithm was applied to both data and MC to compare the detection efficiencies. The neutron calibration campaign is still ongoing.

The following subsections will explain the details of the neutron source data and its simulation, compare various distributions of the two, and discuss the sources of systematic uncertainties.

[1] Apart from the simulation parameters that are irrelevant with Gd-loading, the neutron capture ratio on Gd and the optical parameters of the Gd-loaded water should be ideally the ones that characterize the detector. The former is correlated with the capture cross sections, and both are correlated with the Gd concentration. Tuning these parameters is important, however, is beyond the scope of this study.

4.1 Neutron source data

The source we have employed is the so-called AmBe (Americium-Beryllium) neutron source. It is one of the alpha neutron sources where decay alpha particles from one element (e.g., ^{241}Am) are bombarded onto the other element (e.g., ^{9}Be) to produce neutrons. The design of this source is very simple; it is typically made by encapsulating a mixture of AmO_2 and Be powders in a thin stainless steel container. Since the alpha particles can only travel a few dozen micrometers within the compound, the source can be very compact in size ($\sim O(1)$ cm), and thus be a good neutron point source for detector calibration. The source was deployed inside the tank using the Automated Source Deployment System [36].

When the source emits a neutron, it is known to simultaneously emit a 4.4 MeV gamma-ray, also called the "prompt" gamma-ray, with ∼60% chance [37]. These gamma-rays let us know the exact neutron production time, in the same way a recoil lepton does in the inverse beta decay. The prompt gamma-rays are what make the efficiency measurement possible, and without those, we would never be certain if a neutron was actually emitted or not. In order to take advantage of the prompt gamma-rays, the source was put inside a transparent plastic case with 8 symmetrically positioned Bismuth Germanate ($Bi_4Ge_3O_{12}$, BGO) crystals encompassing the source. The arrangement is shown in Figure 4.1. BGO is an inorganic scintillator commonly used to detect gamma-rays. If a gamma-ray hits one of the BGO crystals and scatters off bound electrons, the crystal will scintillate. If the scintillation is strong enough to trigger the detector, then the detector response within a certain time range will be recorded as one event. The recorded data should have several sources of contamination, and they must be removed with a proper set of cuts before we compare the data with MC simulation.

4.1.1 The source: AmBe + BGO

^{241}Am is an alpha-decaying isotope with half-life of ∼432 years. The intensity of ^{241}Am of our source is 97 µCi, or 3.6 MBq [4, 38], and the neutron emission rate was estimated by multiplying the alpha intensity by the neutron yield per alpha particle. The latter, however,

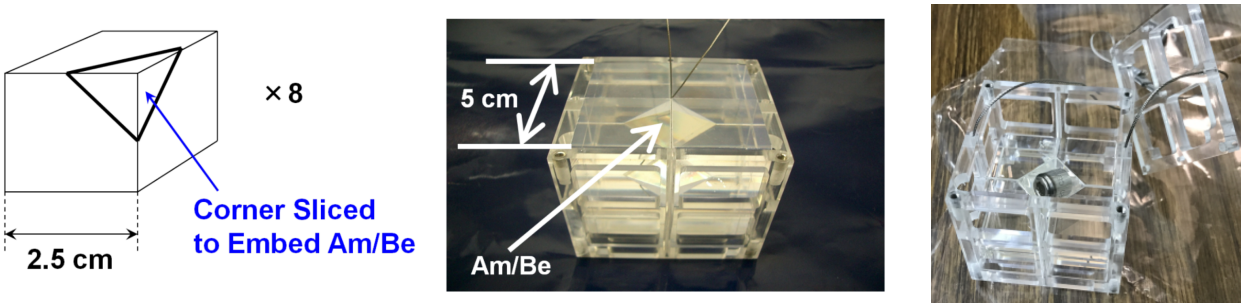

Figure 4.1: The pictures of the deployed source, reprinted from [1, 4]. The AmBe compound is encapsulated in a pellet-sized container, with 8 BGO crystals surrounding it.

is highly dependent on the source design, which unfortunately is unknown either. Hence, the neutron yield per alpha particle was assumed to be 6.0×10^{-5}, based on the other sources [39–41]. The uncertainty was assumed to be 20% according to the reported maximum experimental yield [42]. The neutron emission rate of the source, estimated using the alpha intensity and the assumed neutron yield per alpha particle, is 216 ± 48 neutrons per second. It is larger than the estimate of ∼163 Hz from a previous study [38] by $\sim 1\sigma$. The neutron intensity could be better estimated with a dedicated measurement.

Table 4.1 shows the estimated gamma-correlated and uncorrelated source neutron intensity, based on the recommended prompt gamma-ray emission probability of 0.575 ± 4.8% [37], in comparison with the same estimates on the same source by Watanabe et al. [38].

Neutron type	Estimated intensity	Watanabe et al. [38]
Gamma-correlated	124 ± 28 Bq	87 ± 17 Bq
Uncorrelated	92 ± 21 Bq	76 ± 15 Bq

Table 4.1: The estimated gamma-correlated and uncorrelated neutron intensity of the source. The assumed uncertainty is ∼22% for the estimation in this study, and 20% for Watanabe et al. [38]. The 4.4 MeV gamma-ray intensity should be the same as the correlated neutron intensity.

Figure 4.2 illustrates the measured kinetic energy spectra of the source neutrons. The maximum kinetic energy is ∼12 MeV for uncorrelated neutrons, and ∼7 MeV for gamma-correlated neutrons whose 4.4 MeV energy should be taken away by the prompt gamma-ray.

The details of the neutron emission mechanism is explained in Appendix B.

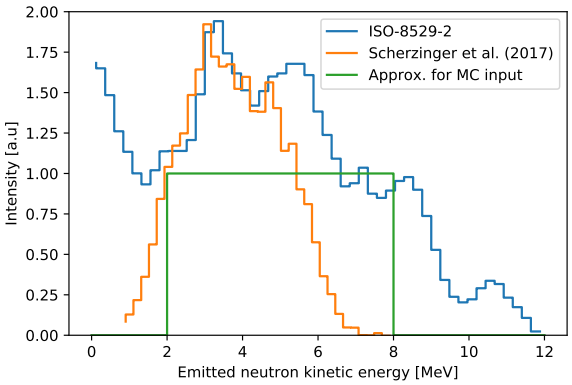

Figure 4.2: Reference AmBe neutron kinetic energy spectra for all neutrons (cited in [40], blue), and for gamma-correlated neutrons ([40], orange). The approximated flat 2-8 MeV input spectrum for correlated neutron simulation is shown in green. The orange and green histograms are area-normalized, and the blue histogram is normalized in a way that the peak value around 3 MeV match the one in the orange histogram.

Some of the relevant properties of BGO are summarized in Table 4.2. We can imagine that a prompt gamma-ray hitting a ∼3-cm-wide BGO crystal would lose most of its energy within the crystal to scintillate enough amount of light to trigger the detector. The amount of photo-electrons deposited in the ID PMTs within the primary trigger time range (within 1.3 µs after trigger) is called QISMSK within SK, and its distribution is shown in Figure 4.3.

Light yield	8,400 photons / MeV
Emission peak	480 nm
Rise time	< 2 ns
Decay time	300 ns
Radiation length	1.1 cm

Table 4.2: Relevant properties of BGO at room temperature. [43]

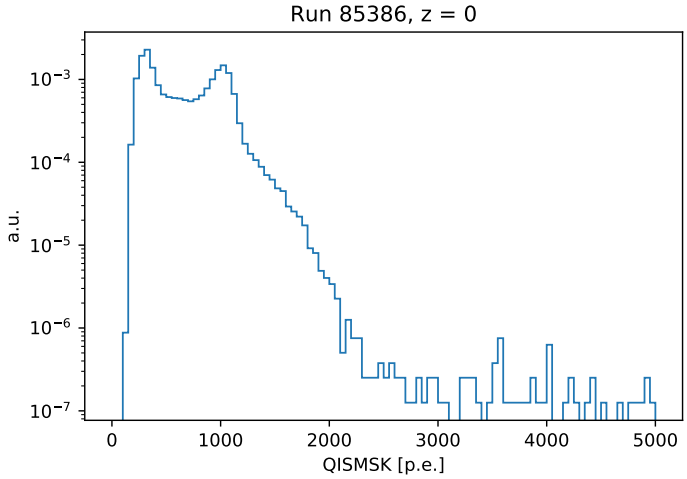

Figure 4.3: The QISMSK distribution of the neutron source data events for Run 85386. Events with QISMSK $>$ 2,000 are mostly triggered by cosmics. Events with QISMSK $\sim$ 1,000 are likely to have been triggered by BGO scintillation.

At the moment, we lack a proper BGO scintillation simulator which enables us to identify and analyze the composition of the QISMSK peaks. We can only infer from the data itself to identify the peaks qualitatively. Figure 4.4 shows the average pulse shape of data events with selected peaks. The pulse shapes of the residual hit time distributions were fitted with a two-component pulse modeling function

$$f(t) = \Theta(t - T_0) \sum_{i \in \{\text{fast,slow}\}} a_i \left[e^{-(t-T_0)/\tau_{d,i}} - \left(\frac{1}{1 + e^{-(t-T_0-5\tau_r)/\tau_r}} - 1 \right) \right] + b \qquad (4.1)$$

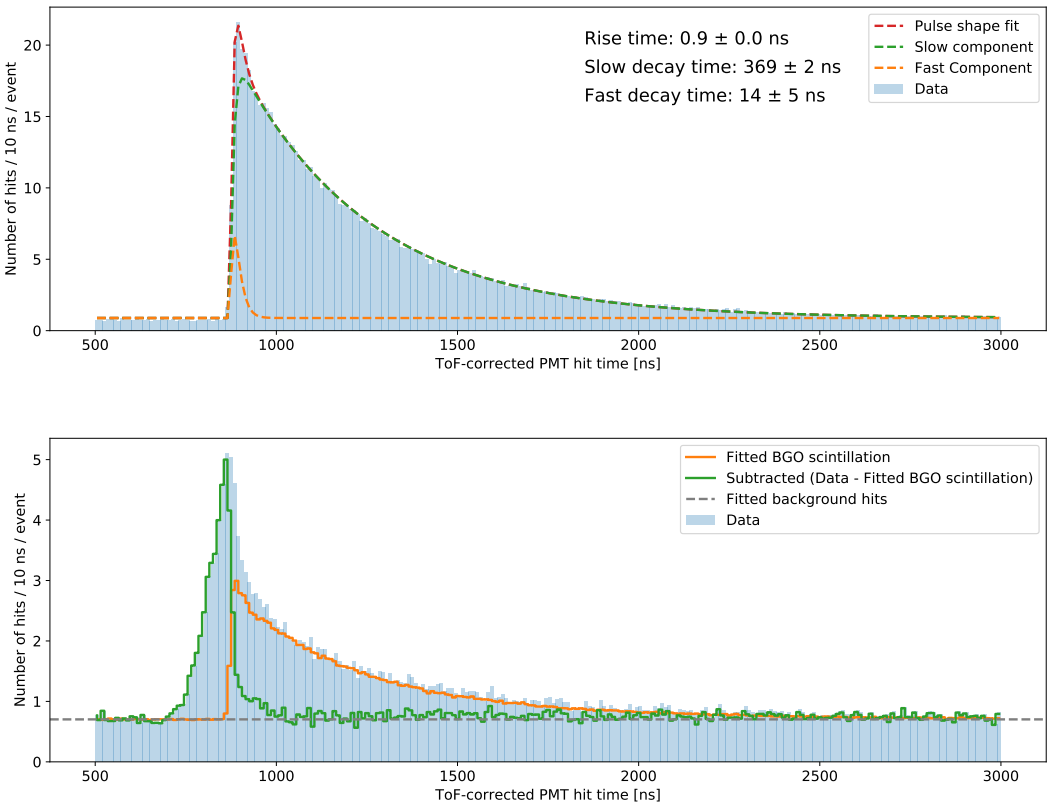

Figure 4.4: The averaged ToF-corrected hit time distributions near the primary trigger time range, for events with 800 < QISMSK < 1250 (top) and events with QISMSK < 400 (bottom). The top histogram is scaled to make the fitted scintillation histogram (orange) in the bottom figure. The scale factor of 0.11 minimizes the variance of the subtracted (green) bin values with reconstructed hit time larger than 1,200 ns (i.e., gives the "flattest" subtracted histogram).

where the parameters are as described in Table 4.3. Each term in the square bracket represents the pulse decay and rise for each of the fast and slow pulse components. Since the typical exponential pulse rise function is replaced with a smoother sigmoid function of the form $1/(1+e^{-t})$, fitting a pulse shape with the function in Equation 4.1 should give a larger fit value for the rise time τ_r than the typical exponential fit.

t	ToF-subtracted hit time [ns]
T_0	Time of first hit on BGO [ns]
Θ	Heaviside step function
a_i	Coefficient for the i-th component
τ_r	Rise time [ns]
$\tau_{d,i}$	Decay time of the i-th component [ns]
b	Baseline number of hits in one bin

Table 4.3: The input t and the fit parameters used in Equation 4.1.

For 800 < QISMSK < 1250, the fitted decay time of ∼370 ns is in reasonable agreement with 300 to 400 ns decay time of BGO with temperature in between 10 and 20°C [44, 45]. Thus, we can conclude that scintillation is the dominant trigger for the events with high QISMSK. However for QISMSK < 400, the same fit with the timing parameters fails to fit the pulse shape properly. Rather, the tail fits quite well with the high QISMSK pulse shape scaled by 0.11, which implies BGO scintillating with either much lower intensity or lower frequency.

The subtracted histogram in the bottom of Figure 4.4 also demonstrates that there may be PMT hits earlier than scintillation, for events with low QISMSK. We can imagine an event scenario where a leaking prompt gamma-ray or a few of the Gd-capture gamma-rays are detected by the PMTs without triggering the detector. If a correlated neutron or the remaining capture gamma-rays hit the BGOs to boost up the earlier hits and eventually trigger the detector, such a scenario can mimic the pulse shape of the low QISMSK events, imprinting a sharp peak with a following signature of scintillation with long decay time. As with the possibility of scintillation due to neutrons, Vincke et al. [46] reports the AmBe neutron's energy deposit within a BGO crystal ∼4 cm in size, as shown in Figure 4.5. A small amount of neutrons mimicking the 4.4-MeV scintillation can be a source of systematic uncertainty, which will be discussed in Subsection 4.4.1.

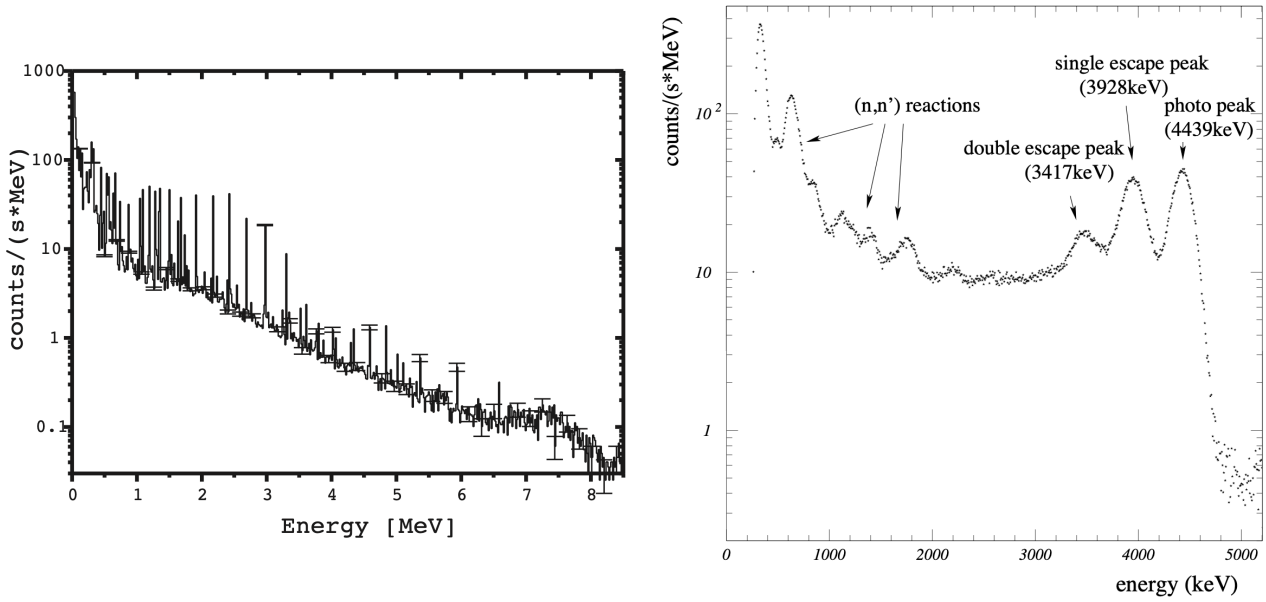

Figure 4.5: The FLUKA-simulated AmBe neutron's energy deposit in BGO (left) and the measured energy deposit of both source neutrons and gamma-rays (right). Reprinted from [47].

4.1.2 Data specification and reduction

The neutron source data has been taken since the beginning of the Gd phase (July 2020), either weekly or bi-weekly with different source positions aligned along the z-axis that passes near the tank center. A dataset for each run has a ∼30-minute record of the detector's response, the most important of which is the hit time and charge information of individual PMTs. Hits more than 60 within a 200 ns time window would trigger the SHE flag of the detector, and the detector response within [-5, 35] µs time window around the trigger would be recorded as one event. The AFT trigger is forced for all SHE triggers. However, for some technical reasons that have not been clarified yet, only ∼50% of the SHE-triggered events accompany a subsequent AFT-recorded event. An AFT-recorded event has an additional 500-µs record of the detector's response following the end of the SHE-triggered event. In other words, about a half of the data events will have ∼535 µs length record of the detector's response following the trigger, while the other half will have only ∼35 µs length of data. In this study, runs taken after the Gd-loading with $z \in \{-12, 0, +12\}$ [m] were selected and analyzed. The specifications of the target runs are summarized in Table 4.4.

	Run	Date	x [m]	y [m]	z [m]	Duration [min]
1	85122	2020-08-05	-3.89	-0.707	-12	33
2	85128	2020-08-05	-3.89	-0.707	0	32
3	85134	2020-08-05	-3.89	-0.707	12	33
4	85149	2020-08-12	-3.89	-0.707	-12	37
5	85155	2020-08-12	-3.89	-0.707	0	31
6	85161	2020-08-12	-3.89	-0.707	12	30
7	85178	2020-08-19	-3.89	-0.707	-12	30
8	85184	2020-08-19	-3.89	-0.707	0	30
9	85189	2020-08-19	-3.89	-0.707	12	30
10	85210	2020-08-26	-3.89	-0.707	-12	31
11	85212	2020-08-26	-3.89	-0.707	0	31
12	85214	2020-08-26	-3.89	-0.707	12	37
13	85228	2020-09-01	-3.89	-0.707	-12	30
14	85230	2020-09-01	-3.89	-0.707	0	31
15	85232	2020-09-01	-3.89	-0.707	12	30
16	85247	2020-09-08	-3.89	-0.707	-12	30
17	85249	2020-09-08	-3.89	-0.707	0	30
18	85251	2020-09-08	-3.89	-0.707	12	30
19	85272	2020-09-15	-3.89	-0.707	-12	31
20	85274	2020-09-15	-3.89	-0.707	0	39
21	85276	2020-09-15	-3.89	-0.707	12	36
22	85299	2020-09-29	-3.89	-0.707	-12	32
23	85301	2020-09-29	-3.89	-0.707	0	30
24	85303	2020-09-29	-3.89	-0.707	12	38
25	85336	2020-10-15	-3.89	-0.707	-12	30
26	85338	2020-10-15	-3.89	-0.707	0	33
27	85340	2020-10-15	-3.89	-0.707	12	34
28	85384	2020-10-27	-3.89	-0.707	-12	32
29	85386	2020-10-27	-3.89	-0.707	0	32
30	85390	2020-10-27	-3.89	-0.707	12	32
31	85435	2020-11-10	-3.89	-0.707	-12	31
32	85437	2020-11-10	-3.89	-0.707	0	30
33	85439	2020-11-10	-3.89	-0.707	12	32
34	85480	2020-12-01	-3.89	-0.707	-12	32
35	85482	2020-12-01	-3.89	-0.707	0	31
36	85484	2020-12-01	-3.89	-0.707	12	30

Table 4.4: Neutron source data runs used in the analysis.

Here, we present the details of the reduction process, specifically for Run 85386 ($z = 0$). It consists of 6 cuts that are supposed to reduce the following possibly contaminated events:

(1) Non-AFT events

Events without AFT flag (i.e., TrgType $\neq 2$) are discarded, which removes about a half of all SHE-triggered events. This cut ensures all selected events have a [-5, 535] µs range.

(2) Cosmic ray events

Cosmic rays can also trigger the SHE flag of the detector. Since cosmic rays are supposed to hit OD PMTs as well as ID PMTs, a cut on the number of OD hits is necessary. The distribution of NHITAC, the number of OD hits within the primary trigger time range, for all SHE-triggered data events and the AmBe neutron MC (explained in Section 4.2) are shown in Figure 4.6. Events with NHITAC > 10 are removed.

(3) Events possibly triggered by neutron capture gamma-rays

Multiple capture gamma-rays from a Gd(n, γ) reaction may trigger the detector and some of them can even cause scintillation. Since we are not supposed to find a neutron signal from events triggered by capture gamma-rays, they must be removed. As can be observed in Figure 4.4, most of the triggering scintillation starts to occur at 860 ns in the reconstructed capture time scale. Thus, events with TrgTagged — the number of tagged candidates with reconstructed capture time < 900 ns — larger than 0 are regarded as possibly triggered by neutron capture gamma-rays and thus removed. Unfortunately, hits induced by a prompt gamma-ray or dim scintillation light are likely to be selected as a tagged candidate, so this cut removes a huge portion of events with moderate QISMSK, as illustrated in Figure 4.8.

(4) Events not likely to have been triggered by 4.4-MeV scintillation

Only the events in the higher QISMSK peak are selected. Events whose QISMSK is not in the range [850, 1200] for $z = 0$ m and [900, 1250] for $z = \pm 12$ m are removed. The QISMSK distributions for three z positions (Run 85384, 85386, 85390) after applying the above cuts are shown in Figure 4.9, along with the QISMSK cut range limits.

(5) Events with a large number of noise hits within the neutron search time range

An event variable MaxNonTrgN1300 was defined to represent the event's maximum number of hits in 1.3 µs within the neutron search time range, which is reconstructed capture time $\in [4, 535]$ µs. Figure 4.10 shows the distributions of MaxNonTrgN1300 for data and MC. Any event with MaxNonTrgN1300 > 160 was regarded as a scintillation-contaminated event, and thus discarded.

(6) Events that may have a neutron mixed in from the preceding trigger

If some two consecutive events are too close in time (i.e., $\Delta t \lesssim O(100)$ µs), a neutron from the earlier event may mix into the subsequent event. To prevent such a set of events, an event variable TDiff [ms] was defined to represent the time difference between two consecutive SHE events. The TDiff distribution of data events are shown in Figure 4.11. Any event with TDiff < 1 ms is removed.

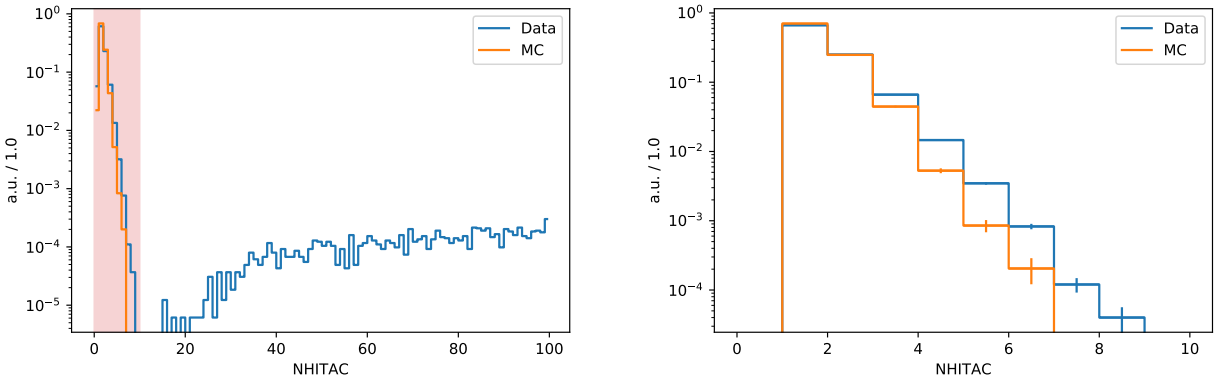

Figure 4.6: The NHITAC distributions for data and MC before Cut 2 (left) and the same distributions after Cut 2 (right). The red rectangle represents the selection range of Cut 2.

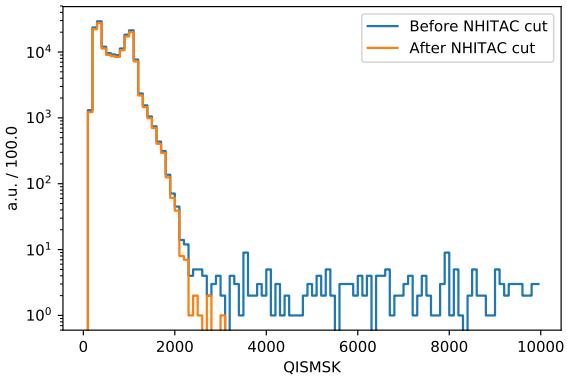

Figure 4.7: The QISMSK distributions before and after Cut 2. Cut 2 apparently removes high QISMSK events triggered by cosmic rays.

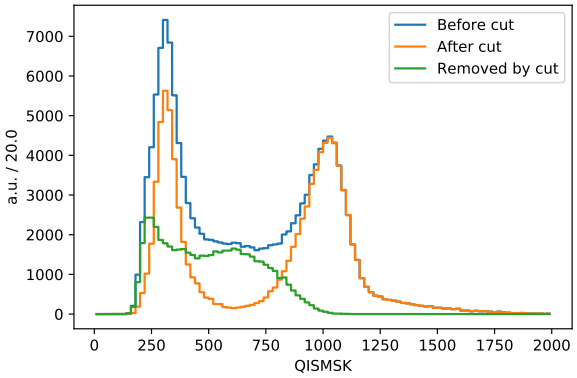

Figure 4.8: The QISMSK distributions of data events before applying Cut 3 (blue), after applying Cut 3 (orange), and removed by Cut 3 (green).

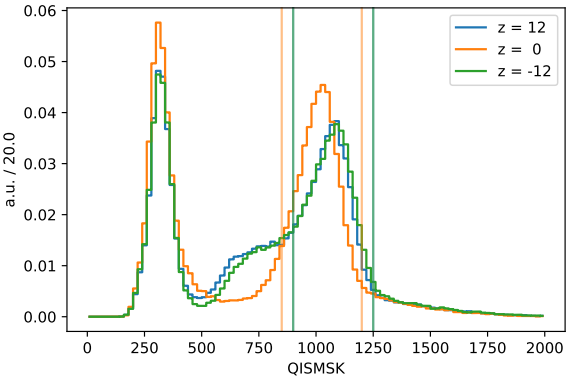

Figure 4.9: The QISMSK distributions for three source z positions. Data for $z = \pm 12$ m show slightly larger QISMSK peak values, as the source is closer to the tank wall. Cut 3 for $z = \pm 12$ m leaves some of the events with moderate QISMSK unlike for $z = 0$ m.

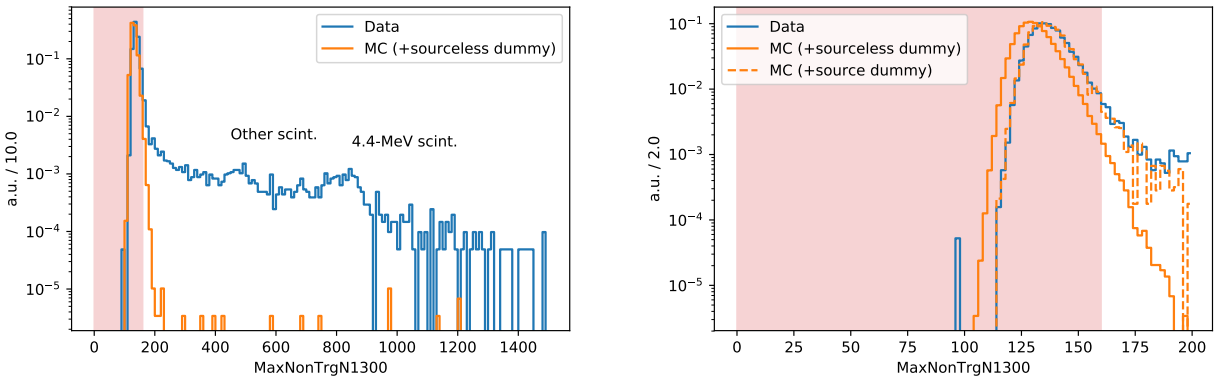

Figure 4.10: The MaxNonTrgN1300 distributions for data and MC (explained in Section 4.2 including source/sourceless dummy) (left) and the same distributions within the range of MaxNonTrgN1300 $\in [0, 200]$ (right). The red rectangles represent the selection range of Cut 5. The long tail in the data distribution should be coming from the source itself, and the two distinct scintillation peaks are observable.

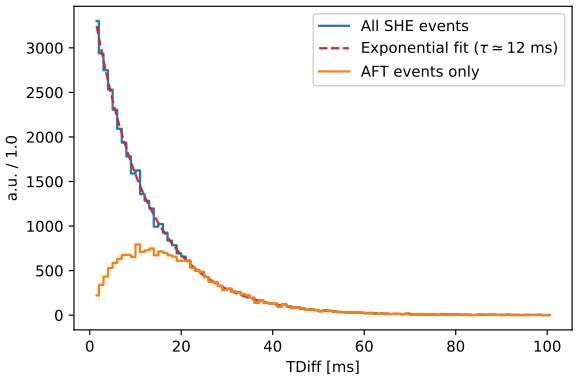

Figure 4.11: The TDiff distributions for all SHE events (i.e., no cut applied) (blue) and for AFT events only (i.e., Cut 1 applied) (orange). The exponential fit to the blue histogram gives the decay time of ∼12 ms. This manifests the Poissonian nature of the SHE triggers, and thus the reciprocal of the decay time directly relates to the trigger rate of ∼83 Hz. For some unknown reason, the AFT flag seems to be omitted more frequently for events close to the previous.

Table 4.5 summarizes the applied event cuts. For Run 85386, the number of total SHE-triggered events was 162,900, and the number of events passing Cuts 1-6 was 22,077 (13.55% pass ratio). Neutron candidates were sought for within the reconstructed capture time (i.e., ReconCT [ns]) range of [4, 535] µs, which corresponds to the data recorded ∼3 µs after the presumed neutron emission. The lower limit of 4 µs is to avoid the scintillation light, as shown in Figure 4.12.

Cut	Removed events	Removed if	Removed ratio
1	Non-AFT	TrgType $\neq 2$	0.54
2	Cosmic ray	NHITAC > 10	0.08
3	Possibly triggered by neutrons	TrgTagged > 0	0.34
4	Non-4.4-MeV scintillation	$\sim(850 <$ QISMSK $< 1200)$	0.51
5	Noisy within neutron search time range	MaxNonTrgN1300 > 160	< 0.01
6	Too close to the previous event	TDiff > 1	0.01

Table 4.5: Summary of the event cuts applied to data events. The removed ratios (among the events passing the previous cut) are obtained for Run 85386.

Cut	Removed candidates	Removed if
1	Too close to scintillation	ReconCT < 4000

Table 4.6: Summary of the candidate cut applied to data events.

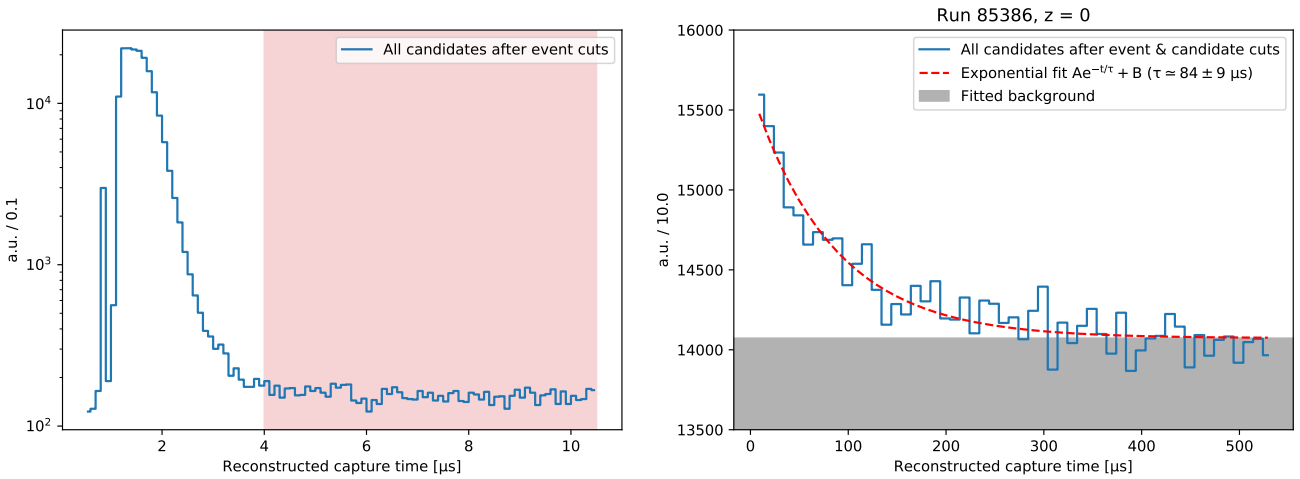

Figure 4.12: ReconCT distributions for all candidates after event cuts (left) and after the final candidate cut (right). The red rectangle in the left figure represents the selection range of ReconCT $>$ 4,000 ns. The exponential fit to the right figure gives the time constant of 84 µs.

Event cuts 2, 5 and Candidate cut 1 were applied to MC dataset as well, as the noise hits for MC are taken from data. The signal likelihood threshold for candidate-tagging was set to 0.7.

4.2 Neutron source simulation

Since it was rather challenging to implement an inorganic scintillator with a complex geometry in the Geant3-based simulator, the simulation of BGO and the trigger system was completely neglected in this study. A single neutron with momentum range [60, 120] MeV/c (close to kinetic energy range [2, 8] MeV) without any prompt gamma-ray or uncorrelated neutrons was simulated with `skdetsim-skgd`. No other source elements were implemented in the simulator. As will be explained later, the lack of BGO and trigger simulation should be the core reason behind the discrepancy between data and MC.

The same physics models — G4NDL neutron cross section library for low energy neutron transport and ANNRI-Gd model for Gd(n, γ) reaction modeling — were used as in generation of MLP training dataset (refer to Section 3.1). The Gd concentration was set to ∼0.0110 wt.%, which is within 1% agreement with the current estimate. The neutron production vertex was fixed at each calibration position, and no vertex smearing was applied. The neutron production time and the trigger time was fixed at t =1,000 ns in the simulated detector's global raw hit time. Since the neutrons in data events are expected to be produced at $t \sim 850$ ns in raw PMT hit time, searching for neutrons in the same time frame for both data and MC would cause some systematic error to the search result. However, this factor is completely neglected in the following analyses, as the neutron's capture time constant ($\sim O(100)$ µs) is much longer than the delay. Less than 0.2 % error is expected with the current Gd concentration.

The noise hits were extracted from the same dummy trigger data as in Section 3.1. One thing to note is that the source itself also randomly generates unwanted noise hits, for example, uncorrelated neutrons and scintillation mixing into the neutron search time range. To compensate for such source-induced noise hits, another set of random trigger data was taken with the source at $z = 0$ m for ∼30 minutes (Run 85388). Let us call the dummy trigger data without the source "sourceless dummy", and the ones with the source inside the tank "source dummy." These two different dummies serve as background measurement. 300,000 single neutron MC events were generated for each z position with sourceless dummy hits attached, and another 30,000 events were generated for $z = 0$ with source dummy hits attached.

4.3 Data and MC comparison

Figures 4.13, 4.14, and 4.15 should give a general idea on the number of events and candidates in data and MC. One thing to note is that there has been a reported increase of noise hits throughout the entire run range used in the analysis. The reason for this is currently under investigation, while one of the suspected is fluorescent bacterial growth within the tank [48]. The current analysis should be affected by this unresolved phenomenon, and it is discussed qualitatively in Section 4.4. Further analysis should be done after the noise level is stabilized.

From this point and on, we assume that each data event is on an equal footing with a neutron MC event. The following subsections will compare distributions of the features, signal likelihood, and reconstructed capture time.

4.3.1 Features

The feature distributions of all candidates from data and MC with sourceless dummy ($z = 0$ only, distributions for other z positions are shown in Appendix C) are shown in Figures 4.16. Although there are more candidates per data events than per MC events as shown in Figure 4.14, the normalized feature distributions are generally in good agreement, proving that modeling data events with a single neutron MC plus noise hits from sourceless dummy data is an effective approach. Still, data events seem to have slightly more signal-like candidates than MC events, as in *Beta(l)* distributions of Figure 4.16. Such tendency is washed out in Figure 4.18, where data events are compared with source dummy MC, suggesting that the afterglow of BGO should have similar angular characteristics as signal hits.

The tagged-candidates distributions in Figures 4.17 and 4.19 also show reasonable agreement between data and MC, except that data events show more $p(n,\gamma)$-like candidates and less $\mathrm{Gd}(n,\gamma)$-like candidates than MC events. Such tendency is observed in both sourceless and source dummy MCs, and it should stem from the simulation settings such as the neutron transport/capture models, cross sections, photon attenuation within Gd-doped water, quantum efficiency of PMTs, etc. Those settings should be further tuned in the future.

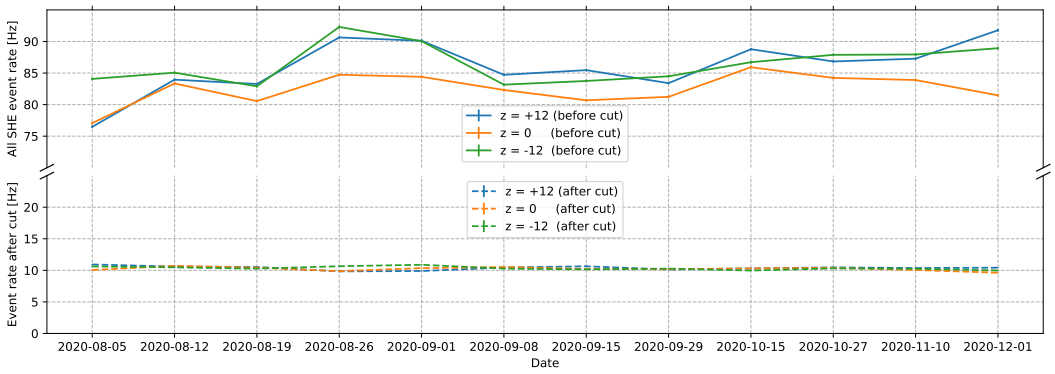

Figure 4.13: SHE-triggered event rates (top) and cut-passing event rates (bottom) by date.

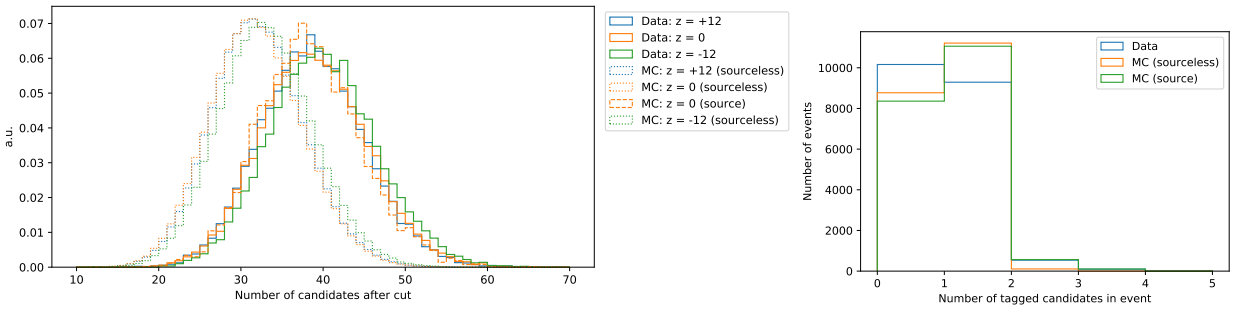

Figure 4.14: Mean number of candidates per event, after all event and candidate cuts. The reason why sourceless dummy MCs have less number of candidates is explained in Figure 4.15.

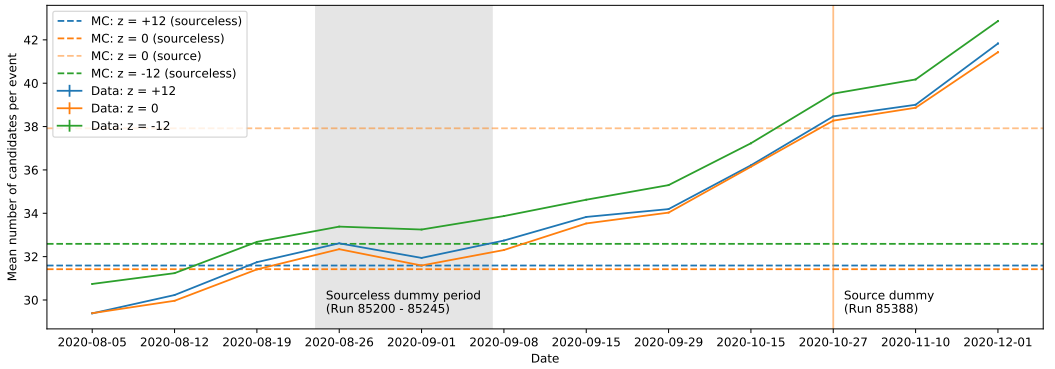

Figure 4.15: Mean number of candidates per event by date. The increase of the number by date has been reported after Gd-loading, and the suspected is the possible bacterial growth within the tank. Asymmetry in z has also been reported for the noise hits [48], which may be a reason why data with $z = 12$ have more candidates than the other two z positions.
The difference in the number of candidates per event shown in Figure 4.14 should come from the difference in the dates the dummy trigger data were taken. Sourceless dummy data were taken from late August to early September, 2020, whereas the source dummy data was taken on October 27$^{\text{th}}$, 2020. Data taken on October 27$^{\text{th}}$ have slightly more candidates than the source dummy, which should be due to the BGO's phosphorescence.

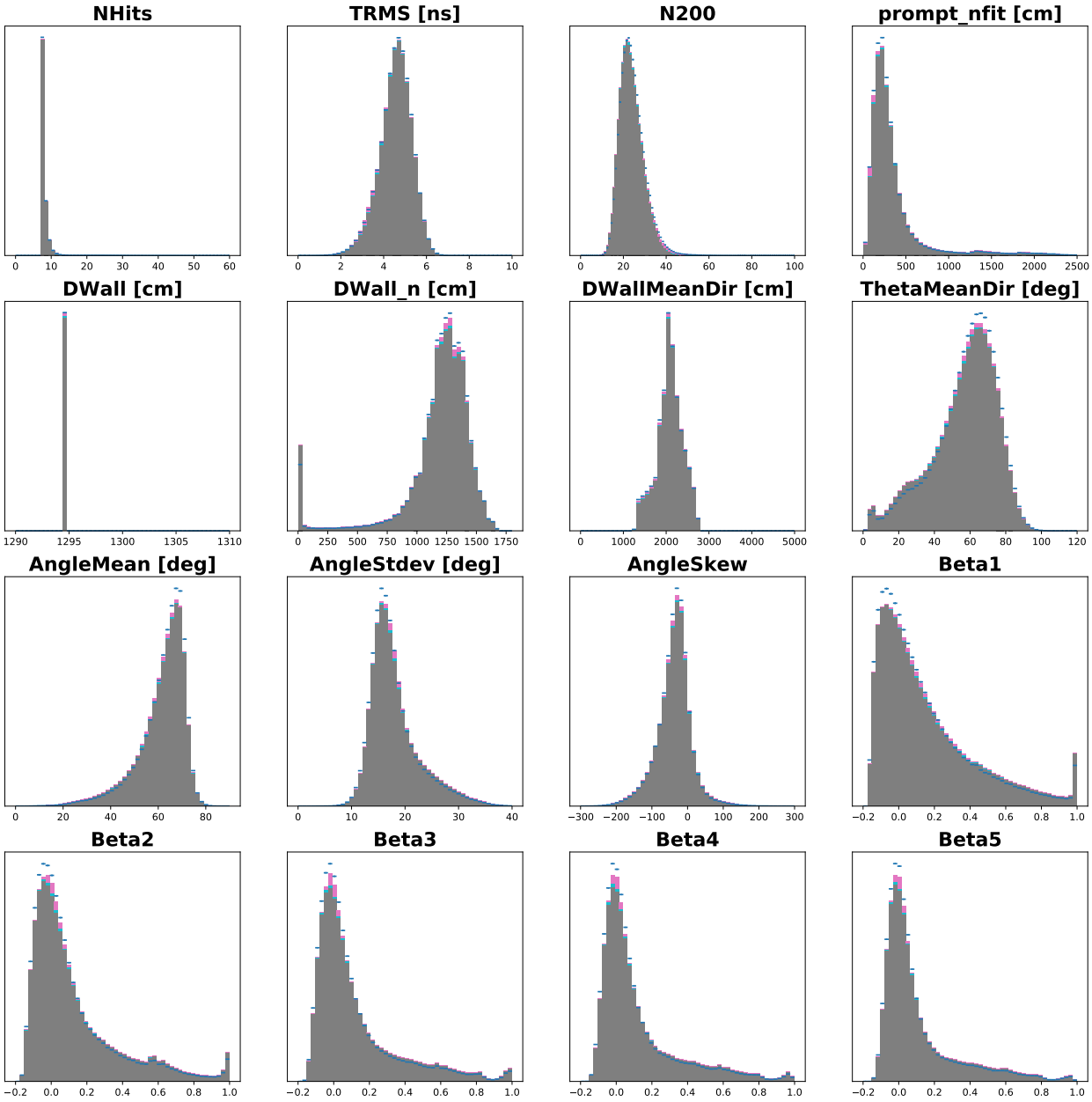

Figure 4.16: Area-normalized feature distributions of sourceless dummy MC and data taken at $z = 0$ (Run 85386), for all selected candidates. (blue: data, pink: MC (Gd), cyan: MC (H), gray: MC (noise))

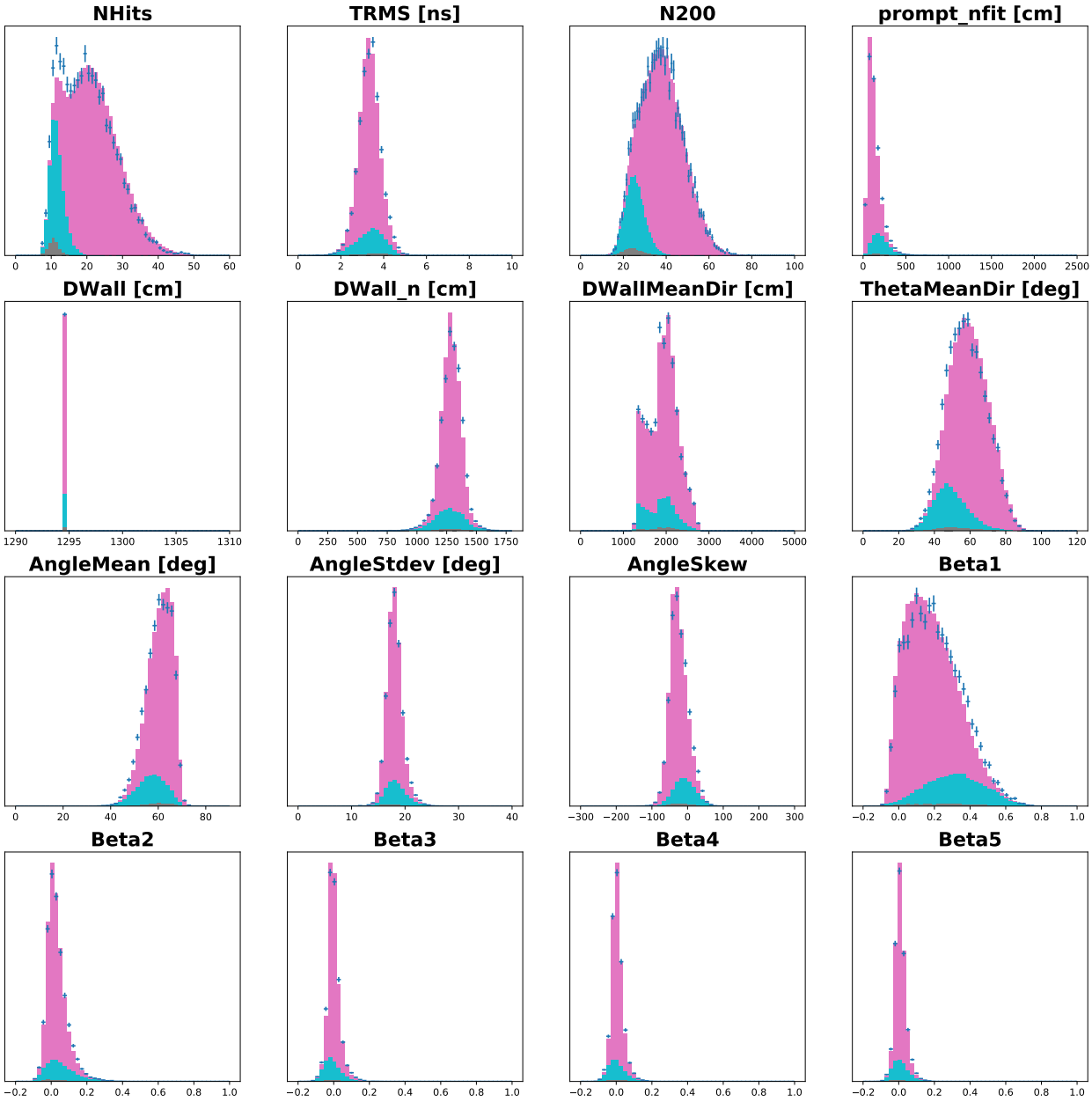

Figure 4.17: Area-normalized feature distributions of source dummy MC and data taken at $z = 0$ (Run 85386), for tagged candidates. (blue: data, pink: MC (Gd), cyan: MC (H), gray: MC (noise))

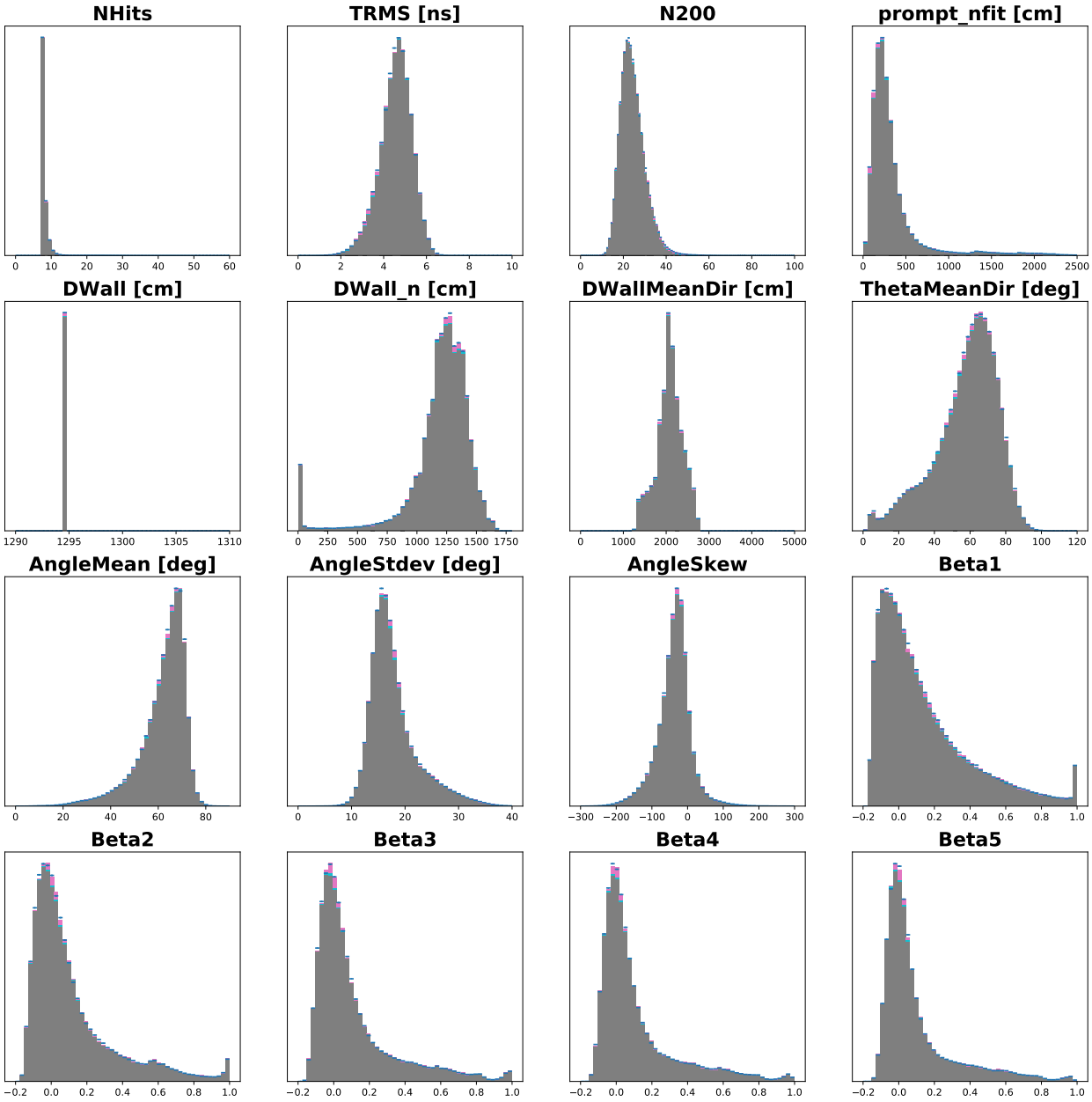

Figure 4.18: Area-normalized feature distributions of source dummy MC and data taken at $z = 0$ (Run 85386), for all selected candidates. (blue: data, pink: MC (Gd), cyan: MC (H), gray: MC (noise))

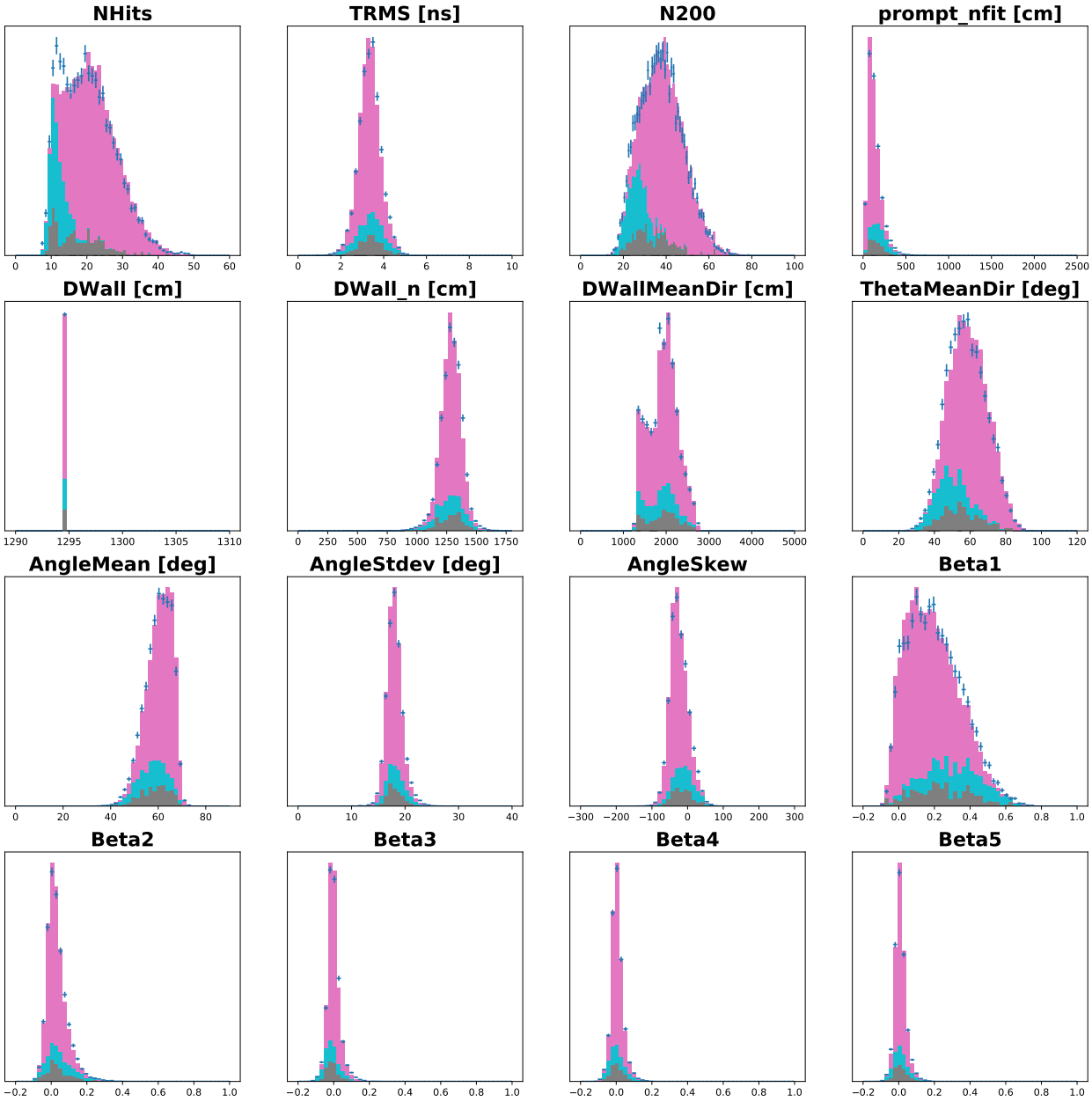

Figure 4.19: Area-normalized feature distributions of source dummy MC and data taken at $z = 0$ (Run 85386), for tagged candidates. (blue: data, pink: MC (Gd), cyan: MC (H), gray: MC (noise))

4.3.2 Signal likelihood

Figure 4.21 shows the signal likelihood distributions of all candidates selected in data and sourceless dummy MC, and Figure 4.20 compares the same distributions of data and source dummy MC, for three source z positions. Overall, the distributions for all three positions seem to have a similar shape, so both the trained MLP and the simplified source simulation with sourceless dummy prove to be effective. One caveat to the source dummy is that it not only includes phosphorescent noise hits, but also random neutron capture gamma-rays which should be very signal-like but definitely should not be classified as signals in MC. A huge increase of candidates with signal likelihood close to 1 between the sourceless dummy MC (center, Figure 4.21) and the source dummy MC (Figure 4.20) can be observed. Another thing to note is that in Figure 4.21, the noise distribution for MC at $z = 12$ m, especially within the range of output likelihood $\in [0.8, 1.0]$, is different from the ones of other two z positions. A reason suspected is the reported increase of low energy noise hits centered around the top of the tank after the Gd-loading was completed [48]. Further investigation is needed.

The neutron capture detection efficiencies $\epsilon_{(n,\gamma)}$ for signal likelihood threshold of 0.7 are listed in Table 4.7. The expected overall neutron capture detection efficiency with sourceless dummy MC was ∼60% for $z = 12$ m and ∼56% for $z = 0$. The z-asymmetry in the noise ratio r_{Noise} is noticeable, which may be due to the reported increase of noise hits near the top of the tank.

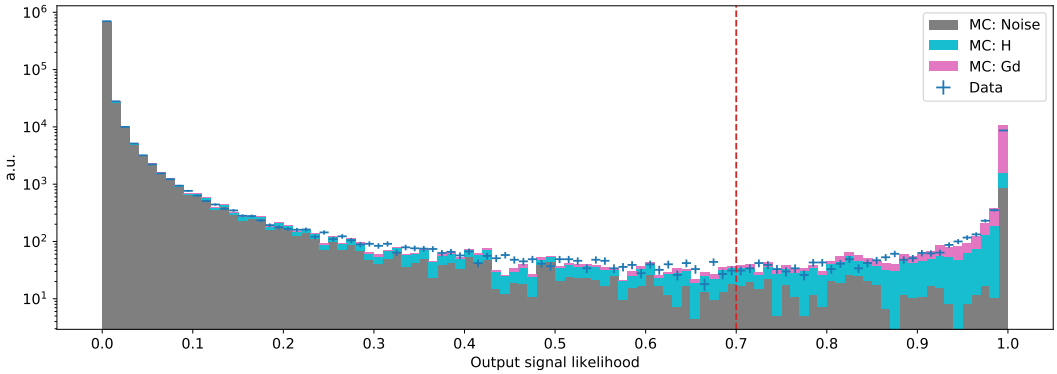

Figure 4.20: Signal likelihood distribution of source dummy MC and data taken at $z = 0$ m (area-normalized). The red dotted line indicates the taggable likelihood threshold of 0.7.

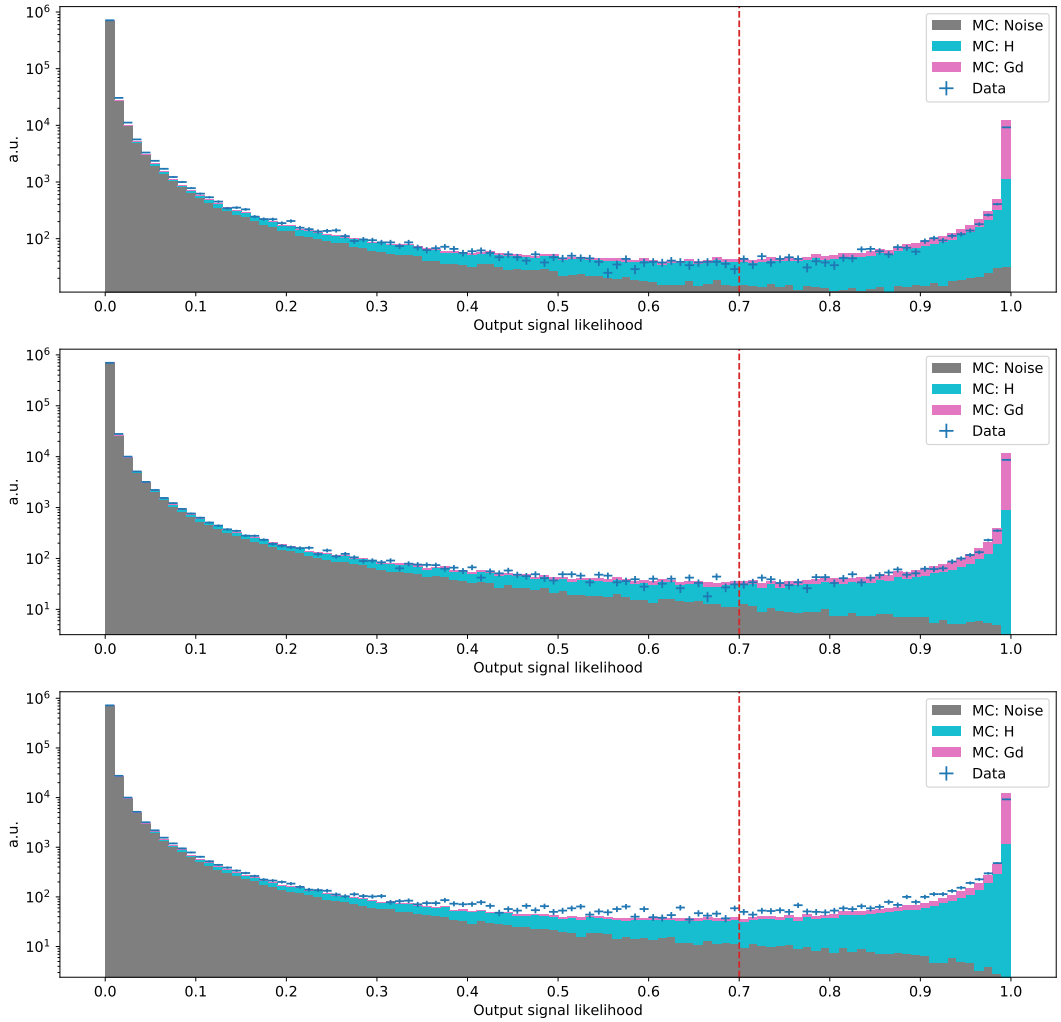

Figure 4.21: Signal likelihood distributions of sourceless dummy MC and data taken at $z = 12$ m (top), $z = 0$ (center), $z = -12$ m (bottom) (area-normalized). The red dotted line indicates the taggable likelihood threshold of 0.7.

			Efficiency (%)			
z [m]	Dummy	Threshold	Gd	H	All	r_{Noise}
12	Sourceless	0.7	95.8	24.0	60.3	3.30
0	Sourceless	0.7	94.7	18.0	56.8	1.68
0	Source	0.7	94.9	17.9	56.9	11.07
-12	Sourceless	0.7	94.1	24.5	59.8	1.54

Table 4.7: Summary of MC neutron capture detection efficiencies, for each source z position. Most of the difference in the noise rate r_{Noise} between source and sourceless dummy MCs should be random uncorrelated neutrons from the source.

4.3.3 Reconstructed capture time

The reconstructed capture time (ReconCT) of a candidate is defined as the mean residual hit time of the earliest and latest hits (in residual time) within a candidate. Considering the maximum residual time width (14 ns) of a candidate and the time resolution of the residual hit time illustrated in Figure 3.9, the reconstructed capture time should give a small enough resolution to fit the exponential distribution of $\tau \sim O(100)$ µs. The reconstructed capture time distributions of data and MC are shown in Figure 4.22. The histograms were fitted with a function of the form $Ae^{-t/\tau} + B$ within ReconCT $\in [15, 535]$ µs. The lower limit of 15 µs is the expected time that neutrons require to thermalize. The mean of the fitted capture time constant τ was 116.7 ± 0.2 µs for data and 112.5 ± 0.4 µs for MC. The two fitted τs disagree, which implies that the neutron capture ratio on Gd is higher for MC than in data, as expected by Figures 4.17 and 4.19. Since the error of the Gd concentration is ∼1%, the Gd capture cross sections or the neutron thermalization process within Geant3 should be checked in the future.

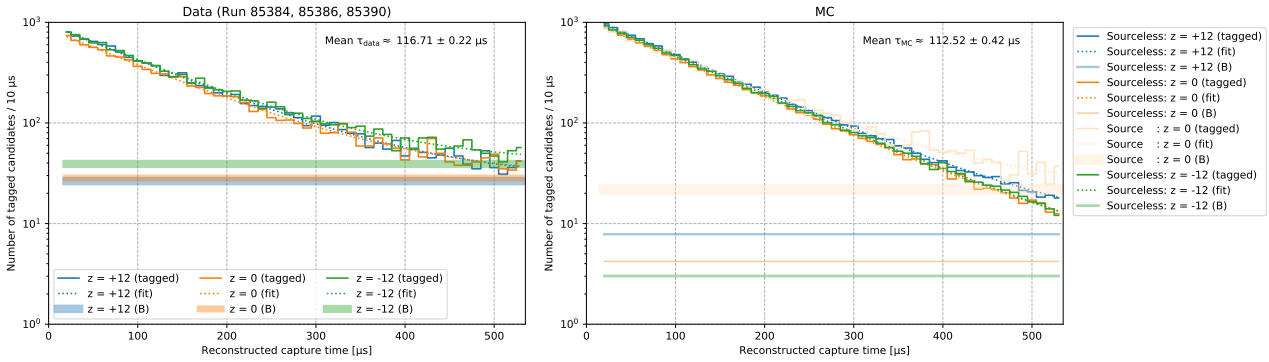

Figure 4.22: Reconstructed capture time distributions of data (left) and MC (right). The MC histogram for each z was scaled by (# of data events of the same z)/(# of MC events).

Figure 4.23 shows the time evolution of the fitted time constant τ for each of the three source z positions. The Gd-loaded water was injected from the bottom of the tank, and we can observe that the fitted τ stabilizes for $z = 12$ m at around September 1st, 2020. The fitted τ of data is slightly larger than that of MC for the same Gd concentration of 0.019 wt.%, as in Figure 4.22.

B, the number of fitted background candidates, is much larger for data events than MC events, as data events include random uncorrelated neutrons from the source. For $z = 0$, the values of fitted B are 142 ± 15, 21 ± 4, and 109 ± 26 tagged candidates per second for data, sourceless

dummy MC, and source dummy MC, respectively. Although the noise levels between the data (Run 85386, Oct. 27, 2020) and the sourceless dummy MC (noise hits taken from late August to early September, 2020) are clearly different as suggested in Figure 4.15, the number of tagged (i.e., signal-like) candidates should not be significantly affected. Thus, the difference between the fitted B for sourceless and source dummy MCs should provide a rough yield of source-induced tagged background candidates. The estimated yield was 88 $\pm$ 26 tagged candidates per second. Assuming roughly the neutron detection efficiency of 55 $\pm$ 10 % for $z = 0$ (based on Table 4.7), we get the estimated source intensity of 160 $\pm$ 57 neutrons per second. This number is in agreement with the source neutron intensity estimates 216 $\pm$ 48 (this study) and 163 $\pm$ 33 (Watanabe et al. [38]), although plagued by huge systematic uncertainties. Also, the number of leaking prompt gamma-rays, that misses the BGO but directly hits the detector to be tagged as signal candidates, as well as the amount of tagged background candidates removed by Event cut 5 (see Table 4.5) is neglected in this estimation. Further study of scintillation and longer measurement of source dummy is needed to fully understand the connection between the source particle intensity and the fitted background B.

Figure 4.24 shows the time evolution of the fitted background B for each of the three source z positions. The fitted Bs seem constant throughout the campaign, except for $z = 12$ m data which show a slight increase of B over time. This may be due to the reported increase of noise hits near the top of the tank [48].

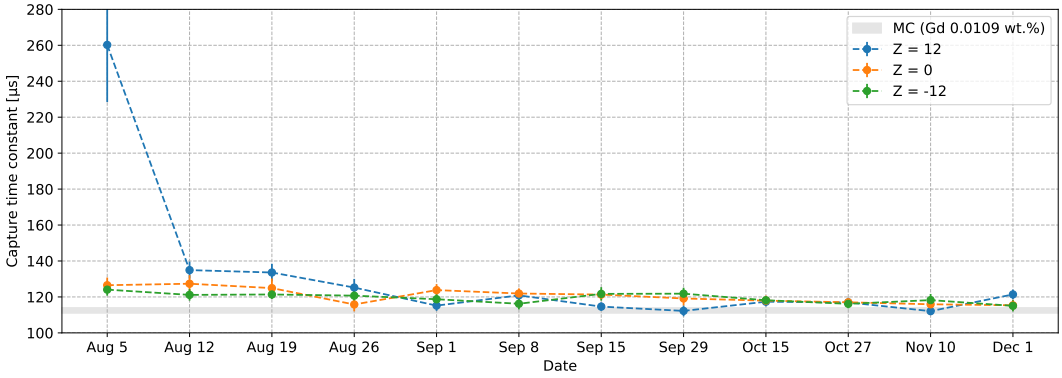

Figure 4.23: Fitted capture time constant τ by date.

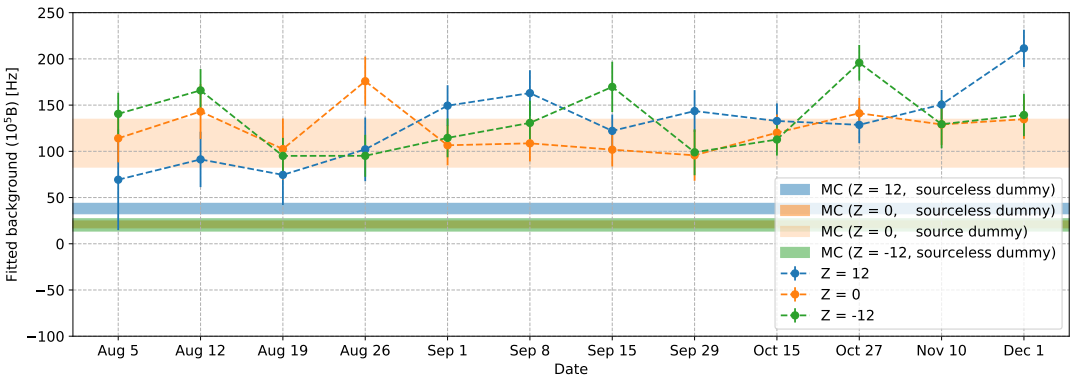

Figure 4.24: Fitted background B by date.

4.3.4 Estimated neutron detection efficiencies

The estimated neutron detection efficiency $\epsilon_n^{\text{est.}}$ of both data and MC was defined as

$$\epsilon_n^{\text{est.}} = \frac{(\#\text{ of tagged candidates}) - (\#\text{ of estimated background candidates})}{(\#\text{ of cut passing events})} \tag{4.2}$$

where the number of estimated background candidates is defined as $B\Delta T/w = 53.1B$. ΔT is the neutron search time range of 531 µs and w is the bin width 10 µs of the reconstructed capture time histogram. The definition of $\epsilon_n^{\text{est.}}$ in Equation 4.2 assumes that each cut passing event has a single emitted source neutron as in each MC event and that all time-correlated neutrons are signals. The true neutron detection efficiency ϵ_n for MC was defined as

$$\epsilon_n^{\text{true}} = \frac{(\#\text{ of tagged signal candidates})}{(\#\text{ of cut passing events})} \tag{4.3}$$

For MC, the number of cut passing events should be the same as the number of emitted neutrons. The estimated neutron detection efficiencies by date for both data and MC are as illustrated in Figure 4.25. We can observe that the neutron detection efficiency for data looks systematically lower than that of MC. The efficiencies of source and sourceless dummy MCs did not show significant discrepancy. The detection efficiencies of data and MC are summarized in Figure 4.25 and Table 4.8. The ϵ_n^{true}'s for MC agree with $\epsilon_n^{\text{est.}}$'s within statistical uncertainties.

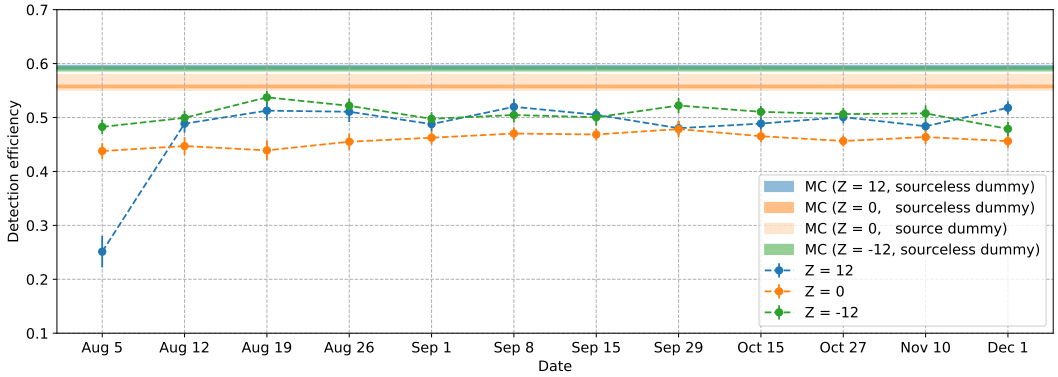

Figure 4.25: Estimated neutron detection efficiency $\epsilon_n^{\text{est.}}$ by date.

z [m]	Data est. (%)	MC est. (%)	Data est./MC est.	MC true (%)	MC dummy
12	49.96 ± 0.44	59.33 ± 0.33	0.84 ± 0.01	59.40	sourceless
0	46.03 ± 0.33	55.76 ± 0.24	0.83 ± 0.02	55.91	sourceless
		56.51 ± 1.45	0.81 ± 0.03	56.07	source
-12	50.79 ± 0.46	59.02 ± 0.38	0.86 ± 0.01	58.91	sourceless

Table 4.8: The estimated neutron detection efficiencies with statistical uncertainties. (Data averaged from August 12$^{\text{th}}$ to December 1$^{\text{st}}$, 2020.)

4.4 Discussion

The following subsections will discuss the possible explanations for the apparent data-MC discrepancy shown in Figure 4.25 and Table 4.8, as well as the currently known sources of systematic bias in the neutron detection efficiency measurement.

4.4.1 Sources of systematic uncertainties

Apart from the data-MC discrepancy, there also exist several sources of systematic uncertainties to the data ϵ_n measurement. The following are the possible sources and the rough estimates of the related uncertainties:

- Noise rate by date

  Apparently the noise level had increased over time within the selected runs, and it can affect the overall tagging efficiency. To verify the effect of the noise level on the detection efficiency $\epsilon_n^{\text{est.}}$, another set of noise hits were extracted from the dummy trigger data taken

on October 27$^{\text{th}}$, 2020, and attached to the $z = 0$ MC. The detection efficiency ϵ_n^{MC} for the sourceless dummy MC was 53.9 ± 1.1 %. Comparing this value with the same ϵ_n^{MC} of the $z = 0$ sourceless dummy MC in Table 4.8, maximum ± 5 % uncertainty is assumed.

- Neutron-induced scintillation

  Neutrons can hit the BGO crystals to make them scintillate, and a few of them can be as bright as scintillation induced by the 4.4-MeV prompt gamma-rays. Moreover, they can be captured close to BGO, or sometimes within BGO to cause scintillation.

  To estimate the amount of such fake triggers within the selected data events, a Geant4-based gamma-correlated neutron MC simulation was carried out along with the BGO geometry and the default Geant4 scintillation model implemented in the simulator. The amount of neutron-induced scintillation was estimated by tracking all interaction products within BGO. The simulated QISMSK distribution was linearly scaled to fit the two QISMSK peaks in data events shown in Figure 4.9. The scaled QISMSK distributions for each interaction channel of neutrons and prompt gamma-rays are given in Figure 4.26. Among 56,748 cut passing MC events, 3,864 events had neutron-induced scintillation. Using the neutron intensity estimates shown in Table 4.1, the neutron-induced scintillation rate within the cut-passing events was estimated to be 12 ± 3 % [49].

  Since neutrons can both scintillate the crystal and leak into the fiducial volume to be detected as signals, the actual percentage of "fake" events without any signal neutron is expected to be lower than 12 %. We assume +10 % uncertainty.

- PMT gain

  About ± 3% uncertainty due to the fluctuation of PMTs' gain is reported by a past study [4], over ∼8 years of time. We disregard the uncertainty in this analysis which was done over a four-months range of runs.

- MLP classification reliability

  About ± 5% uncertainty on the MLP classification was imposed by a past study [4]. We impose the same for this study.

Table 4.9 summarizes the above listed sources of systematics. According to Tables 3.5 and 4.7,

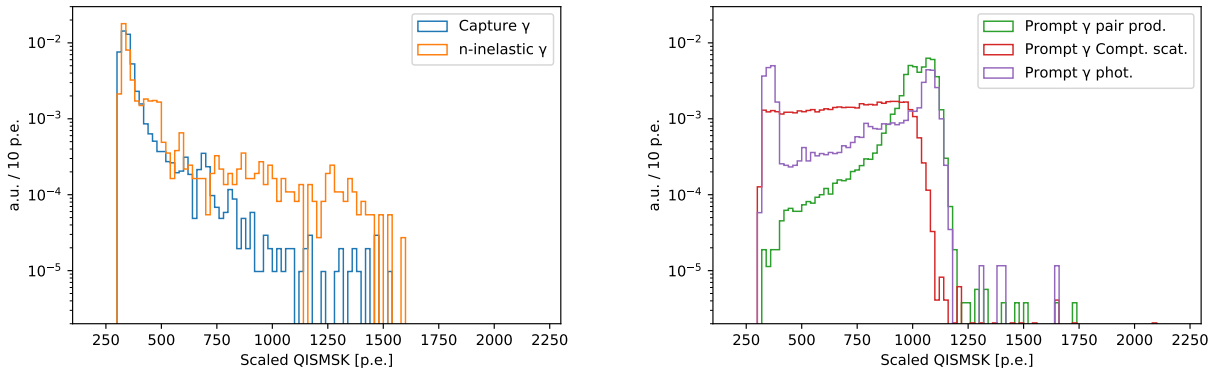

Figure 4.26: Scaled QISMSK distributions by interaction channels, for gamma-correlated neutrons (left) and for prompt gamma-rays (right). (area-normalized) The probability that neutrons will mimic the 4.4-MeV scintillation (i.e., QISMSK∼1,000 p.e.) is $O(10^{-2})$ lower than the prompt gamma-rays.

the true neutron capture detection efficiency $\epsilon_{(n,\gamma)}$ of sourceless dummy MCs for $z = \pm 12$ m (60.3 % for $z = 12$ m, 59.8 % for $z = -12$ m) are closer to that of random vertex MC (60.5 %). We estimate the overall neutron detection efficiency of the SK detector by taking the mean of the two $z = \pm 12$ m results, as $50\ ^{+8}_{-6}$ (sys.) ± 1 (stat.) %.

Source	Fractional uncertainty (%)
Noise rate	$(-5, +5)$
Fake triggers	$(-0, +10)$
MLP classification	$(-5, +5)$
Total	$(-7, +12)$

Table 4.9: Summary of the possible sources of systematic errors and their rough fractional uncertainty estimates. All errors are assumed to be normal and independent.

4.4.2 The data-MC discrepancy

There are several factors within our MC, that are likely to cause the data-MC discrepancy:

- Gd concentration in MC

  Although rather unlikely, the input Gd concentration to the MC, which is based on the total input Gd-sulfate mass to the detector system, might simply have been overestimated compared to the true concentration within the tank after purification, resulting in a higher detection efficiency and a lower capture time constant ($\tau_{\mathrm{MC}} \approx 113$ µs, $\tau_{\mathrm{Data}} \approx 116$ µs).

- Lack of BGO in MC

  A few source neutrons can mimic the 4.4-MeV scintillation of prompt gamma-rays. Events triggered by such neutron-induced scintillation are expected to lack detectable neutrons, and thus become a source of systematic bias, lowering the estimated detection efficiency. A simulation with the BGO geometry and a scintillation model tuned to the current measurement is required to estimate the bias.

- Neutron physics (neutron transport/capture models and cross sections)

  The fraction of neutron captures on Gd is apparently higher in MC than in data, according to the feature distributions and the fitted capture time constants. Different neutron physics models and cross sections should be tested to estimate the model-dependent bias.

- Untuned detector characteristics (photon attenuation in Gd-loaded water, PMT QE, etc.)

  Almost two years have passed since the detector characteristics applied in the SK simulator were last tuned during the pure water phase (SK4). Those parameters can affect the horizontal placement of the *NHits* distributions of signal candidates, increasing/decreasing overall *NHits* of candidates.

Table 4.10 compares the measured neutron detection efficiencies plus their rough systematic estimates with the same efficiencies of the MC event sets, including one with a lowered Gd mass fraction ($\sim$0.0103 wt.%) to match the (n, γ) capture time constant of $\sim$116 µs of data. While the tuned MC efficiencies for $z = \pm 12$ m are within the bounds of the systematics, the two efficiencies still disagree for $z = 0$. It suggests that the Gd concentration in MC alone cannot be a sole cause of the data-MC discrepancy. The possible relative significance of the aforementioned factors are discussed in Appendix D, by fitting a parameterized *NHits* distribution based on a hypothesis that the gamma-ray production model and the detector characteristics are fully compatible with data.

z [m]	Data eff. (%)	Sys. (%)	Tuned MC eff. (%)	Untuned MC eff. (%)
12	50	$^{+6}_{-4}$	54	59
0	46	$^{+6}_{-3}$	55	56
-12	51	$^{+6}_{-4}$	57	59

Table 4.10: The measured neutron detection efficiencies and the rough systematic estimates. The statistical uncertainties are neglected. The tuned MC efficiencies are taken from the MC with its Gd cocentration lowered to ∼0.0103 wt.% to match the fitted neutron capture time constant to the one measured in data (∼116 µs).

4.4.3 Future work

Below is the list of future work:

- BGO and trigger simulation

  Geant4-based simulation is under development. The BGO-geometry is fully implemented, and scintillation physics is yet to be tuned. If the BGO simulation combined with SHE trigger simulation can reproduce the data QISMSK peak, we would be able to decompose the peak and estimate the amount of fake triggers within the cut-passing events.

- Neutron physics models

  Different models should be tested to estimate the model-dependent systematic.

- Tuning detector simulation parameters, stabilizing the noise level

  The systematic coming from the untuned detector characteristics in simulation should be ruled out to better analyze the significance of the fake triggers and the physics model.

- Longer source/dummy measurement with different positions

Chapter 5

Summary and prospects

To improve visibility of neutrino-induced neutrons, the SK detector has fully loaded Gd — the most powerful element known in capturing thermal neutrons — with 0.0110 wt.% concentration since the end of July, 2020. Although some of the parameters still remain tuned to the pure water phase, a new simulation framework with the recent $p(n,\gamma)$/Gd(n,γ) models and cross sections implemented has become ready for use since September, 2020.

To evaluate the detector's achievable neutron detection efficiency, we have inherited the same neutron detection algorithm [1, 3, 4] that has been used so far within SK for $p(n,\gamma)$ detection. The algorithm consists of two stages; in Stage 1, we pick out any cluster of PMT hits that are tightly localized in the ToF-corrected time frame, and in Stage 2, we categorize those selected clusters into signal and noise according to the signal likelihood output of the pre-trained MLP. The parameters that characterize Stage 1 were tuned in this study to maximize neutron detection efficiency in the Gd-loaded (0.0110 wt.%) SK's single neutron MC (detailed in Section 3.1) with the Geant4 neutron cross section library and the ANNRI-Gd model as neutron capture physics models. A new MLP was designed and trained on 300,000 single neutron (with random vertex) MC events generated by the same simulation framework. With this detection algorithm and the realistic neutron search time range of $[T_0{+}3,\ T_0{+}534]$ µs where the neutron production time $T_0 = 1$ µs, the neutron capture detection efficiency obtained on a test MC dataset was ∼92 % for Gd(n,γ) captures, ∼26 % for $p(n,\gamma)$ captures, and ∼61 %

overall. The parameter optimization and the training of MLP to Gd-loaded detector MC have not affected the $p(n,\gamma)$ neutron detection efficiency in pure water (only) which was reported to be ∼25 % by the past studies [1, 3, 4].

The same algorithm was applied to both AmBe neutron source data and single neutron MC. The signal likelihood and feature distributions showed reasonable agreement between data and MC, proving the effectiveness of our primitive approach that neglects complex source geometry and simplifies the detector trigger system. However, the MC showed higher neutron capture ratio on Gd than in data, which should be one of the causes for the discrepancy in the estimated neutron detection efficiencies between data (∼50 %) and MC (∼60 %). Another source of the apparent discrepancy should be fake neutron event triggers due to scintillation induced by source neutrons, which are not at all accounted for in MC. The neutron physics models, cross sections, untuned detector parameters, and fluctuation in the detector dark noise level should cause bias as well. Roughly estimating the systematics, we set 50^{+6}_{-4} %, 46^{+6}_{-3} %, 51^{+6}_{-4} % for each z being 12, 0, -12 m, as the neutron detection efficiencies of the algorithm and the current SK detector of 0.0110 wt.% Gd.

We hope to lower the uncertainties in the neutron detection efficiency measurement, which is the major systematic in the neutron multiplicity of neutrino-nucleus interaction. Enhanced neutron detection efficiency with smaller uncertainty would definitely accelerate mass hierarchy and CP violation search with atmospheric/beam neutrinos and supernova relic neutrino search.

Appendix A

Neutrino oscillation

The three neutrino weak flavor eigenstates that have been discovered so far form a complete, orthonormal basis for the three lepton generations of the Standard Model. If the neutrinos were massive, we may define another complete, orthonormal basis of three mass eigenstates, and this basis should not necessarily coincide with the flavor basis. Let the flavor eigenstate be a coherent superposition of the mass eigenstates, related by a 3×3 unitary matrix U:

$$|\nu_l\rangle = \sum_k U_{lk}^* |\nu_k\rangle \tag{A.1}$$

where $|\nu_l\rangle$ is the flavor eigenstate of flavor $l \in \{e, \mu, \tau\}$, and $|\nu_k\rangle$ is the k-th mass eigenstate where $k \in \{1, 2, 3\}$. If the neutrino mass eigenvalues are non-degenerate, an interesting phenomenon can happen. Let $|\nu\rangle$ denote a neutrino state that has been produced via weak interaction as $|\nu_l\rangle$ at time $x^0 = 0$. Then, each mass eigenstate should gain a distinct phase as it propagates in (vacuum) spacetime, so that

$$\begin{aligned} |\nu(x)\rangle &= \sum_k U_{lk}^* |\nu_k\rangle \, e^{-i\phi_k(x)} \\ &= \sum_{l',k} U_{lk}^* U_{l'k} |\nu_{l'}\rangle \, e^{-i\phi_k(x)} \end{aligned} \tag{A.2}$$

where $\phi_k(x) \coloneqq p_k \cdot x$ is the phase gain of $|\nu_k\rangle$ after propagation x.

Naturally, the probability that the state $|\nu\rangle$ that has started out with flavor l will be detected to have another flavor l' is

$$\begin{aligned} P(\nu_l \to \nu_{l'})(x) &= \left| \sum_k U^*_{lk} U_{l'k} e^{-i\phi_k(x)} \right|^2 \\ &= \delta_{ll'} + 2\mathrm{Re} \sum_{k' \neq k} \left[U^*_{lk} U_{l'k} U_{lk'} U^*_{l'k'} e^{-i\Delta\phi_{kk'}(x)} \right] \end{aligned} \tag{A.3}$$

where $\Delta\phi_{kk'}(x) \equiv \phi_k(x) - \phi_{k'}(x)$. If all mass eigenstates propagate in-phase, i.e., the neutrino masses are degenerate so that $\phi_k(x)$ is the same for all k, $P(\nu_l \to \nu_{l'}) = \delta_{ll'}$ by the unitarity of U, and thus there is zero chance that a certain flavor eigenstate will change its flavor as it propagates. But if the neutrino masses are non-degenerate so that the mass eigenstates become out-of-phase, the probability in Equation A.3 should be non-zero for $l \neq l'$. Such flavor transition allowed by the non-degeneracy of neutrino masses is called "oscillation," due to the sinusoidal form of the transition probability in Equation A.3. The oscillation of neutrinos have been confirmed by experiments for various sources: solar, atmospheric, and artificial.

In the ultrarelativistic limit, $\phi_k(x)$ reduces to $\phi_k(x) \approx m_k^2 L/2E$, where m_k is the non-degenerate mass of the k-th mass eigenstate $|\nu_k\rangle$, $L = |\vec{x}|^2$ is the distance that the neutrino has traveled, and $E = p_k^0 = E_\nu$ is assumed to be the energy of the neutrino, same for all k. Hence, the oscillation probability $P(\nu_l \to \nu_{l'})$ depends on the components of the so-called neutrino mixing (or the PMNS) matrix U, the squared differences $\Delta m^2_{kk'} \equiv m_k^2 - m_{k'}^2$ of two distinct neutrino masses, and the neutrino's kinematics: the traveled distance L and the neutrino energy E.

In a scenario where only the Dirac masses are concerned, the unitary 3×3 neutrino mixing matrix U is parameterizable with four real free parameters, considering the neutrino and lepton spinors of three generations absorbing the relative phases and removing $\binom{3}{2} - 1$ degrees of freedom from U, so that only the remaining four degrees of freedom can be actually physical. The standard way of parameterizing the mixing matrix U is:

$$\begin{bmatrix} \nu_e \\ \nu_\mu \\ \nu_\tau \end{bmatrix} = \begin{bmatrix} 1 & 0 & 0 \\ 0 & \cos\theta_{23} & \sin\theta_{23} \\ 0 & -\sin\theta_{23} & \cos\theta_{23} \end{bmatrix} \begin{bmatrix} \cos\theta_{13} & 0 & \sin\theta_{13}e^{-i\delta_{\mathrm{CP}}} \\ 0 & 1 & 0 \\ -\sin\theta_{13}e^{i\delta_{\mathrm{CP}}} & 0 & \cos\theta_{13} \end{bmatrix} \begin{bmatrix} \cos\theta_{12} & \sin\theta_{12} & 0 \\ -\sin\theta_{12} & \cos\theta_{12} & 0 \\ 0 & 0 & 1 \end{bmatrix} \begin{bmatrix} \nu_1 \\ \nu_2 \\ \nu_3 \end{bmatrix} \tag{A.4}$$

where θ_{ij} for $i, j \in \{1, 2, 3\}$ are the mixing angles that represent the internal mixing of mass eigenstates, and δ_{CP} represents the overall complex phase of U. Note that the complex phase is not allowed for the eigenspace dimension smaller than 3. The complex phase of the mixing matrix U allows for the CP violation (CPV), i.e., a non-zero difference between the oscillation probabilities of neutrinos and antineutrinos, according to Equation A.3. The three mixing angles θ_{ij}, the (Dirac) CP phase δ_{CP}, and the two independent neutrino mass-squared differences Δm^2_{21} and Δm^2_{32} are the fundamental parameters that fully characterize the oscillation with a given neutrino energy and propagation. These are called the neutrino oscillation parameters.

Most of the oscillation parameters except δ_{CP} are relatively precisely measured as in Table A.1. δ_{CP} remains largely unknown, while CP conservation ($\delta_{CP} = 0$ or π) is disfavored according to the recent data analysis [18]. A non-zero and non-π δ_{CP}, if precisely measured, may account for the matter-dominant universe, as the same possible CP violation currently observed in the quark sector is known to be either non-existent or extremely small. Another pending problem is the sign of Δm^2_{32}. The sign is not known yet, as the leading order (vacuum) oscillation probability is not sensitive to its sign. This problem is called the neutrino mass hierarchy (MH) problem. If $\Delta m^2_{32} > 0$, i.e., $m_3 > m_2 > m_1$, we call this scenario the normal hierarchy (NH), and if $\Delta m^2_{32} < 0$, i.e., $m_2 > m_1 > m_3$, we call this scenario the inverted hierarchy (IH). The mass hierarchy problem is correlated with the CPV search to some extent, as in matter unlike in vacuum, the sign of Δm^2_{32} can fake CPV to a different extent between neutrinos and antineutrinos.

Parameter	Best-fit	3σ range	3σ error
$\lvert\Delta m^2_{32}\rvert$	2.525	2.411 – 2.646	9.31%
Δm^2_{21}	7.37	6.93 – 7.96	13.8%
$\sin^2\theta_{13}$	0.0215	0.0190 – 0.0240	23.3%
$\sin^2\theta_{12}$	0.297	0.250 – 0.354	35.0%
$\sin^2\theta_{23}$	0.425	0.381 – 0.615	55.1%
δ_{CP}/π	1.38	$0 - 0.17 \oplus 0.76 - 2$	102%

Table A.1: Recent (circa 2017) best-fit values, 3σ ranges, and errors for the oscillation parameters, assuming normal mass hierarchy ($m_1 < m_2 < m_3$). The unit of Δm^2_{32} is $10^{-3}\,\mathrm{eV}^2$, and the unit of Δm^2_{21} is $10^{-5}\,\mathrm{eV}^2$ [50]

Figure A.1: Feynman diagrams for $\nu_l n$ (left) and $\bar{\nu}_l p$ (right) CCQE interactions.

In practice, we indirectly assume the presence of neutrinos by detecting the products of neutrinos' weak interactions with matter, i.e., matter nuclei and bound electrons. The weak interaction between neutrinos and the other fermions can occur either through charged current (CC) exchange mediated by one of the two W bosons (W^+, W^-), or through neutral current (NC) exchange mediated by the neutral Z boson. All neutrinos can elastically scatter off a bound electron via NC exchange, and ν_e can do the same via CC exchange as well. Although the neutrino-electron scattering cross section is theoretically well-estimated, the interaction is far rarer than the neutrino-nucleon scattering by $O(10^{-3})$ for moderate neutrino energies ($\sim$1 GeV). While neutrinos can go through NC exchange to interact with and scatter nucleons, a more dominant and visible interaction channel with nucleons of sub-GeV neutrinos is the CC quasi-elastic (CCQE) interaction, where neutrinos exchange a W boson with a nucleon to produce a clearly detectable charged lepton (whose nonzero mass explains the name *quasi*-elastic) and a recoil nucleon which is invisible more than often in experiments. The simplified feynman diagrams of νn and $\bar{\nu} p$ CCQE interactions are shown in Figure A.1.

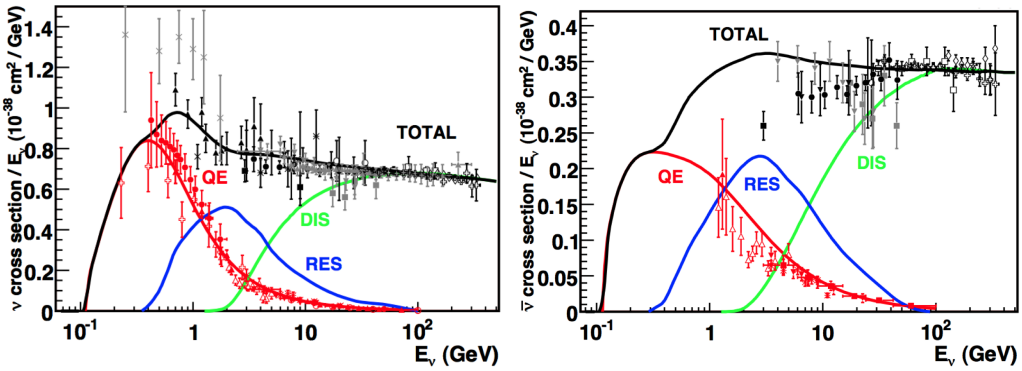

Figure A.2: The theoretical and experimental values of neutrino-nucleon (left) and antineutrino-nucleon CC interaction cross sections (right). Reprinted from Ref. [51].

Due to the simplicity of the interaction, relatively high cross section, and the detectability of a recoil charged lepton, most of the detected neutrino event statistics that are used to constrain the oscillation parameters are dominated by CCQE. In reality, the neutrino targets are not free nucleons, and the neutrinos technically interact with each nucleon bound to a nucleus. Although the possible intranuclear interactions of the neutrino-nucleon final states — also known as the final state interactions (FSI) — complicates the event topology and makes it challenging to model the dynamics, in the ideal 2-body CCQE scenarios $\nu_l + {}^{Z}_{A}\mathrm{X} \rightarrow l^- + {}^{Z-1}_{A}\mathrm{X}^* + p$ and $\bar{\nu}_l + {}^{Z}_{A}\mathrm{X} \rightarrow l^+ + {}^{Z-1}_{A-1}\mathrm{Y}^* + n$ with one outgoing lepton l and one nucleon n/p each, the energy of the incoming neutrino E_ν can be kinematically deterimined as

$$E_\nu = \frac{(m^{\mathrm{in}}_{n/p})^2 - (m^{\mathrm{out,\ eff}}_{n/p})^2 - m_l^2 + 2(m^{\mathrm{out,\ eff}}_{n/p})E_l}{2(m^{\mathrm{out,\ eff}}_{n/p} - E_l + p_l \cos\theta_l)} \tag{A.5}$$

where $m^{\mathrm{in}}_{n/p}$ is the mass of the incoming nucleon, $m^{\mathrm{out,eff}}_{n/p} \approx m^{\mathrm{out}}_{n/p} - E_b$ is the effective mass of the outgoing nucleon considering the nuclear binding energy E_b, and m_l, E_l, p_l, and θ_l are each the mass, energy, momentum, and scattering angle of the outgoing lepton.

Appendix B

Neutron production mechanism of AmBe neutron source

The ^{241}Am is an alpha-decaying isotope with a half-life of ∼432 years:

$$^{241}\mathrm{Am} \xrightarrow{432\ \text{years}} {}^{237}\mathrm{Np} + {}^{4}\alpha(5.5\ \text{MeV}) + \gamma(59.5409\ \text{keV}) \tag{B.1}$$

The long half-life of ^{241}Am ensures stable intensity throughout a long period of time, unlike spontaneous fission neutron source like ^{252}Cf. Since the second most frequent decay channel has a branching ratio of $O(10^{-12}$, we can regard all ^{241}Am isotopes undergo the alpha decay described in Equation B.1.

The AmBe source is a mixture of ^{241}Am, the alpha emitter, and ^{9}Be, the alpha absorber. The source itself is designed to be a stainless steel casing encapsulating the Americium-oxide and Be metallic powder. When bombarded with alpha particles, ^{9}Be absorbs one of those to form a compound nucleus of $^{13}\mathrm{C}^{*}$, which instantaneously decomposes into $^{12}\mathrm{C}^{*}$ and a neutron. The Q-value is 5.7 MeV and thus exothermic, and kinematically alpha with zero kinetic energy can make this reaction happen. The excited $^{12}\mathrm{C}^{*}$ can be in one of the few possible energy levels including the ground state, and if it is in the first excited state (4.44 MeV, spin-parity 2^{+}), it de-excites with emitting the same energy gamma-ray. In the second excited state (7.66

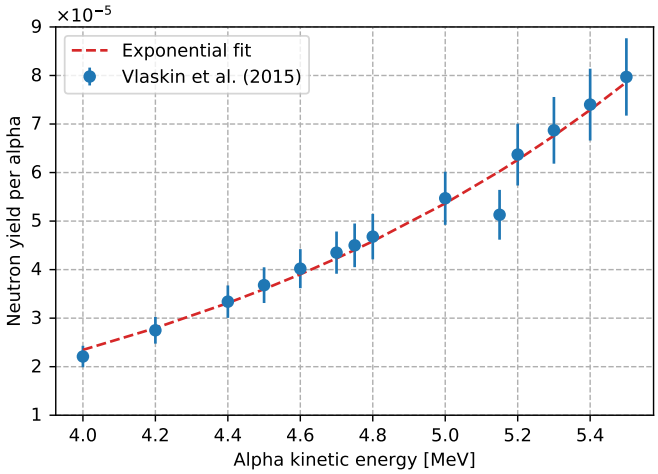

Figure B.1: The neutron yield per alpha from measurement. 10% errors assumed for all data points. [52] Exponential $ae^{-bx} + c$ fit gives a good approximation.

MeV) that happens with alpha threshold energy of ∼2 MeV, it de-excites with emitting an alpha particle and rarely a gamma-ray. For the third and higher excited states, it undergoes a breakup reaction of emitting 3 alpha particles. This should be negligible for AmBe. The neutron emission process correlated with 4.4 MeV gamma-ray is described in the equations below.

$$^{9}\mathrm{Be} + \alpha \rightarrow {}^{13}\mathrm{C}^{*} \rightarrow {}^{12}\mathrm{C}^{*} + n + Q(5.704\ \mathrm{MeV}) \tag{B.2}$$

$$^{12}\mathrm{C}^{*} \xrightarrow{\sim 60\%} {}^{12}\mathrm{C} + \gamma_1(4.438\ \mathrm{MeV}) \tag{B.3}$$

Considering the measured cross sections of each channel of $^{9}\mathrm{Be}(\alpha, n)^{12}\mathrm{C}$ reaction with the kinetic energy of α being $\sim$ 5.5 MeV, about 78% of the fast neutrons emitted via Equation B.2 should be correlated with 4.4 MeV gamma-rays. However in reality, the alpha particles may slow down before they are absorbed. Z. Liu et al [37] recommends the R-value, or the 4.438 MeV gamma-ray to the total neutron ratio, of $0.575 \pm 4.8\%$ which should be dependent on the AmBe capsule, oxygen component, etc.

Appendix C

Feature distributions of neutron source data and MC for nonzero heights

The following are the feature distributions of neutron source data and MC for $z = \pm 12$ m:

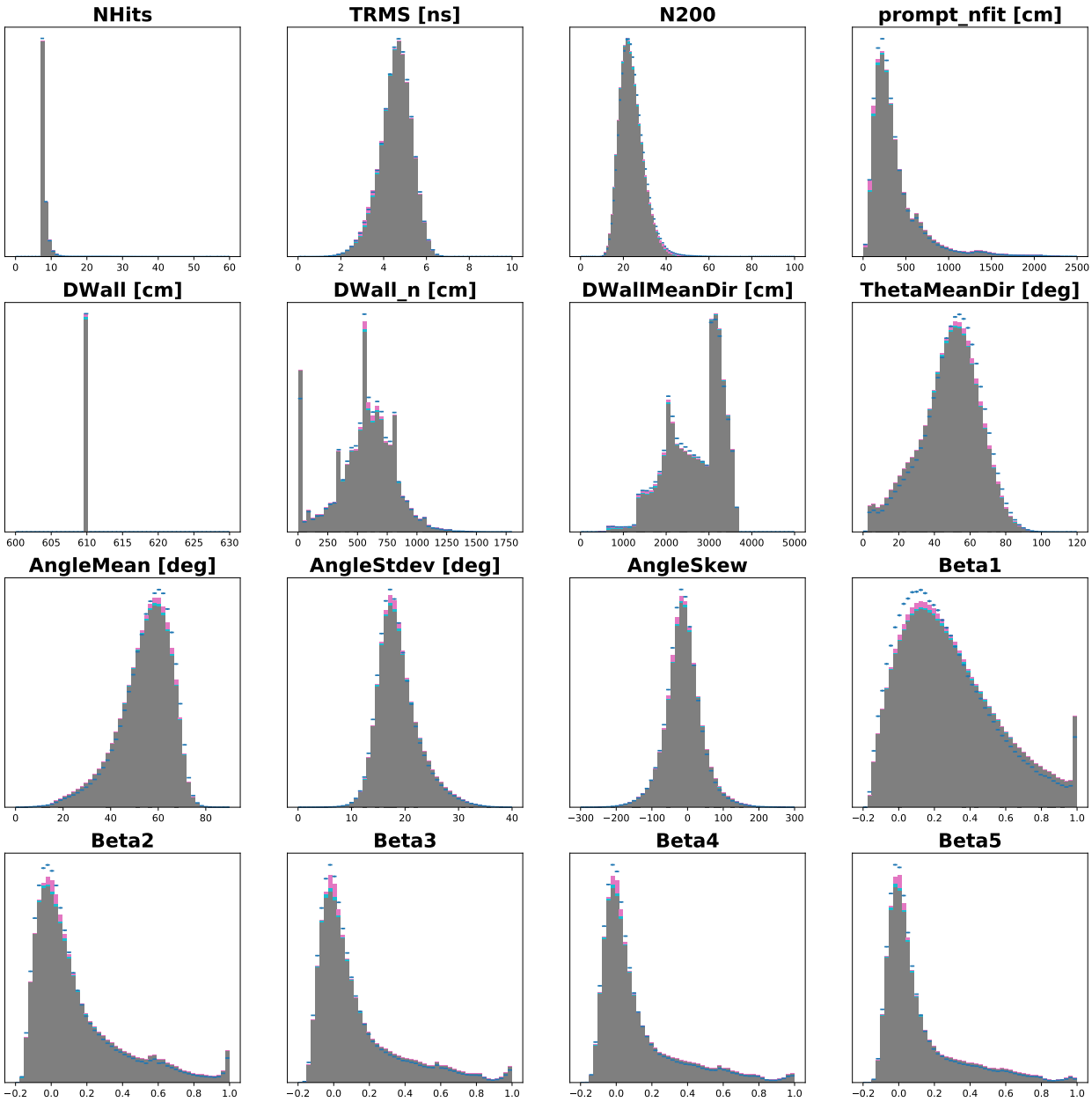

Figure C.1: Feature distributions of source dummy MC and data taken at $z = 12$ m (Run 85390), for all candidates. (blue: data, pink: MC (Gd), cyan: MC (H), gray: MC (noise))

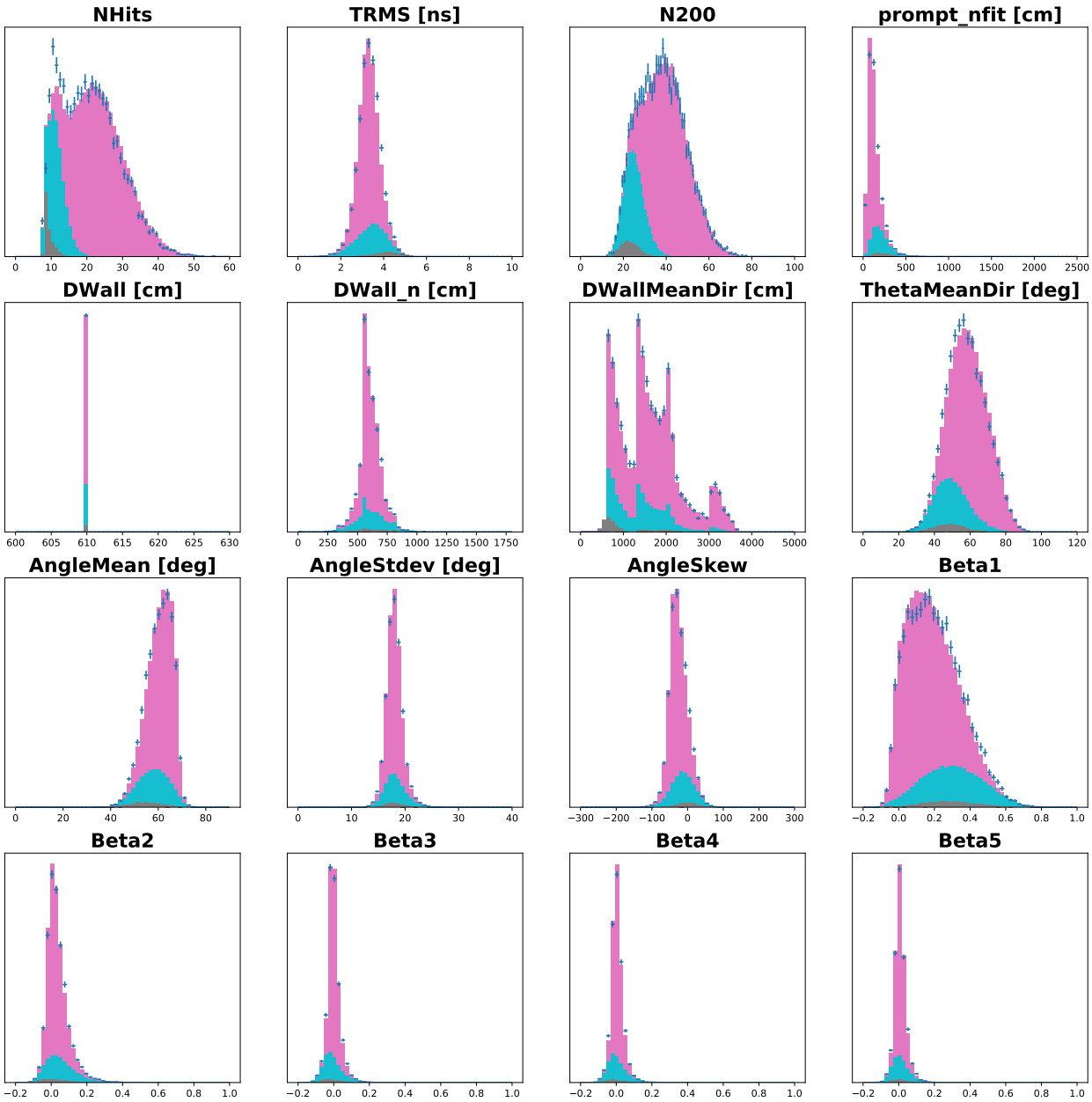

Figure C.2: Feature distributions of source dummy MC and data taken at $z = 12$ m (Run 85390), for tagged candidates. (blue: data, pink: MC (Gd), cyan: MC (H), gray: MC (noise))

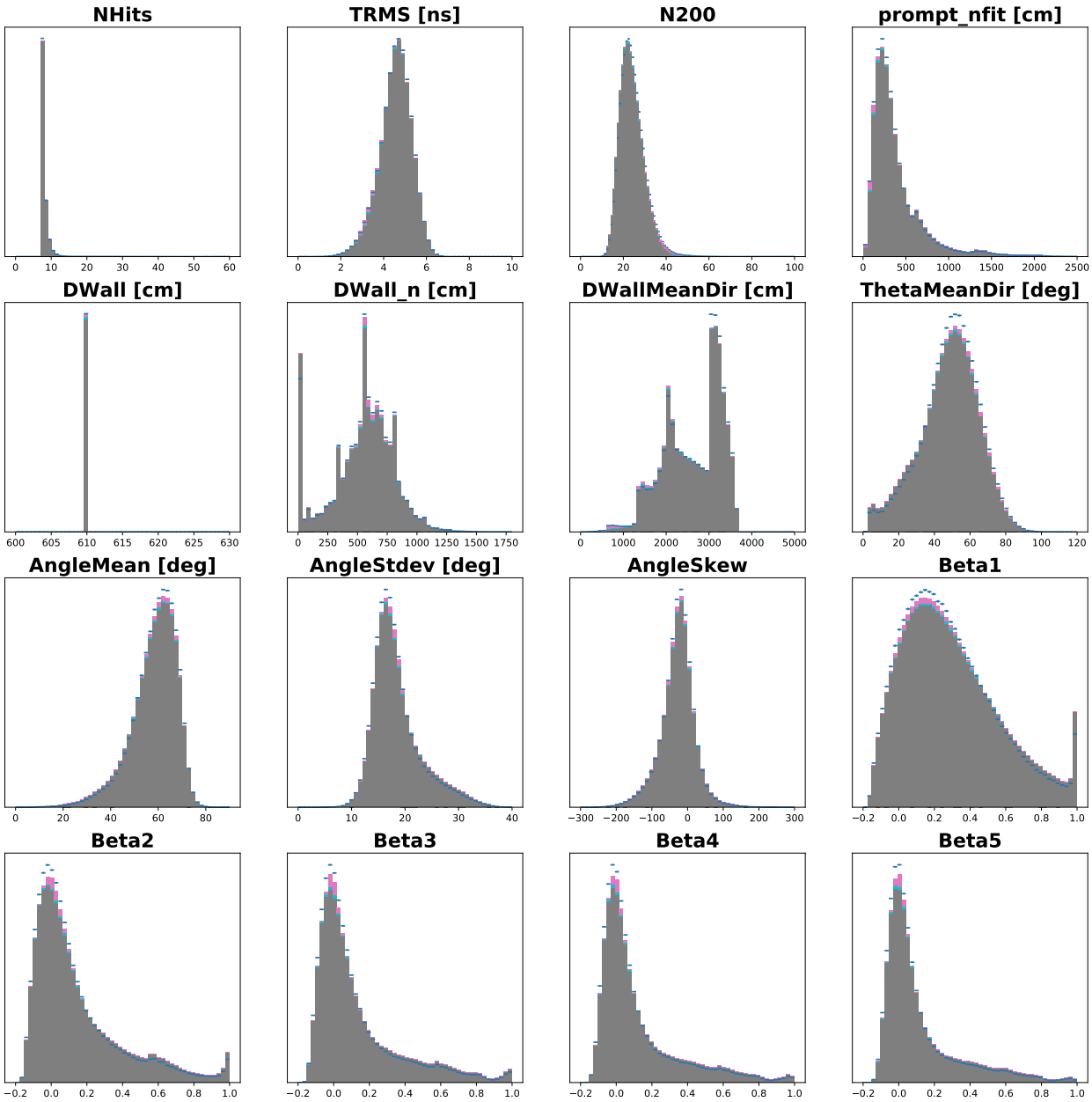

Figure C.3: Feature distributions of source dummy MC and data taken at $z = -12$ m (Run 85384), for all candidates. (blue: data, pink: MC (Gd), cyan: MC (H), gray: MC (noise))

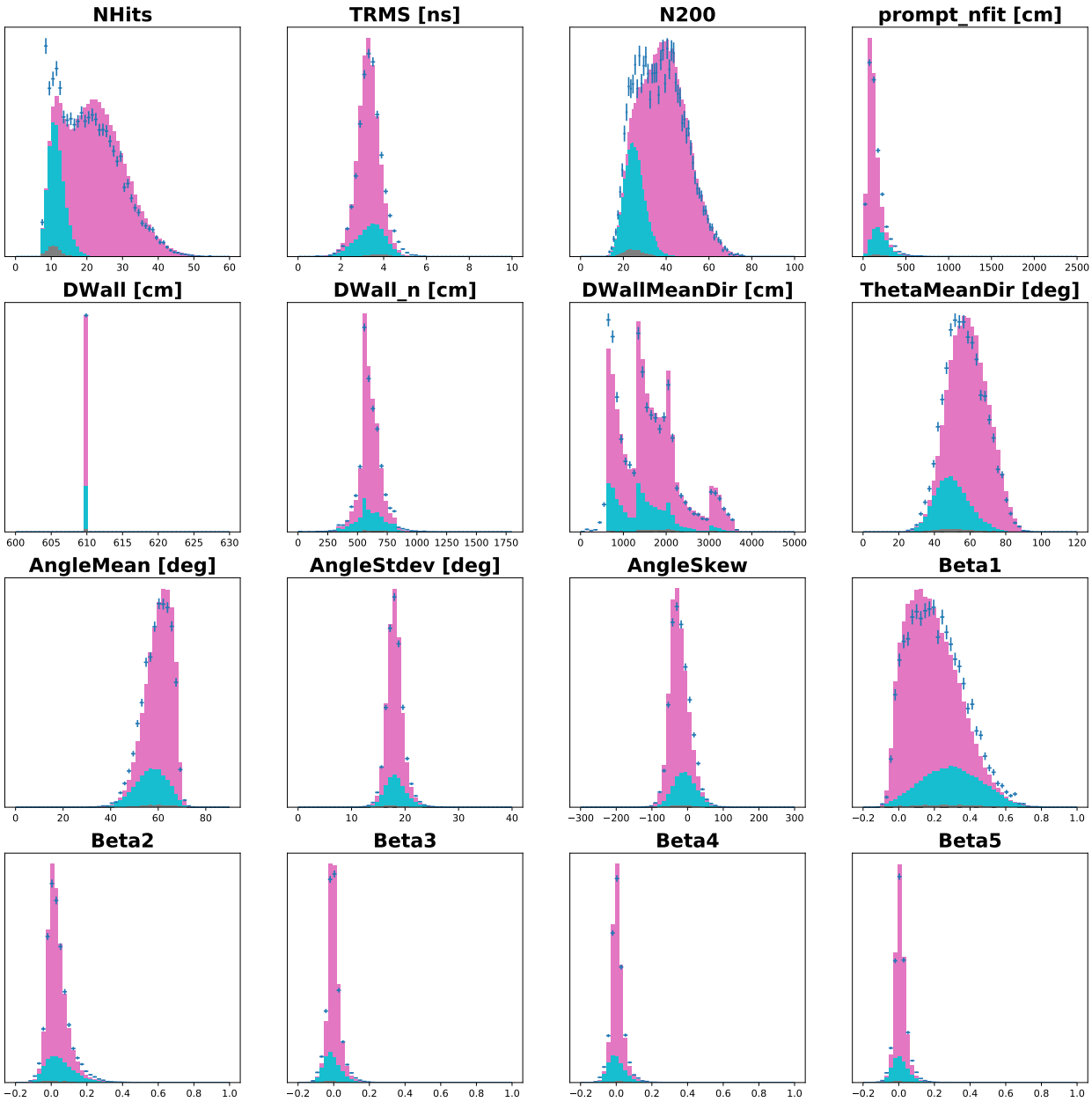

Figure C.4: Feature distributions of source dummy MC and data taken at $z = -12$ m (Run 85384), for tagged candidates. (blue: data, pink: MC (Gd), cyan: MC (H), gray: MC (noise))

Appendix D

Hypothesis test on *NHits*

It is difficult to evaluate the factors mentioned in Subsection 4.4.1 at the current stage, however, we can test a hypothesis to check which factor is the most significant. The hypothesis is that the detector characteristics of the simulator and the neutron capture models (i.e., the gamma-ray production models) are fully compatible with data. The cross sections are allowed to differ between data and MC, so that the capture ratio on Gd can be a free parameter. Under this assumption, we can model the tagged data distribution of feature x with individual disintegrated histograms we obtain from either MC or data.

First, let $h^{1n}_{\mathrm{MC}}(x)$ denote the bin value of the x histogram for single neutron source dummy MC. Then, $h^{1n}_{\mathrm{MC}}(x)$ can be expanded with a set of individual histograms as in Equation D.1:

$$h^{1n}_{\mathrm{MC}}(x) \simeq c_{\mathrm{MC}}\Big\{r_{\mathrm{MC}}h^{\mathrm{Gd}}_{\mathrm{MC}}(x) + (1 - r_{\mathrm{MC}})h^{\mathrm{H}}_{\mathrm{MC}}(x)\Big\} + h^{B}_{\mathrm{dark}}(x) + h^{B,\mathrm{all}}_{\mathrm{source}}(x) \tag{D.1}$$

Here, $h^{\mathrm{i}}_{\mathrm{MC}}$ ($i \in \{\mathrm{Gd}, \mathrm{H}\}$) represents the tagged x histogram of a single neutron MC where the simulated neutron is completely captured by the i^{th} nuclide. $h^{\mathrm{i}}_{\mathrm{MC}}$ should be a convolution of the detector's response (e.g., simulation physics models, water parameters, PMT gain, etc.) and the algorithm's detection efficiency (e.g., neural network, likelihood threshold, cut conditions, etc.). h^{B}_{dark} denotes the tagged x histogram of completely dark detector (i.e., sourceless dummy configuration), whereas $h^{B,\mathrm{all}}_{\mathrm{source}}$ denotes the same histogram with the source dummy configuration

subtracted by $h^B_{\rm dark}$. $r_{\rm MC}$ is the MC's captured neutron ratio to all generated neutrons, and $r_{\rm MC}$ is the MC's neutron capture ratio on Gd. The values of $c_{\rm MC}$ and $r_{\rm MC}$ are 0.984 and 0.507 for ∼0.0110 wt.% Gd concentration.

In a similar way, we can also model the x distribution $h^{\rm corr}_{\rm data}$ of a gamma-correlated data event where we expect a single neutron emitted from the source to be detectable, as in Equation D.2. Values and distributions that might differ from MC are subscripted "data." $h^B_{\rm dark}$ should be the same between data and MC, since we take those from dummy trigger data rather from simulation. Another thing to note is that the gamma-correlated data events should have some part of its radiation as noise, while the rest (i.e., gamma-correlated neutrons) should be included within $h^i_{\rm data}$ ($i \in \{{\rm Gd}, {\rm H}\}$). Hence, we denote the former as $h^{B,{\rm corr}}_{\rm source} := b h^{B,{\rm all}}_{\rm source}$, where the factor b should be close to the AmBe R-value (ratio of correlated neutrons to all neutrons) of ∼0.58 or higher in case a fraction of prompt gamma-rays are tagged by the algorithm.

$$h^{\rm corr}_{\rm data} \simeq c_{\rm data}\Big\{ r_{\rm data} h^{\rm Gd}_{\rm data}(x) + (1 - r_{\rm data}) h^{\rm H}_{\rm data}(x) \Big\} + h^B_{\rm dark}(x) + h^{B,{\rm corr}}_{\rm source}(x) \tag{D.2}$$

Now, let us introduce the parameter s that denotes the ratio of correlated neutron events to all event-cut passing events. Then, we can model the x distribution of all cut passing data events with Equation D.3.

$$\begin{aligned} h_{\rm data}(x) &\simeq s h^{\rm corr}_{\rm data} + (1 - s)\left\{ h^B_{\rm dark}(x) + h^{B,{\rm all}}_{\rm source}(x) \right\} \\ &= s\Big\{ c_{\rm data} r_{\rm data} h^{\rm Gd}_{\rm data}(x) + c_{\rm data}(1 - r_{\rm data}) h^{\rm H}_{\rm data}(x) + h^{B,{\rm corr}}_{\rm source}(x) \Big\} + (1 - s) h^{B,{\rm all}}_{\rm source}(x) + h^B_{\rm dark}(x) \\ &= s\Big\{ c_{\rm data} r_{\rm data} h^{\rm Gd}_{\rm data}(x) + c_{\rm data}(1 - r_{\rm data}) h^{\rm H}_{\rm data}(x) + b h^{B,{\rm all}}_{\rm source}(x) \Big\} + (1 - s) h^{B,{\rm all}}_{\rm source}(x) + h^B_{\rm dark}(x) \\ &= s c_{\rm data} r_{\rm data} h^{\rm Gd}_{\rm data}(x) + s c_{\rm data}(1 - r_{\rm data}) h^{\rm H}_{\rm data}(x) + \{1 - (1 - b)s\} h^{B,{\rm all}}_{\rm source}(x) + h^B_{\rm dark}(x) \end{aligned} \tag{D.3}$$

Assuming $h^i_{\rm MC} \simeq h^i_{\rm data}$ for $i \in \{{\rm Gd}, {\rm H}\}$, i.e., assuming that the simulated detector response and the algorithm efficiency are the same in both data and MC, we can model $h_{\rm data}$ with MC signal distributions $h^i_{\rm MC}$, the dark distribution $h_{\rm dark}$ from sourceless dummy, and the source-induced

noise distribution $h^{B,\mathrm{all}}_{\mathrm{source}}$ from source dummy, along with four fittable parameters s, $c(=c_{\mathrm{data}})$, $r(=r_{\mathrm{data}})$, and b, each within the range [0,1]. This is expressed in Equation D.4.

$$h^{\mathrm{fit}}_{\mathrm{MC}}(x) := scrh^{\mathrm{Gd}}_{\mathrm{MC}}(x) + sc(1-r)h^{\mathrm{H}}_{\mathrm{MC}}(x) + \{1-(1-b)s\}h^{B,\mathrm{all}}_{\mathrm{source}}(x) + h^{B}_{\mathrm{dark}}(x) \tag{D.4}$$

Below is the summary of the four free parameters:

- s: fraction of events with one signal neutron ($s_{\mathrm{MC}} = 1$)
- c: fraction of captured neutrons to all emitted neutrons ($c_{\mathrm{MC}} = 0.984$)
- r: fraction of neutron captures on Gd ($r_{\mathrm{MC}} = 0.507$)
- b: scaling parameter between gamma-uncorrelated source-induced background and all source-induced background

With the above hypothesis assuming Gaussian, we have estimated the best-fit parameter values of s, c, r, and b using a simple χ^2-test on the *NHits* distribution for Run 85386 ($z = 0$). h^{B}_{dark} was taken from Run 85392, the closest sourceless dummy run to Run 85386. $h^{B,\mathrm{all}}_{\mathrm{source}}$ was taken as the *NHits* distribution the only source dummy run available (Run 85388, $z = 0$) subtracted by h^{B}_{dark}. h^{i}_{MC} are taken from the source dummy MC used in Section 4.3. For all datasets, the signal likelihood threshold was set to 0.546, which gives 56.61 % capture detection efficiency with 1.99 % noise ratio for within sourceless dummy MC whose noise hits are taken from Run 85392. The corresponding capture detection efficiency is 94.62 % for $\mathrm{Gd}(n,\gamma)$ and 17.52 % for $p(n,\gamma)$ reaction. Each $h(NHits)$ is shown in the left figure of Figure D.1.

$\chi^2 = \sum_x (h_{\mathrm{data}}(x) - h^{\mathrm{fit}}_{\mathrm{MC}}(x))^2 / h^{\mathrm{fit}}_{\mathrm{MC}}(x)$ was calculated for bins with more than 5 candidates in the data *NHits* distribution. The χ^2-minimizing values of parameters s, c, r, and b were 1.000, 1.000, 0.423, and 0.585, respectively, and the fitted $h^{\mathrm{fit}}_{\mathrm{MC}}$ along with h_{data} is shown in the right of Figure D.1. Since the assumption $h^{i}_{\mathrm{MC}} \simeq h^{i}_{\mathrm{data}}$ for $i \in \{\mathrm{Gd}, \mathrm{H}\}$ is only approximate as the water parameters have not been tuned for Gd-loaded water, there is no reason to expect a perfect fit. Nonetheless, the fitted MC histogram shows reasonable agreement with data. The

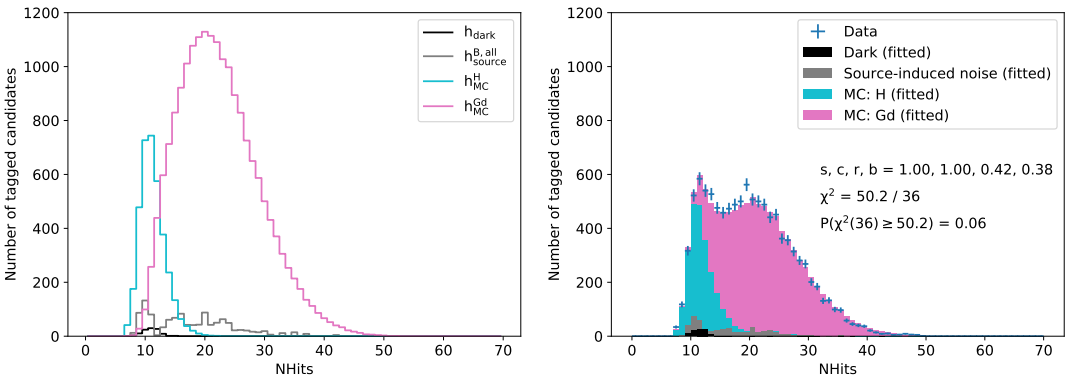

Figure D.1: The disintegrated histograms used for parameter estimation (left) and the fitted *NHits* distributions with the base histograms (right).

r_{MC} value of 0.507 and the fitted parameter values of $s = 1.00$ and $r(= r_{\mathrm{data}}) = 0.43$ indicate that neutronless triggers may be a negligible source of uncertainty, compared to the neutron capture ratio on Gd. The fitted b is 0.585, which is close to the AmBe R-value of ∼0.575.

With the Gaussian assumption, the parameter likelihood is assumed to be proportional to $e^{-\chi^2/2}$, and the normalized single parameter likelihood distributions are as illustrated in Figure D.2. The likelihood peaks of s and b are very localized so that their peak widths are within 2 % of the peak values, backing up that the neutron capture ratio on Gd should be a more serious source of uncertainty than neutronless triggers under the current fit model.

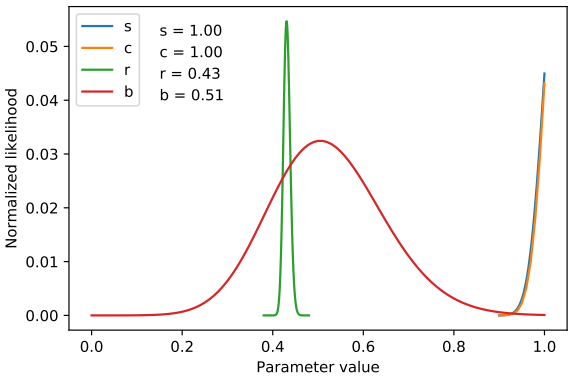

Figure D.2: Parameter fit.

The ratio $r_{\mathrm{MC}}/r^{\mathrm{fit}}_{\mathrm{data}}$ is ∼0.84. The Gd-neutron capture ratio r itself should be

$$r \approx \int_{E_{\mathrm{min}}}^{E_{\mathrm{max}}} \rho(E_n) \frac{n_{\mathrm{Gd}} \int_0^{E_n} \sigma_{\mathrm{Gd}}(E)/(dE/dx)\, dE}{\sum_X n_X \int_0^{E_n} \sigma_X(E)/(dE/dx)\, dE} dE_n \tag{D.5}$$

where $E_{\max}$ and $E_{\min}$ are the maximum and minimum kinetic energy of AmBe neutrons, $\rho(E_n)$ is the fraction of AmBe neutrons with kinetic energy E_n, n_X is the number density of element X, $\sigma_X(E)$ is the capture cross section of element X for neutron kinetic energy E, and dE/dx is the stopping power of neutrons in Gd-loaded water. For simplicity in MC, X is either Gd or H. Since the number densities are estimated within 1 % precision, $\rho(E)$, $\sigma_X(E)$, and dE/dx might be causing errors. To verify the source of uncertainty, a cross-check simulation with a precise neutron energy spectrum and different physics models should be carried out.

For reference, tuning the Gd concentration in MC to fit the capture time constant τ to $\tau_{data} \approx$ 116 µs has yielded $\epsilon_n^{\text{est.}} \sim$55 % for sourceless dummy MC and $\epsilon_n^{\text{est.}} \sim$52 % for source dummy MC. The Gd concentration was set to ∼0.0103 wt.%, and the corresponding r_{MC} was 0.4953. The discrepancy remains to persist even with lowered Gd concentration.

Bibliography

[1] T. J. Irvine. "Development of Neutron-Tagging Techniques and Application to Atmospheric Neutrino Oscillation Analysis in Super-Kamiokande". PhD thesis. The University of Tokyo, 2014.

[2] K. M. Tsui. *Super-K Gd project: Neutron-tagging algorithm.* 2017 Autumn Meeting, The Physical Society of Japan. Sept. 12, 2017. URL: http://www-sk.icrr.u-tokyo.ac.jp/~nakahata_s/tokusui/talk/ntag_jps_autumn_2017_kaming.pdf (visited on 12/14/2020).

[3] T. Mochizuki. "Development of 50-cm Diameter Photomultiplier Tubes and a Neutron Tagging Algorithm for Hyper-Kamiokande". MA thesis. The University of Tokyo, 2019. (Japanese).

[4] R. Akutsu. "A Study of Neutrons Associated with Neutrino and Antineutrino Interactions on the Water Target at the T2K Far Detector". PhD thesis. The University of Tokyo, 2019.

[5] K. Hirata et al. "Observation of a neutrino burst from the supernova SN1987A". In: *Phys. Rev. Lett.* 58 (14 Apr. 1987), pp. 1490–1493. DOI: 10.1103/PhysRevLett.58.1490. URL: https://link.aps.org/doi/10.1103/PhysRevLett.58.1490.

[6] Y. Fukuda et al. "Evidence for Oscillation of Atmospheric Neutrinos". In: *Phys. Rev. Lett.* 81 (8 Aug. 1998), pp. 1562–1567. DOI: 10.1103/PhysRevLett.81.1562. URL: https://link.aps.org/doi/10.1103/PhysRevLett.81.1562.

[7] A. D. Sakharov. "SPECIAL ISSUE: Violation of CP in variance, C asymmetry, and baryon asymmetry of the universe". In: *Soviet Physics Uspekhi* 34.5 (May 1991), pp. 392–393. DOI: 10.1070/PU1991v034n05ABEH002497.

[8] C. L. Cowan et al. "Detection of the Free Neutrino: a Confirmation". In: *Science* 124.3212 (1956), pp. 103–104. ISSN: 0036-8075. DOI: 10.1126/science.124.3212.103. URL: https://science.sciencemag.org/content/124/3212/103.

[9] S. Ando and K. Sato. "Relic neutrino background from cosmological supernovae". In: *New J. Phys.* 6 (2004), p. 170. DOI: 10.1088/1367-2630/6/1/170. arXiv: astro-ph/0410061.

[10] K. S. Krane. *Introductory nuclear physics*. New York, NY: Wiley, 1988.

[11] "Neutron Nuclear Reactions". In: *Nuclear Reactor Physics*. John Wiley & Sons, Ltd, 2007. Chap. 1, pp. 1–32. ISBN: 9783527611041. DOI: https://doi.org/10.1002/9783527611041.ch1. eprint: https://onlinelibrary.wiley.com/doi/pdf/10.1002/9783527611041.ch1.

[12] K. Shibata et al. "JENDL-4.0: A New Library for Nuclear Science and Engineering". In: *Journal of Nuclear Science and Technology* 48.1 (2011), pp. 1–30. DOI: 10.1080/18811248.2011.9711675. URL: https://doi.org/10.1080/18811248.2011.9711675.

[13] L. Marti Magro et al. "Evaluation of gadolinium's action on water Cherenkov detector systems with EGADS". In: *Nuclear Instruments and Methods in Physics Research Section A: Accelerators, Spectrometers, Detectors and Associated Equipment* 959 (Feb. 2020), p. 163549. DOI: 10.1016/j.nima.2020.163549.

[14] K. Hagiwara et al. "Gamma-ray spectrum from thermal neutron capture on gadolinium-157". In: *Progress of Theoretical and Experimental Physics* 2019.2 (2019). ISSN: 2050-3911. DOI: 10.1093/ptep/ptz002. URL: https://doi.org/10.1093/ptep/ptz002.

[15] P. A. Cherenkov. "Visible emission of clean liquids by action of γ radiation". In: *Dokl. Akad. Nauk. SSSR 2, 451* (1934).

[16] T. Lou. "Development of 50 cm Diameter Hybrid Photo-Detector for Hyper-Kamiokande". MA thesis. The University of Tokyo, 2017.

[17] J. D. Jackson. *Classical electrodynamics*. Third edition. New York : Wiley, [1999] ©1999. URL: https://search.library.wisc.edu/catalog/999849741702121.

[18] K. Abe et al. "Constraint on the matter–antimatter symmetry-violating phase in neutrino oscillations". In: *Nature* 580.7803 (2020), pp. 339–344. ISSN: 1476-4687. DOI: 10.1038/s41586-020-2177-0. URL: https://doi.org/10.1038/s41586-020-2177-0.

[19] Super-Kamiokande Collaboration. *Introduction of Gadolinium into Super-Kamiokande and the Start of New Observations*. Aug. 21, 2020. URL: http://www-sk.icrr.u-tokyo.ac.jp/sk/news/2020/08/sk-gd-detail-e.html.

[20] M. B. Chadwick et al. "ENDF/B-VII.1 Nuclear Data for Science and Technology: Cross Sections, Covariances, Fission Product Yields and Decay Data". In: *Nuclear Data Sheets* 112.12 (2011), pp. 2887–2996. ISSN: 0090-3752. DOI: https://doi.org/10.1016/j.nds.2011.11.002. URL: http://www.sciencedirect.com/science/article/pii/S009037521100113X.

[21] C. Simpson et al. "Sensitivity of Super-Kamiokande with Gadolinium to Low Energy Antineutrinos from Pre-supernova Emission". In: *The Astrophysical Journal* 885.2 (Nov. 2019), p. 133. DOI: 10.3847/1538-4357/ab4883. URL: https://doi.org/10.3847%7B%5C%%7D2F1538-4357%7B%5C%%7D2Fab4883.

[22] K. M. Tsui et al. *skdetsim-skgd*. https://github.com/kmtsui/skdetsim-skgd. 2020. commit a8caebc.

[23] C. Zeitnitz and T. A. Gabriel. "The GEANT-CALOR interface and benchmark calculations of ZEUS test calorimeters". In: *Nuclear Instruments and Methods in Physics Research Section A: Accelerators, Spectrometers, Detectors and Associated Equipment* 349.1 (1994), pp. 106–111. ISSN: 0168-9002. DOI: https://doi.org/10.1016/0168-9002(94)90613-0. URL: http://www.sciencedirect.com/science/article/pii/0168900294906130.

[24] M. Sakuda et al. *Website of the ANNRI-Gd model*. http://www.physics.okayama-u.ac.jp/~sakuda/ANNRI-Gd_ver1.html. (Visited on 12/14/2020).

[25] T. Tanaka et al. "Gamma-ray spectra from thermal neutron capture on gadolinium-155 and natural gadolinium". In: *Progress of Theoretical and Experimental Physics* 2020.4 (Nov. 2020). ISSN: 2050-3911. DOI: 10.1093/ptep/ptaa015. URL: https://doi.org/10.1093/ptep/ptaa015.

[26] E. Mendoza and D. Cano-Ott. "Update of the Evaluated Neutron Cross Section Libraries for the Geant4 Code". In: ().

[27] G. Horton-Smith. *GLG4sim, Generic liquid-scintillator anti-neutrino detector Geant4 simulation*. URL: http://neutrino.phys.ksu.edu/~GLG4sim/ (visited on 01/06/2021).

[28] S. Tobayama. "An analysis of the oscillation of atmospheric neutrinos". PhD thesis. University of British Columbia, 2016.

[29] F. Chollet et al. *Keras*. https://keras.io. 2015.

[30] I. Goodfellow, Y. Bengio, and A. Courville. *Deep Learning*. MIT Press, 2016.

[31] M. Smy. "Low Energy Event Reconstruction and Selection in Super-Kamiokande-III". In: *30th International Cosmic Ray Conference*. Vol. 5. July 2007, pp. 1279–1282.

[32] A. Bellerive et al. "The Sudbury Neutrino Observatory". In: *Nuclear Physics B* 908 (July 2016), pp. 30–51. ISSN: 0550-3213. DOI: 10.1016/j.nuclphysb.2016.04.035. URL: http://dx.doi.org/10.1016/j.nuclphysb.2016.04.035.

[33] A. Hoecker et al. "TMVA: Toolkit for Multivariate Data Analysis". In: *PoS* ACAT (2007), p. 040. arXiv: physics/0703039.

[34] A. Hoecker et al. *User's Guide*. Oct. 4, 2013. URL: http://tmva.sourceforge.net/old_site/docu/TMVAUsersGuide.pdf (visited on 12/22/2020).

[35] D. P. Kingma and J. Ba. *Adam: A Method for Stochastic Optimization*. 2017. arXiv: 1412.6980 [cs.LG].

[36] T. Yano, Y. Isobe, and A. Suzuki. *Installation of Automated Source Deployment System*. Nov. 8, 2018.

[37] Z. Liu et al. "The 4.438MeV gamma to neutron ratio for the Am–Be neutron source". In: *Applied Radiation and Isotopes* 65.12 (2007), pp. 1318–1321. ISSN: 0969-8043. DOI: https://doi.org/10.1016/j.apradiso.2007.04.007. URL: http://www.sciencedirect.com/science/article/pii/S0969804307001200.

[38] H. Watanabe et al. "First study of neutron tagging with a water Cherenkov detector". In: *Astroparticle Physics* 31.4 (2009), pp. 320–328. ISSN: 0927-6505. DOI: https://doi.org/10.1016/j.astropartphys.2009.03.002. URL: http://www.sciencedirect.com/science/article/pii/S0927650509000401.

[39] Eckert & Ziegler Nuclitec GmbH. *Sealed Radiation Sources Product Information*. URL: http://www.hanshin-eng.co.kr/index/img/5Nuclitec.pdf (visited on 12/26/2020).

[40] J. Scherzinger et al. "A comparison of untagged gamma-ray and tagged-neutron yields from 241AmBe and 238PuBe sources". In: *Applied Radiation and Isotopes* 127 (2017), pp. 98–102. ISSN: 0969-8043. DOI: https://doi.org/10.1016/j.apradiso.2017.05.014. URL: http://www.sciencedirect.com/science/article/pii/S0969804316309861.

[41] *Neutron sources:Americium-241/Beryllium and Californium-252*. 1976. URL: https://permalink.lanl.gov/object/tr?what=info:lanl-repo/lareport/LA-UR-11-01808. The source is re-referenced from the URL.

[42] K. W. Geiger and L. Van Der Zwan. "Radioactive neutron source spectra from 9Be(α, n) cross section data". In: *Nuclear Instruments and Methods* 131.2 (1975), pp. 315–321. ISSN: 0029-554X. DOI: https://doi.org/10.1016/0029-554X(75)90336-5. URL: http://www.sciencedirect.com/science/article/pii/0029554X75903365.

[43] *BGO Bismuth Germanate*. URL: https://www.crystals.saint-gobain.com/products/bgo (visited on 12/27/2020).

[44] W. Wolszczak et al. "Temperature Properties of Scintillators for PET Detectors: a Comparative Study". In: Nov. 2014. DOI: 10.1109/NSSMIC.2014.7430768.

[45] C. L. Melcher et al. "Temperature Dependence of Fluorescence Decay Time and Emission Spectrum of Bismuth Germanate". In: *IEEE Transactions on Nuclear Science* 32 (1985), pp. 529–532.

[46] H. Vincke et al. "Response of a BGO detector to photon and neutron sources: simulations and measurements". In: *Nuclear Instruments and Methods in Physics Research Section A Accelerators Spectrometers Detectors and Associated Equipment* 484 (May 2002). DOI: 10.1016/S0168-9002(01)01966-0.

[47] E. Gschwendtner. "Benchmarking the Particle Background in the LHC Experiments". Presented on 17 Sep 2000. 2000. URL: https://cds.cern.ch/record/532546.

[48] Y. Nakajima. *Status of water system and water in the tank*. Dec. 2, 2020. (internal).

[49] S. Han. *Estimating the ratio of neutron-less scintillation with SKG4*. URL: http://indico-sk.icrr.u-tokyo.ac.jp/event/5538/contributions/15861/attachments/15854/18637/han_neutronless_scint.pdf (visited on 01/06/2020). (SK internal).

[50] F. Capozzi et al. "Global constraints on absolute neutrino masses and their ordering". In: *Phys. Rev. D* 95 (9 May 2017), p. 096014. DOI: 10.1103/PhysRevD.95.096014. URL: https://link.aps.org/doi/10.1103/PhysRevD.95.096014.

[51] J. L. Hewett et al. *Fundamental Physics at the Intensity Frontier*. 2012. arXiv: 1205.2671 [hep-ex].

[52] G. N. Vlaskin, Y. S. Khomyakov, and V. I. Bulanenko. "Neutron Yield of the Reaction (α, n) on Thick Targets Comprised of Light Elements". In: *Atomic Energy* 117.5 (2015), pp. 357–365. ISSN: 1573-8205. DOI: 10.1007/s10512-015-9933-5. URL: https://doi.org/10.1007/s10512-015-9933-5.